

3D Slicer: A Free, Open Source Tool for 3D Image Registration

J.P.Robinson¹, E.Claridge², P.R.Cooper³, L.M.Grover³, M.Sandzholzer³ and A.D.Walmsley³

¹ Physical Science of Imaging in the Biomedical Sciences (PSIBS), University of Birmingham, Edgbaston, Birmingham, B15 2TT, UK. j.p.robinson@cs.bham.ac.uk

² School of Computer Science, University of Birmingham

³ School of Dentistry, University of Birmingham

Aims

Image registration is the process of aligning one image set with another such that they are in the same coordinate system. An optimal mathematical geometric transformation between the image sets is estimated and applied, enabling them both to be compared and analysed [1].

Examples of applications include:

- Aligning images from the same specimen to study how it has changed over time (different time points)
- Aligning images from different specimens to study how they differ (different specimens)
- Constructing an atlas of normal specimens. Aligning a treated/diseased specimen to an atlas of normal specimens to investigate how it differs [1].

3D Slicer (available online at www.slicer.org) is a free, open source, easy-to-use image visualization and analysis software package. It is multi-threaded and available on multiple platforms, including Windows Linux and Mac OS X. Since 1998, it has been actively developed by a community of scientists and is capable of various image registration methods [2].

The purpose of this study was to evaluate and validate the accuracy of a rigid registration algorithm. The subject used for validation was the recording of changes in the root canals of teeth following root canal treatment. The presentation provides a demonstration on the use of this software and its ability to allow registration of images.

Method



Figure 1: Photo of lower first molar

A lower first molar tooth was scanned at four different time points, each time being removed and reinserted on the positioning stage. Teeth are anatomically approximately symmetric along their median sagittal axis (Figure 1), and the registration algorithm may therefore converge on the wrong result. To prevent this, teeth were placed in the scanner at similar rotational alignments.

Analysis of the anatomy of the molar tooth was undertaken using a Skyscan 1172. The entire lengths of teeth were scanned at 80 kV, 124µA, at an isotropic resolution of 7-13µm resulting in the acquisition of 1100-1200 cross-sections. A camera exposure time of 620ms, a rotation step of 0.4°, frame averaging of 9 and medium filtering of the data was applied. X-rays

were filtered with the equipment's aluminium and copper filter. A flat field correction was taken on the day, prior to scanning to correct for variations in the pixel sensitivity of the camera. Images were reconstructed using NRecon 1.6.2 with a bream hardening correction of 25% and a ring artifact correction of 20.

To reduce noise, the reconstructed images were processed with an edge preserving smoothing algorithm as described by Gonzalez and Woods [3] and written as an Image J Plugin (University of Jyväskylä, Finland). A window of 3 and standard deviation variance of 15 were used.

ImageJ 1.45r was used to convert each image set into the NRRD file format, a format compatible with 3D Slicer 3.6.3. The first image set was used as a reference, and the subsequent images sets were registered to the reference. The images were registered using rigid transformations (rotation and translation), mattes mutual similarity metric and gradient descent optimisation (figure 2):

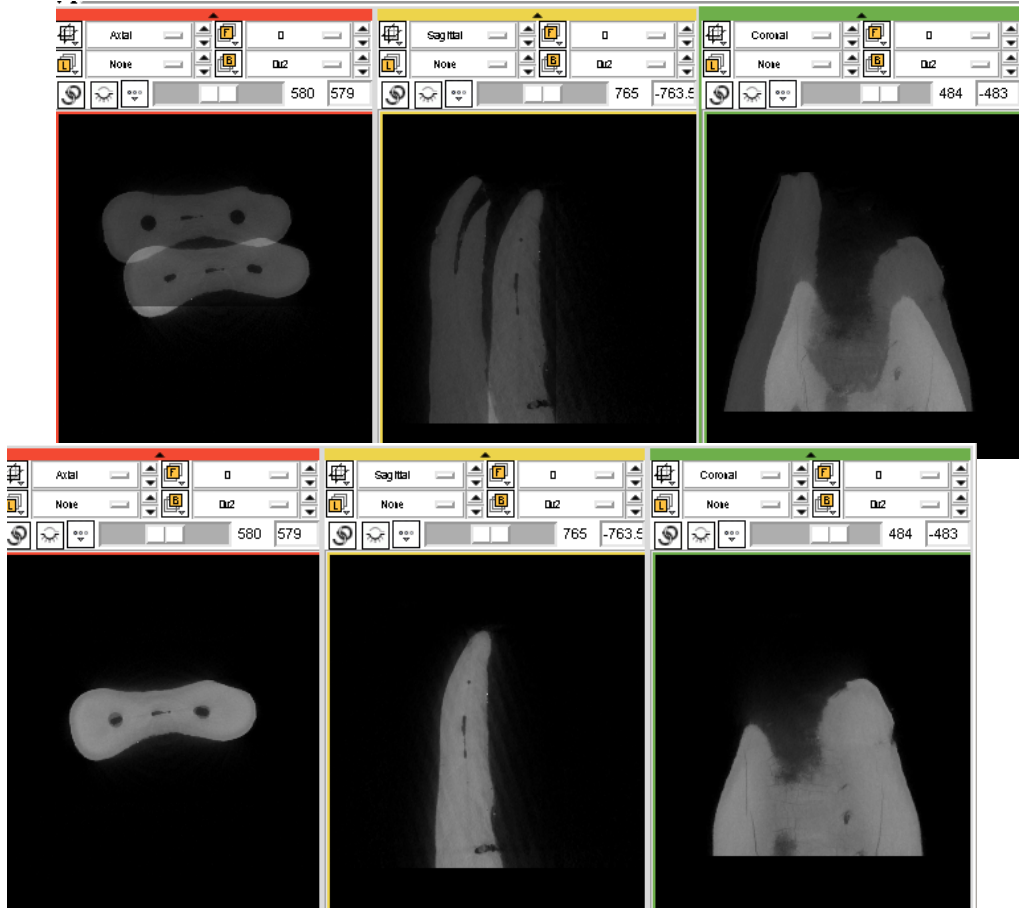


Figure 2: microCT images of two superimposed teeth prior to (top three panels) and after (bottom three panels) rigid image registration. The three views are axial (left), sagittal (middle) and coronal (right).

The root canals in the teeth were segmented using a 3D region growing approach and similarity was quantitatively compared using the Tanimoto similarity coefficient which is formulated as:

$$J(A, B) = \frac{|A \cap B|}{|A \cup B|}$$

where A and B are binary images [4]. This function gives a value between 0 and 1, 0 being different and 1 being identical.

Results

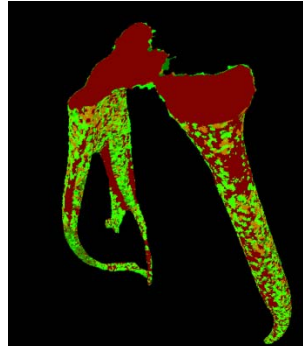


Figure 3: The 5 registered image sets superimposed. Red identifies areas where all image sets agree and green, areas of disagreement.

Tanimoto's similarity coefficient was between 0.93 - 0.94 for canal space signifying excellent co-registration accuracy. Figure 3 is a picture of all image sets superimposed after registration. It shows that the source of error is on the surface of the tooth, as a consequence of the segmentation process. Electronic noise, small deviations of the photons (scatter), and the polychromatic nature of the x-rays all contribute towards artifacts and noise. These are amplified by the reconstruction process, which contributes to segmentation inaccuracy. The image quality may be improved by performing greater levels of smoothing.

Conclusion

Images were registered with excellent accuracy. Figure 4 demonstrates how registration with 3D Slicer is now being used within dental research.

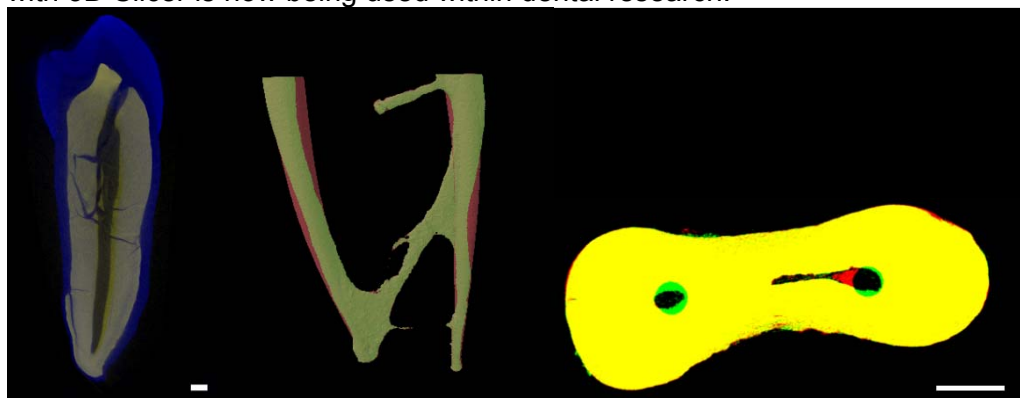


Figure 4: Examples of how registration is being used in dental research. Left image shows heat-induced dimensional changes of a premolar (Image pre-treatment is coloured blue, and image post-treatment is yellow). The image shows how the crown has been destroyed and cracks introduced. The middle image shows how a canal system inside a tooth has been enlarged by files used in root canal treatment. Image before treatment is coloured green and image after is coloured red. The right image is a cross-section through a tooth before and after root canal treatment. Yellow indicates areas of similarity, green shows area of canal enlargement by the dental file and red indicates build up of debris inside the canal. All scale bars represent 1mm.

References:

1. Barbara Z, Flusser J, "Image registration methods: a survey", *Image and Vision Computing*, 21, 997-1000, 2003
2. 3D Slicer, <http://www.slicer.org/pages/Introduction> (accessed 01/02/2012)
3. Gonzalez, R.C. and R.E. Woods, "*Digital image processing*" / Rafael C. Gonzalez, Richard E. Woods. 2nd ed2002, Upper Saddle River, N.J.: Prentice Hall. xx, 793.
4. Rogers, D.J. and T.T. Tanimoto, "A Computer Program for Classifying Plants. Science", 132, 117-1118, 1960.

A simple solution to help mounting centered samples to scan when using the Skyscan micro-CT attachment for SEM

J. Alba-Tercedor¹

¹ Department of Zoology. Faculty of Sciences. University of Granada. 18071-Granada. Spain.
jalba@ugr.es

Aims

Since our beginnings as an enthusiastic users of the micro-CT technology to prepare, to mount, and finally to reconstruct volume renderings of the anatomy of very tiny animals, we have found some difficulties. Some of them derivate of the inexperience (see Alba-Tercedor & Sáinz-Cantero, 2010). Probably one of the major challenges that, as new users of the micro-CT attachment for SEM, we encountered it was to center accurately the sample (specimen) to scan. This applies especially when using high magnification (with pixel sizes lower than 1 μm). In these cases a small variation in the central position, makes impossible to get a scan because when the sample rotates during the scanning procedure, the projection of the image come out of the vision field. When mounting a sample on the specimen holder (sample mount) by naked eye, or even under the stereo microscope, it can apparently looks well centered. However, later when mounted in the SEM, and before to start the scan, if the sample is rotated 90° and/or 180°, it is quite common to test that the image of the interest area to scan come out of focus. For that reason, normally several (or many) tries are needed before to get a satisfactory centered position of the sample. This represents an unnecessary waste of time and a cost. So here we present how up to know we are conducting to solve this annoying problem.

Method

Just after starting to use the micro-CT attachment for SEM, we ran into the above describe challenging problem of how to center properly the sample. Thus, first it all (and following the earlier advices of the Skyscan people), we were trying to center the sample by mounting it on the sample mount and by inserting it on the rotation stage axis. So by naked eye or under the microscope we were rotating the sample mount by hand and observing any apparent deviation of the center and correcting the position, if necessary. However to work directly with the rotation stage under the stereo microscope (that resulted more effective than naked eye), resulted if not impossible, at least an annoying task due to the scarce space existing between the sample mount (once it is fixed on the axe) and other parts of the rotation stage. Thereafter, we decided to build a separate little platform with an axis to fix the sample mount (indeed a “manual rotation stage” where to mount and test if the sample is centered – focused- or it is not, Fig. 1). This permits an easy manipulation because fingers have plenty of space around to be able to rotate the sample mount, permitting to observe if the position of the specimen is properly centered.

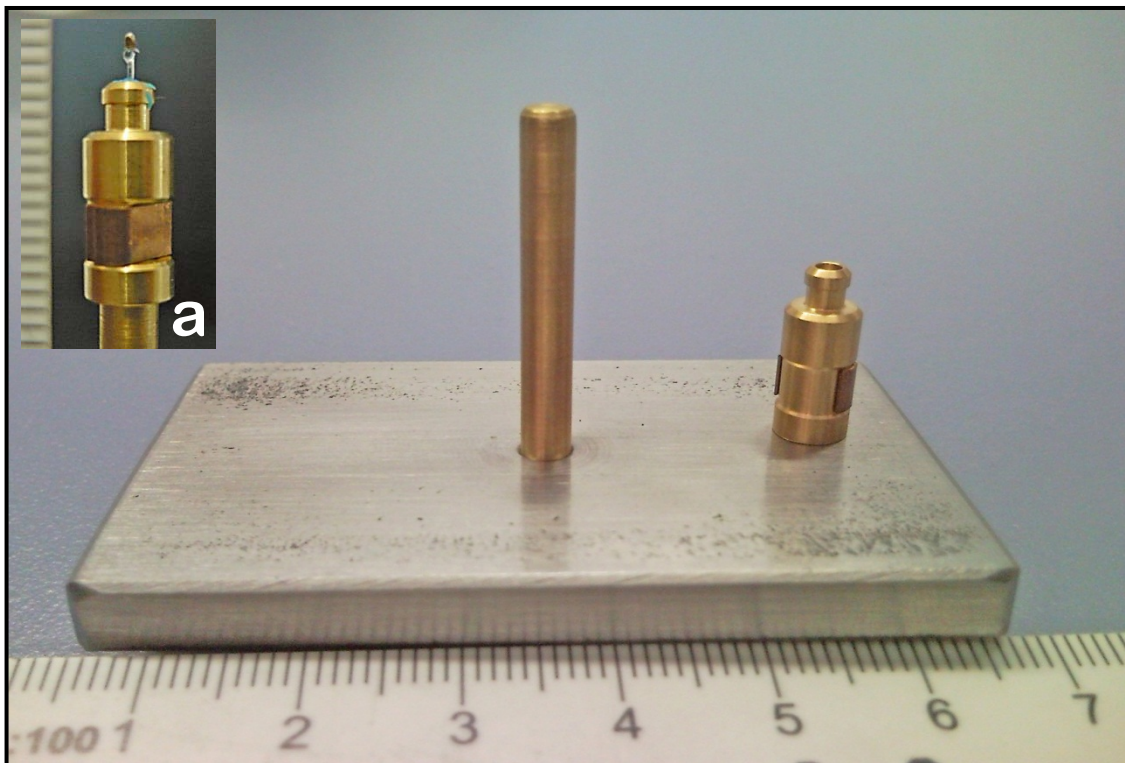


Figure 1: Manual rotation stage to help mounting centered samples and a close up of a specimen mounted on a stub, already mounted on the axis of the stage's test (**a**).

Results and Discussion

With the above simple described device it was possible to start to focus properly samples. However, it revealed not to be enough to be able to evaluate with accuracy if the specimen (sample) was situated in a central position. So we decided to implement the methods by using an auxiliary reference positional grid installed in the stereo microscope ocular by using an ocular micrometer (Fig. 2).

So after a preliminary adjust and focus of the sample putting it in a preliminary central position. Then the manual rotation stage (Figs.: 1 & 2a), was used to observe it apically (at higher magnifications) under the stereo microscope to be able to see correctly the specimen (Fig. 2b). Overexposing the image with the scale of the ocular micrometer, and fixing a reference in the scale. By rotating 180° (left and right) the stub (sample mount), is quite easy to discover and to correct any existing deviation of the central position by comparing with the reference in the scale line (Fig 2c).

Additionally we propose another little complement (not yet implemented!), but we advance the idea here. It would be a wire (or a thin long piece of metal) pointing straight forwards to the center of the sample mount. Thus, just rotating the sample on the rotation stage will give a more accurate idea of the focus of the specimen. The fixation of it could be an easy task, because the metal target already has a hole where screwing an appropriate screw (Fig.3).

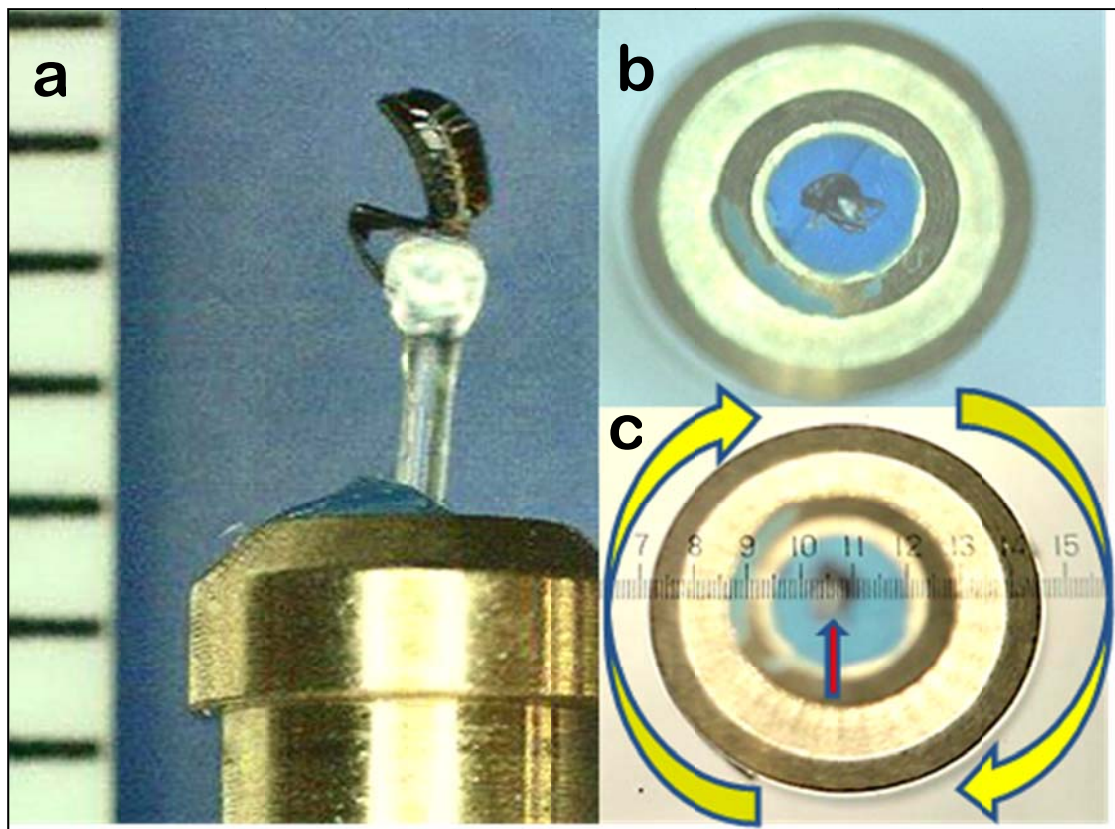


Figure 2: Example of how to proceed to center the abdomen of a little beetle insect mounted on a sample mount (**a**: preliminary mounting of the specimen in a central position by using the manual rotation stage; **b**: to observe it apically at a high magnification to be able to see correctly the specimen; **c**: to overexpose it to the scale of the ocular micrometer, fixing a reference. Finally, by rotating 180° -left and right- the sample mount, it is quite easy to discover any deviation of the central position with respect the reference).

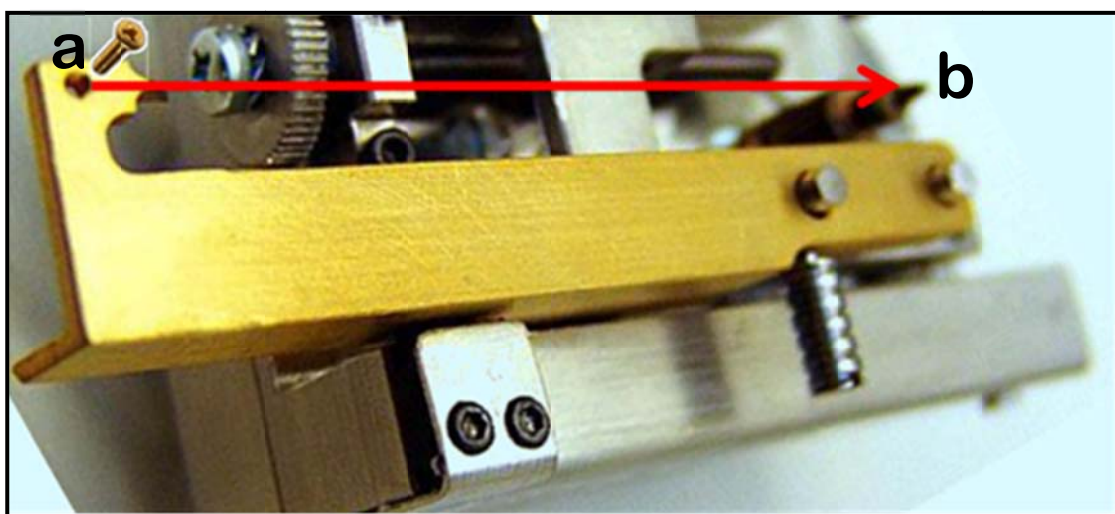


Figure 3: Proposal of a new complement, It would be a wire or a thin long piece of metal (see position in red), screwed on the existing hole (**a**), and pointing straight forwards to the center of the specimen holder (**b**).

Conclusions

As users, always there are occasions to find any challenging task not well solved or not fitting with our particular needs. However, we are constantly experiencing that normally anyone of our queries receive a quick reply and effective solution given by the Skyscan people. And they solve most of them in a daily and efficient manner. Moreover, as it can be read in a technical document produced by the company: “SkyScan users also have shown a lot of inventiveness and creativity in finding solutions themselves for mounting all manner of different samples” (Skyscan, 2008). Thanks to that there is a constant improvement of the efficiency when finding new procedures to get better results. So following this philosophy, the procedure here described, including the “Manual rotation stage”, facilitates a correct central position of the sample, making possible to scan specimens at high magnifications (pixel size lower than 1 µm). Moreover the thin pointer fixed on the metal target, could help to add more accuracy to this task.

For others Skyscan micro-tomography systems, there is a motorized “micropositioning stage” (<http://www.skyscan.be/products/stages.htm>) that facilitates enormously the task of centering the samples. However, in case of don't possess it, a similar manual stage, could be also very useful to centering the samples. A platform similar to that of Fig. 1 can be used. But with a hole to insert and rotate the sample holder, instead of have a fixed axis inserted. Thus, the same procedure (described for the use of a manual rotation stage) could be used to be able to mount the specimens in a correct central position.

Acknowledgements

We are indebted to our colleague Dr. José Luis Caballero López-Lendinez, the handy man who kindly built the “manual rotation stage” that we described here.

To the Skyscan people for giving us a fast support, especially to Alexander Sasov and Bart Pauwels, for their patience effectiveness and kindness answering our constant bombing of queries.

This work was supported by the Spanish “Ministerio de Educación y Ciencia” (CGL2007 – 61856/BOS), and the “Junta de Andalucía” (RNM-02654).

References:

1. Alba-Tercedor, J., Sáinz-Cantero, C. “Studying Aquatic Insects Anatomy with the Skyscan 1172 high-resolution micro-CT”. *Skyscan Users Meeting 2010* vol. 2: 8-11, 2010 (http://www.skyscan.be/company/UM2010/abstract_08.pdf)
2. Skyscan. “Method Notes, Skyscan 1172 Desktop Micro-CT”. pp: 1-53. (Skyscan, Ed.). Kontich, Belgium, 2008.

Surface and volume rendering of large datasets

Kevin Mackenzie

Institute of Medical Sciences, University of Aberdeen, Aberdeen, AB25 2ZD
k.s.mackenzie@abdn.ac.uk

Aims

As part of a project I was involved with looking at the development of teeth, I recently visited Skyscan NV, Kontich, Belgium to scan some medieval maxilla jaw fragments and a whole mandible (Fig. 1). The scans resulted in extremely large datasets and these proved very difficult to view on a standard Windows XP Desktop computer.

It quickly became apparent that I would need a higher spec computer to allow visualization and rendering of these samples. So I purchased a Dell 64-bit Windows 7 PC (XEON 3.20GHZ) with 12GB RAM plus an ATI FirePro V7800 (Fire GL) 2GB graphics card, and installed the 64-bit versions of CTAn (1.1.11), CTVol (2.1), and CTvox (2.3) on it.

The main objective was to analyze these scans and compare the resulting surface and volume rendered images using CTVol and CTvox respectively.

The resulting quality of images and the ease with which the new computer could handle these files, especially using CTvox, prompted me to revisit previous scans from our Skyscan 1072 desktop micro-CT scanner that in the past had been difficult to open.

I have also been able to demonstrate the ease with which stereo pair images (red/ blue) can be created within CTVol and CTvox, and to create small models that can be viewed on an Apple mobile device.

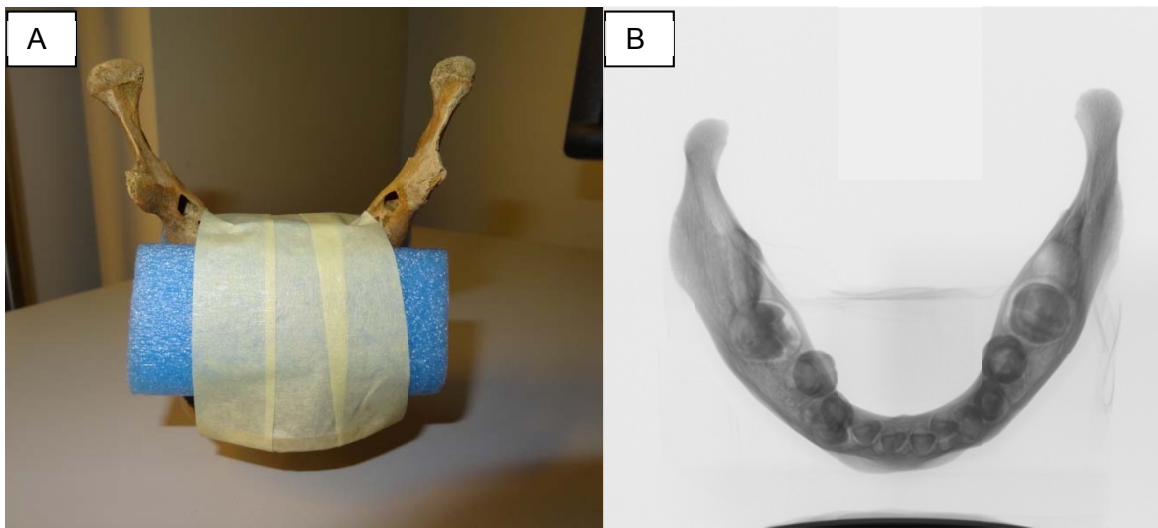


Figure 1: (A) Mandible taped up and ready to go into scanner, (B) Back projection image of combined scan of mandible using the Skyscan 1173.

Method

The maxilla and whole mandible samples were scanned using the Skyscan 1173 high energy, spiral scan micro CT scanner, at 115kV/69uA using a 0.25mm brass filter, pixel size 25um, rotational step of 0.15 degrees and rotated for 360 degree with frame averaging set at 2 and exposure time of 1.5sec.

The smaller maxilla samples took 1 hour 14 minutes to scan and resulted in 1440 images and file size of 13.4GB. Reconstruction was then carried out using NRecon (1.6.4) using settings of ring artifact correction 6 and beam hardening of 15%. This resulted in 1769 slices and a file size of 8.26GB (2k x 2k BMP file format).

The larger mandible required an oversized connected scan that took 6 hours 20mins to complete and resulted in 4800 back projection images with a file size of 84.8GB. Reconstruction was again carried out using NRecon (ver 1.6.4) with the same settings as above. This resulted in 3188 slices and a file size of 6.03GB (this time as 4k x 3k PNG file, (as BMP files would have resulted in 50.7GB)).

These reconstructed datasets were then loaded into CTAn and 3D surfaced rendered models created and then viewed in CTVol. (Fig. 2). This was time consuming and could take a few hours or more to create a model depending on its complexity.

These datasets were also opened in CTvox to create volume rendered models. Opacity was adjusted, colour texture file applied and shadow and/or material affect applied (Fig. 3). Red/blue stereo images were also created in both software packages using stereo mode from the Options menu or by selecting the red green glasses icon on toolbar. The time taken to load the dataset was considerably faster than CTVol taking only 5 to 10mins.

Results

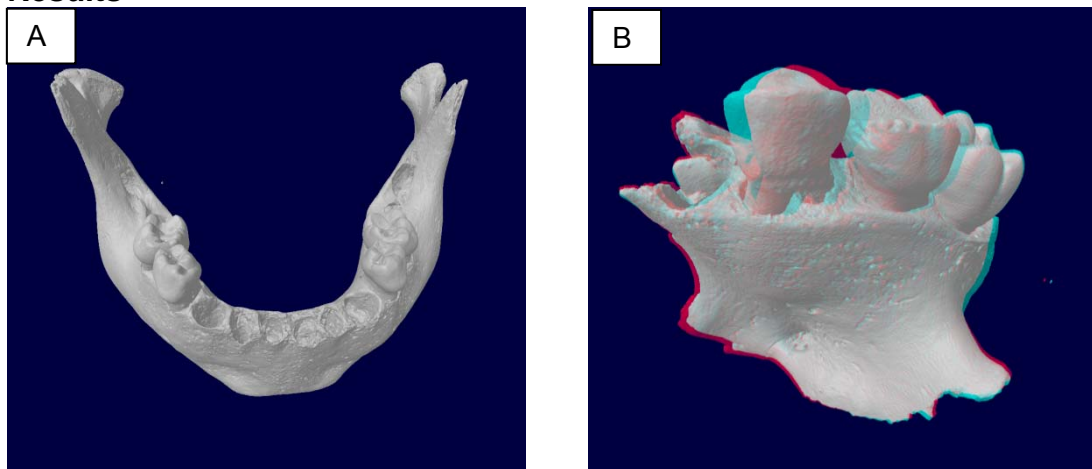


Figure 2: CTVol images (A) Mandible rendered image in p3g format, (B) Stereo mode 3D image of maxilla fragment (red/blue stereo pair).

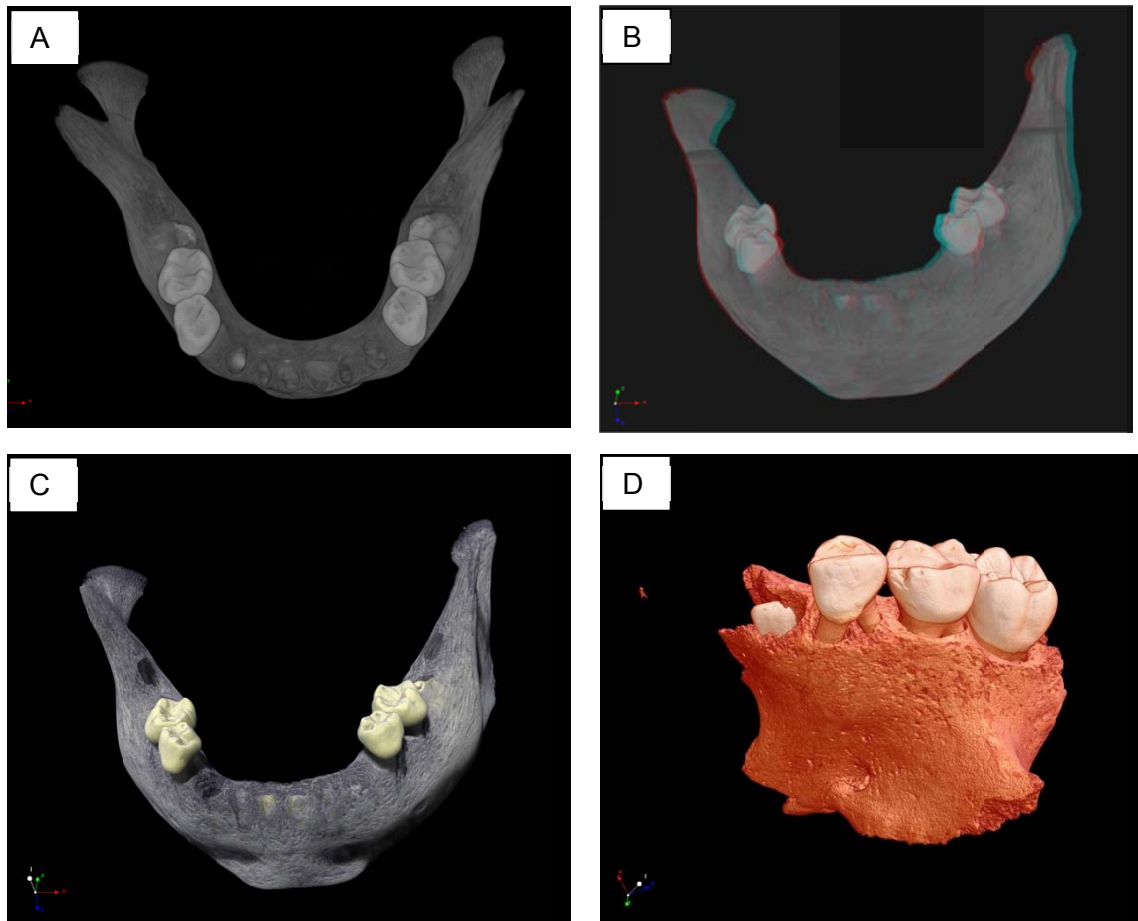


Figure 3: CTvox images (A) Mandible volume rendered image. (B) Stereo mode 3D image (red/blue stereo pair). (C) Use of colour textures and adjustment of opacity. (D) Maxilla - combined colour textures with shadow and surface lighting options.

As stated above, some scans from our Skyscan 1072 desktop micro-CT scanner had in the past had been difficult to open. Bone samples settings of 50kV/187uA and 0.5mm Al filter, 0.68 degrees step for 180 degrees, produced a back projection dataset of 276 images with a file size of 553 MB; and, after using NRecon to carry out reconstruction (Ring artifact correction 7 and Beam Hardening 20%), 975 images with a file size of 976 MB.

Sometimes, to allow the creation of 3D models, we had to reduce the reconstructed dataset size by resizing and selecting defined ROI in CTan.

The new computer allows us to easily open the datasets at full size and so we are now able to utilize the many functions in CTvox. This has led to re-examination of scans we have done over the years (Fig. 4).

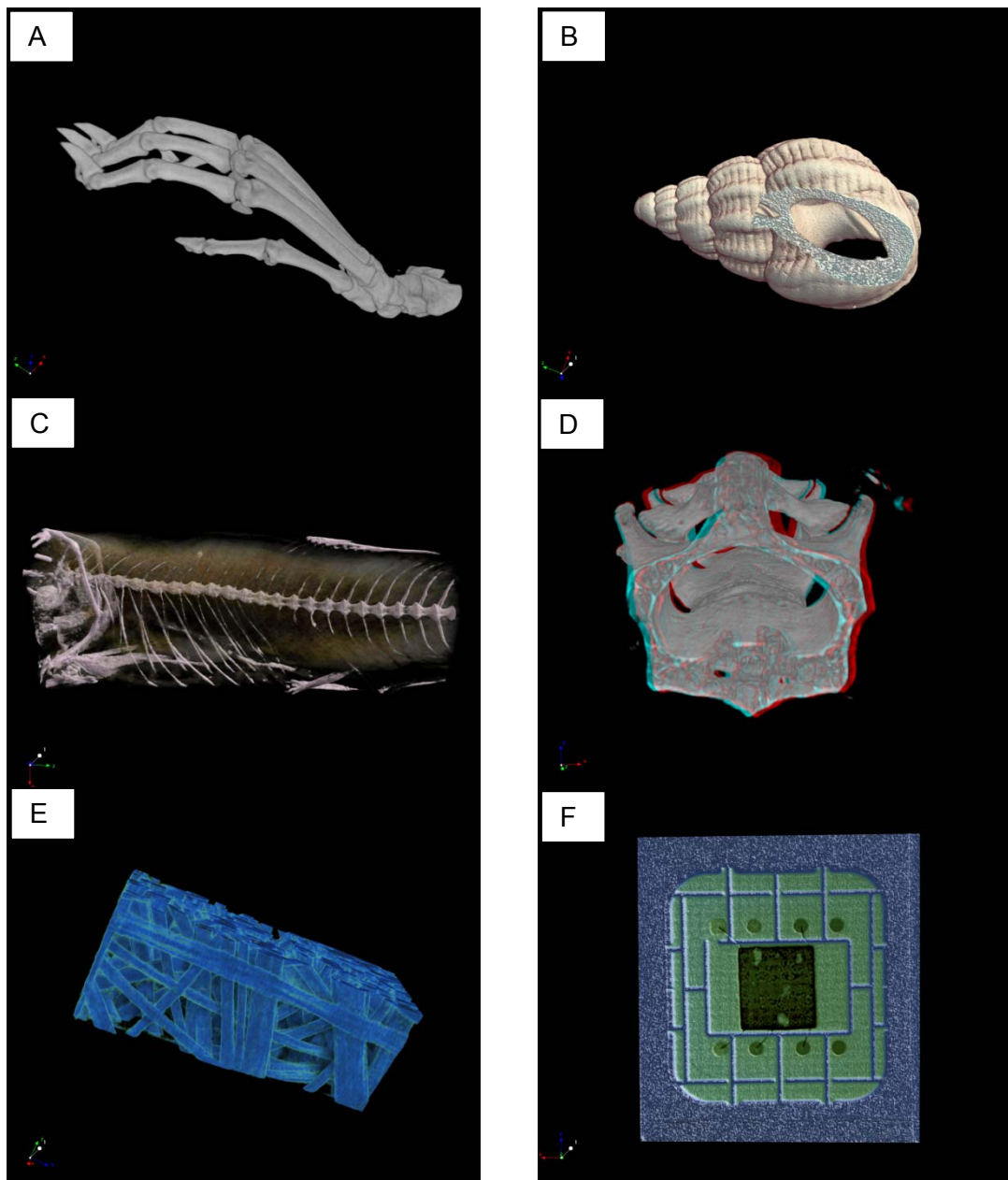


Figure 4: CTvox examples from 1072 scanner (A) mouse foot, (B) shell, (C) fish, (D) mouse vertebra (red/blue stereo pair), (E) glass fibres in resin, (F) mobile phone SIM card.

We also tried loading the maxilla scans into Imaris 7.0.0 (64-bit) from Bitplane. (This software is normally used for viewing confocal laser scanning microscope Z stack images). We found that although it took a long time to load the scans, especially when compared to CTvox, once loaded they were easily manipulated and that the selection of normal shading surface improved the image. (Fig. 5)

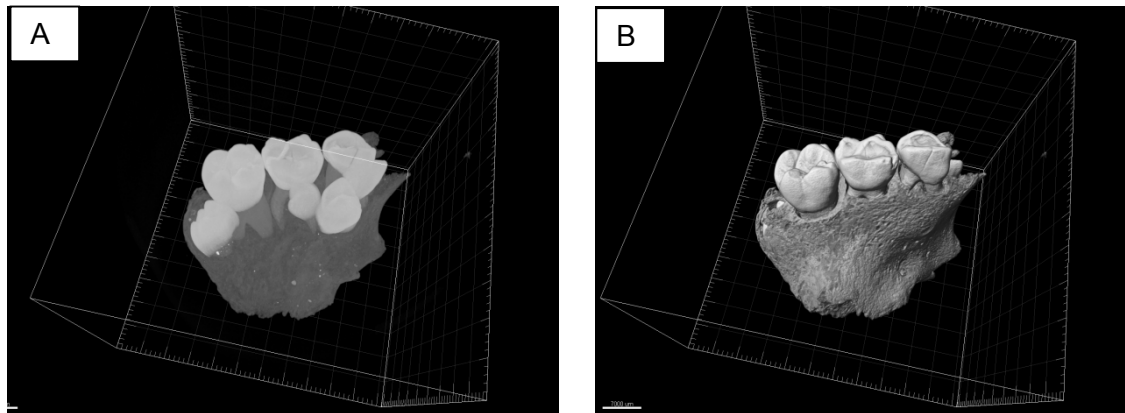


Figure 5: Imaris generated images from maxilla (A) Maximum Intensity Projection volume, (B) normal shading surface

Conclusion

We found that the large datasets could be opened in CTvox without having to resize them.

CTvox is very easy to use and performs well with a fast computer and large graphics card.

It also has many options to slice through image, change surface texture, add shadow and adjust lighting of model, and to easily make movies. It even includes an option to output a file suitable for viewing on Apple mobile devices.

Another option not commonly used in both CTVol and CTvox is the ability to create 3D stereo pairs which can give extra depth detail to the model.

Iterative dual energy reconstruction for noisy microCT images

M. Depypere¹, J. Nuyts², N. van Gastel³, K. Laperre³, G. Carmeliet³, F. Maes¹, P. Suetens¹

¹ Department of electrical engineering (ESAT/PSI)

² Department of Nuclear Medicine,

³ Laboratory for experimental medicine and endocrinology,
Katholieke Universiteit Leuven, Belgium

Aims

Dual energy CT imaging enables discrimination of materials with similar attenuation coefficients. By acquiring two CT scans at different X-ray energies of the same sample, the energy dependence of the linear attenuation coefficient can be exploited to differentiate between materials. Dual energy CT has been widely used to distinguish bone from vascular contrast agents that contain elements with a K-edge in the imaging energy range, such as iodine, barium or lead.

Post-reconstruction decomposition techniques first reconstruct the two sets of projection data separately to obtain two reconstructions at different energies. The difference in attenuation between the energies is then compared to determine the amount of each tissue type in every voxel. Noise affects the reconstructed attenuation values, and negatively influences the tissue decomposition. Obtaining images with high signal-to-noise ratio can require cumbersome long scan durations, cause heat dissipation issues, and induce radiation side effects for in vivo experiments. MicroCT imaging would benefit from a dual energy algorithm that is robust to noise.

Method

Polychromatic attenuation model. As dual energy applications attempt to exploit the dependency of the linear attenuation coefficient μ on the photon energy E , we will model the attenuation coefficient as a linear combination of basis functions. Any material without a K-edge in the imaging energy range can be approximated by a linear combination of two basis functions. A well known set of basis functions are the photoelectric effect $f_P(E)$ and the Compton scatter $f_C(E)$.¹ To describe the attenuation of a K-edge element, a third basis function $f_K(E)$ is required that models the mass attenuation coefficient of the K-edge material. The model then becomes:

$$\mu(E) \approx c_P f_P(E) + c_C f_C(E) + c_K f_K(E)$$

As a result, the energy dependent attenuation of any material can be characterized by the three coefficients c_P , c_C , and c_K , provided that there is only one K-edge material present. The coefficients are shown in Table 1 for some common materials in biological microCT scans. Figure 1 illustrates the basis function decomposition for the attenuation of water, bone and barium sulfate.

Material	c_p	c_c	c_k
Air	1.7e-5	0.0002	0.0
Water	0.0144	0.1793	0.0
Bone	0.1757	0.3109	0.0
Barium sulfate 30gv	0.0	0.0	1.233

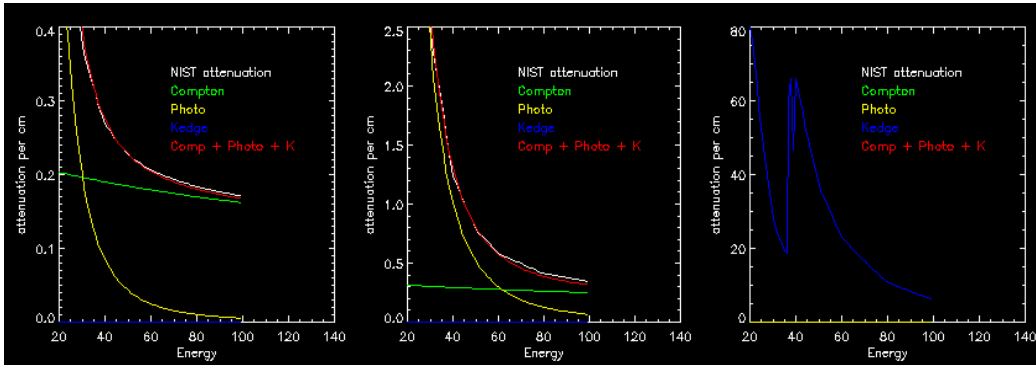
Table 1: Values of c_p , c_c , and c_k for some common materials.

Figure 1: Basis function decomposition for materials water (left), bone (middle) and barium sulfate (right). The white curve is the actual attenuation. The green, yellow and blue curves represent the Compton scatter, photoelectric effect, and K-edge basis functions respectively. The red curve shows the approximated attenuation as the sum of green, yellow and blue curves.

To define the composition of a voxel, three coefficients need to be determined in every voxel of the reconstruction image. This requires three measurements at three different energies. These three measurements can be obtained by taking a third microCT-scan, or in a single scan by using multi-bin photon counting detectors. We adopt the approach of Bruno De Man et al that restricts the relative weights of the photoelectric and Compton basis functions.² Not all combinations of coefficients of these basis functions occur in biological tissue, and we can restrict the allowed combinations. As a result c_p can be computed from c_c and vice versa, and only two unknowns in every voxel remain. With this relationship, the solution can be found with just two measurements at different energies. For more details about this model, we refer to De Man et al.²

Iterative reconstruction method. The goal of the reconstruction is to determine the unknown coefficients c in every voxel. Iterative techniques generally start from a uniform image that serves as estimate of the reconstruction, and iteratively refine this estimation. In each iteration the projections of the current reconstruction estimate are calculated and compared to the measured projections acquired during the microCT scan. The reconstruction estimate is then updated to minimize differences between the calculated and measured projections. To enable modeling of the noise and improving the noise robustness of the algorithm, the reconstruction is formulated in a statistical framework. More details about the iterative reconstruction can be found in Nuyts et al.³

Results

Dual energy microCT scans of two samples are acquired. The settings for the low energy scan are a tube voltage of 50kV and 0.5mm aluminium filtration, while the high energy scan puts the tube voltage at 100kV and uses a filter of 0.5mm aluminium and 0.038mm copper. These filters are used because they are installed by default on our SkyScan 1172 microCT system. The two samples are analysed with both the post-reconstruction approach as described by Granton et al⁴ and the presented iterative decomposition method.

The first sample is a polypropylene tube filled with water that contains a mix of barium sulfate, water and gelatine to prevent sedimentation, and a cylinder of bone equivalent material, calcium hydroxyapatite (CaHA). The filtered backprojection (FBP) reconstruction is noisy (Figure 2a), and the tissue decomposition results in a coefficient of variation of 0.36 in the barium sulfate region (Figure 1b). The iterative approach is more robust to noise in these conditions with a coefficient of variation of 0.15 in the same region (Figure 1c and d). Due to the inhomogeneity of the CaHA, some particles exhibit K-edge behaviour and are detected as such by both methods.

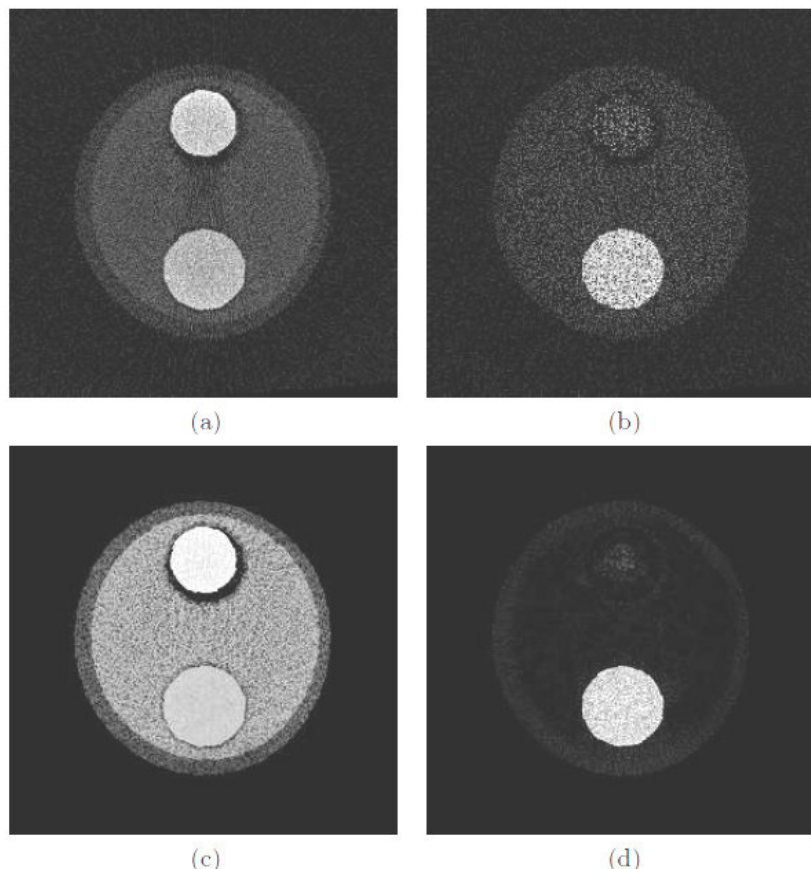


Figure 2: Results of the phantom. (a) FBP reconstruction. (b) Barium sulfate tissue fractions computed by the post-reconstruction approach. (c) Sum of c_P and c_C computed by the iterative method. (d) Barium sulfate coefficients c_K computed by the iterative method.

The method is also tested on an ex vivo mouse tibia perfused with barium sulfate. In the reconstruction of Figure 3a, the two large grey structures represent bone, while the white dots are cross sections of blood vessels perfused with barium sulfate. Due to noise, the post-reconstruction decomposition considers several bone voxels as contrast agent (Figure 3b), while the iterative approach does not suffer from this issue (Figure 3c). The vasculature can be interpreted more easily when viewed as a red overlay on the original reconstruction (Figure 3d)

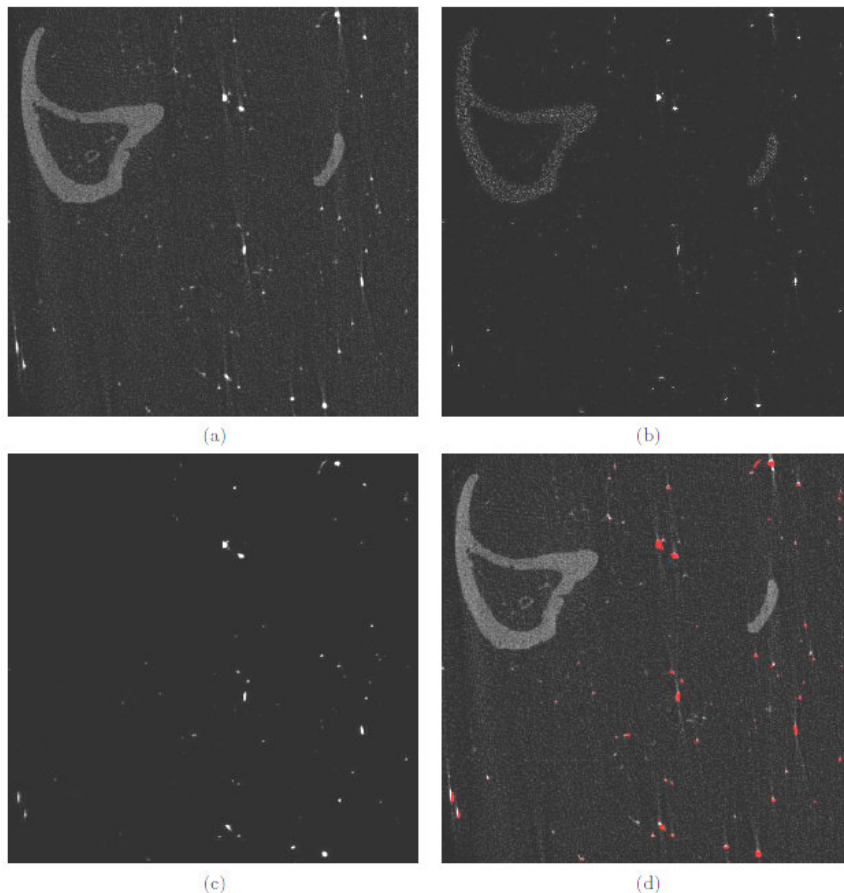


Figure 3: Results of the mouse tibia. (a) FBP reconstruction. (b) Barium sulfate tissue fractions computed by the post-reconstruction approach. (c) Barium sulfate coefficients c_K computed by the iterative method. (d) Overlay of the contrast c_K in red on (a).

Conclusion

We have presented an iterative dual energy reconstruction algorithm that is able to deal with one K-edge material. The method is shown to be able discriminate bone from contrast agent. By reducing the number of unknowns to two per reconstruction voxel, this approach can be applied to any kind of CT scanner. The method performs better than a typical post-reconstruction approach with respect to noise at the expense of increased computation time.

References:

1. Alvarez RE, Macovski A, "Energy-selective reconstructions in X-ray Computerised Tomography", Physics in Medicine and Biology, 21(5), 733-744, 1976
2. De Man B, Nuyts J, Dupont P, Marchal G, Suetens P, "An iterative maximum-likelihood polychromatic algorithm for CT", IEEE Transactions on Medical Imaging, 20(10), 999-1008, 2001
3. Nuyts J, De Man B, Dupont P, Defrise M, Suetens P, Mortelmans L, "Iterative reconstruction for helical CT: a simulation study", Physics in Medicine and Biology, 43(4), 729-737, 1998
4. Granton PV, Pollman SI, Ford NL, Drangova M, Holdsworth DW, "Implementation of dual- and triple-energy cone-beam micro-ct for postreconstruction material decomposition", Medical Physics, 35(11), 5030-5042, 2008

Can combined CT and TOF-MRI assist in neuro-anatomical surgery planning in small animal models?

G. Vande Velde^{1,2}, J.R. Rangarajan^{2,3}, K. van Kuyck⁴, T. Dresselaers^{1,2}, U. Himmelreich^{1,2}, B. Nuttin⁴, F. Maes^{2,3}, P. Suetens^{2,3}

¹ Biomedical NMR Unit, ² Molecular Small Animal Imaging Center (MoSAIC), ³ Medical Image Computing (ESAT/PSI), ⁴ Laboratory for Experimental Functional Neurosurgery, K. U. Leuven, Belgium.

Aims

Deep brain stimulation (DBS) for neurological and psychiatric disorders like Parkinson's disease or major depression disorder requires the implantation of electrodes for the application of electrical pulses in deep brain anatomical locations. For such procedures, pre-operative or intra-operative multi-modality brain magnetic resonance imaging (MRI) or computed tomography angiography (CTA) images of the individual patient are extensively investigated to define the optimal trajectory for electrode insertion to avoid vasculature and functionally important brain areas. Unlike DBS in humans, planning of brain interventions in preclinical rodent models is typically restricted to defining the target and entry points in a generalized anatomical small animal brain atlas¹ and transforming these onto the individual animal using a stereotactic reference frame. As current atlases provide limited or no blood vessel information, the outcome of neurosurgical small animal model experiments could be deleteriously influenced when a sub-optimal electrode trajectory ruptures the cerebral vasculature resulting in severe systemic effects. However, the feasibility of individual pre-operative imaging-based surgical path planning in animal studies is limited. Therefore, we aim to build a stereotactic (probabilistic) atlas based on anatomical (CT, MRI) and cerebral vasculature (TOF-MRI, CTA) information that can be used for neurosurgical planning (e.g. electrode implantation), without requiring the acquisition of vasculature and anatomical reference images for each individual animal. Here, we validate vasculature information from TOF-MRI with CT(A) and assess the intra-strain variability in skull reference points and cerebral vasculature for neurosurgery planning and subsequent (probabilistic) atlas building. Using this atlas, we aim to evaluate the risk of a user defined electrode trajectory damaging a blood vessel on its path. The use of such a method will be readily applicable to DBS in small animal models and also to a wide range of stereotactic surgeries like targeted injection of viral vectors, contrast agents, cells for the creation of neural disease models and *in situ* cell labeling applications.

Method

In vivo 3D anatomical MR brain images and 2D multi-slice MR angiography (MRA) time-of-flight cerebral angiography images (FLASH-TOF, isotropic resolution of 195 μm) were acquired for 10 male Wistar rats in a 9.4T Bruker small animal MRI scanner. *In vivo* and *ex vivo* CT images of the full rat head were acquired on a SkyScan1076 small animal CT scanner. *In vivo* CT images of the full rat skull were acquired from isoflurane gas-anesthetized rats (3% for induction, 1.8 % for maintenance), positioned with bregma in the center of the FOV, using the following parameters: 35 μm isotropic resolution, 49 kV source voltage, 200 μA source current, 0.5 mm Al filter, 180 ms exposure time, 0.8° rotation step, 2 averages, 2 connected scans to cover the complete rat skull length (this is important to include enough landmarks for coregistration such as lambda, bregma, nasal suture,...). After the last *in vivo* imaging time point, rats were sacrificed by administration of an overdose of anaesthesia (i.e. nembutal, to which 20% heparine was added to avoid blood clotting) and

transcardially perfused, first with heparinized saline to flush the blood away, than with paraformaldehyde (4% in PBS) to fix the tissue, followed by a saline flush and in a last step with 30% BaSO₄ (in 2% gelatine) as a blood pool contrast agent for *ex vivo* CTA. We are currently evaluating a second perfusion protocol that would allow us to visualize the vessel tree on histological tissue sections. To this end, the BaSO₄ in the final perfusion step is mixed with liquid latex and waterproof black drawing ink. *Ex vivo* CTA images were acquired from the packed specimen with the following parameters: 35 µm isotropic resolution, 100 kV source voltage, 100 µA source current, 1 mm Al filter, 220 ms integration time, 0.7° rotation step, 3 averages, 2 connected scans to cover the complete rat skull length.

We used an in-house developed image analysis pipeline^{2,3} for image pre-processing (e.g. RF intensity inhomogeneity correction) and spatial normalization of MR and CT anatomical images, MRA and CTA vasculature images and reference atlas template images. A vasculature average image was constructed in atlas space (figure 1). We use *ex vivo* CTA for validation of the MRA-TOF. For the planning of stereotactic surgery, the targets are visualized in the Paxinos-MR template along with the multi-modality information of MR/CT anatomical and MRA images normalized to atlas space. The risk of the electrode damaging the vasculature is computed by representing vessels and electrodes in terms of Euclidean distance maps. A 2D automatic ray casting approach with potential trajectories radiating from the target point towards the skull is presented with associated information on the vasculature along each path. The coordinates of entry point, the angle of entry and the depth of incision along with the associated risk (maximum intensity and averaged sum-of-pixel intensities along trajectory) are presented to the user (figure 1, E).

Results

The information from multi-modality (MRI, CT and atlas) images of anatomy, vasculature and stereotactic coordinates was combined to realize an optimal 3D planning for stereotactic neurosurgery in rodents (figure 1).

Larger vessels are consistently visualized in all the TOF-MRI images that were processed and their geometric location is nearly identical. Depending on minor modifications in the animal position within the MRI scanner, some sections of the vessel tree were less visible for some animals compared to the others.

An average vasculature template has been constructed from the MRA-TOF images in the atlas space. The CT data serves as ground truth for validation of this vasculature atlas (*ex vivo* CTA) and for evaluation of the variability of bregma (*in vivo* and *ex vivo* CT). Visual comparison of the MRA-TOF vasculature (major vessels) in individual animals indicates minimal variability. This could indicate the feasibility to use the vasculature template as a representative of the population for more precise planning of stereotactic surgeries like the DBS application. To validate this objective, we used the multi-modality information to plan stereotactic surgery using a potential risk path and an estimated safe trajectory (figure 1, E). From these experiments we know that for optimal planning of stereotactic surgery (e.g. electrode implantation), coregistration of MRI/MRA images with CT data on bregma and lambda reference points on the skull is highly important. Therefore, information (CT) on the variability of bregma will be combined with the vasculature data in the atlas.

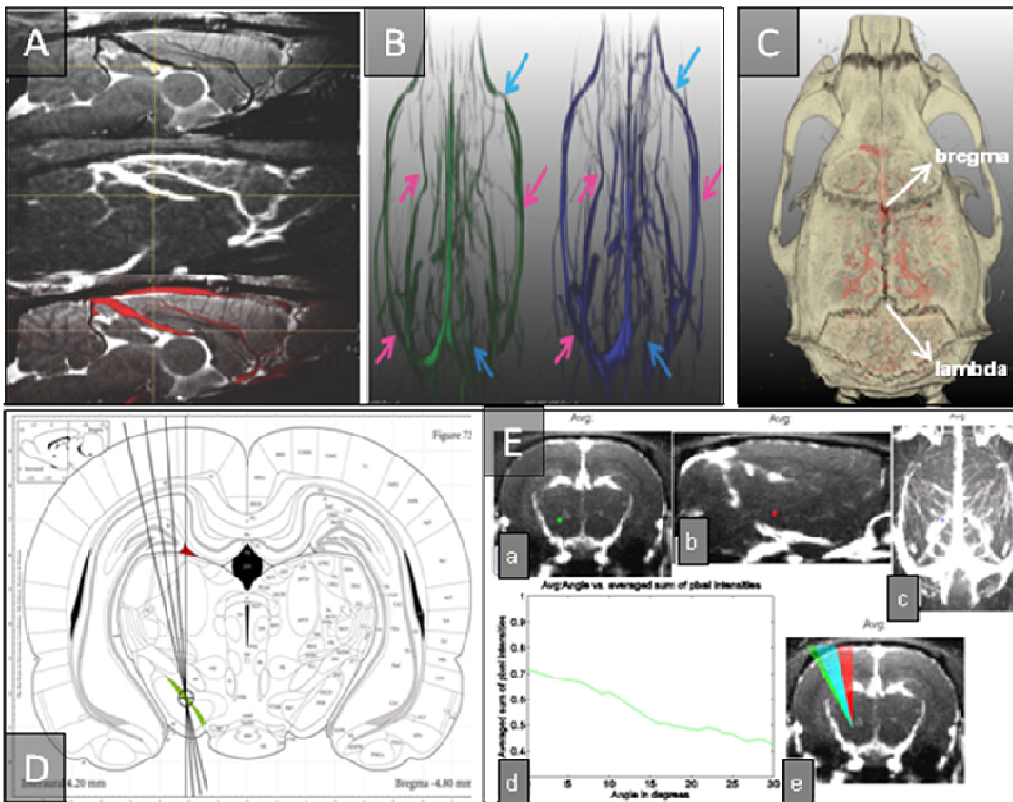


Figure 1: (A) Coregistration between MRI (top), MRA (middle) and MRI-MRA (bottom, red overlay). (B) 3D volume rendering of MRA images of the same 2 animals. Arrows indicate regions of similarity (pink) and variability (blue). (C) CT images providing information on bregma and lambda reference points and vasculature for validation of MRA. (D) Surgery planning in 2D (Paxinos) atlas space with possible trajectories at different angles. (E, a-c) Average vasculature images in atlas (Paxinos) space: the maximum-intensity MRA-TOF vasculature information constructed from 4 consecutive slices at the same location, with * marking the green target region. (d) Risk assessment: the averaged sum-of-pixel intensities along each of the trajectories determine the associated risk of the electrode traversing through hyperintense pixels (=vasculature in TOF-MRI). Based on the averaged sum-of-pixel intensities along each of the trajectories, the paths are color-coded: high (red) - medium (cyan) – lower risk (green) (e).

Conclusion

For pre-clinical stereotactic surgeries, optimal trajectory planning is valuable input to avoid injuring vasculature. We address this issue by investigating the intra-strain variability in cerebral vasculature combined with the position of bregma for the Wistar rat strain. Provided that the intra-strain variability is small, a probabilistic vasculature atlas for the given strain could form a reference for brain surgery planning. We use image registration to spatially align multi-modal anatomical and vasculature information from age and weight matched animals from the same strain to the common reference frame in a standard atlas space. Excluding the acquisition effects, we observe consistency with vasculature for the test group. We demonstrate the methodology for building a vasculature template and subsequent use for planning neuromodulation experiments. We are currently extending this study with more animals, where validation of the proposed safe and risk paths through stereotactic surgeries, together with validation with CTA using contrast agents, are pursued not only for electrode insertion but also for the injection of cells and viral vectors.

References:

2. Paxinos, G. and Watson, S., "The rat brain in stereotaxic coordinates", Elsevier Academic Press, 2005.
3. Vande Velde, G., Rangarajan, J., Toelen, J., Dresselaers, T., Ibrahim, A., Krylychkina, O., Vreys, R., Van der Linden, A., Maes, F., Debysen, Z., Himmelreich, U., Baekelandt, V., "Evaluation of the specificity and sensitivity of ferritin as an MRI reporter gene in mouse brain using lentiviral and adeno-associated viral vectors," Gene therapy [in print], 2011.
4. Rangarajan, J., Loeckx, D., Vande Velde, G., Dresselaers, T., Himmelreich, U., and Maes, F., "Impact of rf inhomogeneity correction on image registration of micro mri rodent brain images," 8th IEEE international symposium on biomedical imaging [in print], 2011.

Quantitative multi-pinhole small-animal SPECT with U-SPECT-II/CT

C. Wu¹², H.A.F. Gratama van Andel²³, J.R. de Jong¹, P. Laverman⁴, R.A.J.O. Dierckx¹, F.J. Beekman²³⁵

¹ Department of Nuclear Medicine & Molecular Imaging, University Medical Center Groningen, University of Groningen, Hanzeplein 1, 9713 GZ Groningen, The Netherlands,

² Image Sciences Institute and Rudolf Magnus Institute, University Medical Center Utrecht, Universiteitsweg 100, 3584 CG Utrecht, The Netherlands

³ MILabs B.V., Heidelberglaan 100, 3584 CX Utrecht, The Netherlands

⁴ Department of Nuclear Medicine, Radboud University Nijmegen Medical Center, Geert Grooteplein 10, 6525 GA, Nijmegen, The Netherlands

⁵ Department Radiation, Radionuclides & Medical imaging, Delft University of Technology, Mekelweg 15, 2629 JB Delft, The Netherlands

Aims

Small-animal SPECT plays an important role in biomedical research. Accurate and reliable quantitative imaging with small animal SPECT can help scientists with understanding the behavior of organs, tissues and pharmaceutical *in vivo*, which is a good motivation for developing accurate correction methods for photon attenuation. Previous phantom assessments¹⁻² show that photon attenuation reduces the measured activity concentration in the center of rat-sized and mouse-sized phantoms by up to 25% and 18% with Tc-99m, respectively. These studies lead to the conclusion that the attenuation compensation, together with correction for other image degrading effects, is required in order to consistently achieve accurate quantitative small-animal SPECT images. We here propose a CT-based modified non-uniform Chang³ method for attenuation correction and evaluate this method with phantom studies in a U-SPECT-II/CT system (with an integrated Skyscan 1178 single-source system)⁴. The necessary information for calculating attenuation correction maps was derived from registered X-ray CT images of the phantom.

Method

First a SPECT scan was made in the U-SPECT-II/CT system of a small drop of a solution containing 57.2 MBq Tc-99m to obtain the calibration factor of the SPECT system. Later on a 30-mm NEMA-small-animal phantom filled with 8.66 MBq/ml Tc-99m solution was scanned with both the SPECT and CT modalities. List-mode SPECT data were acquired and a scatter-corrected SPECT image was reconstructed by using the pixel-based ordered subset expectation maximization (POSEM⁵) algorithm combined with a triple-energy-window (TEW⁶)-based scatter correction. A CT image was also reconstructed in Hounsfield unit (HU) and registered to the SPECT image.

The attenuation coefficient (μ) at the location of each voxel was derived from the registered CT image, by employing a linear scaling of the HU numbers:

$$\mu = \mu_0 \left(\frac{HU}{1000} + 1 \right),$$

where μ_0 is the attenuation coefficient associated with water and the energy of the photons used in SPECT. In the case of Tc-99m studies, μ_0 equals 0.151 cm^{-1} .

The amount of attenuation was quantified by the transmitted fraction (TF) which is the ratio of detected counts with attenuation to the counts in an ideal attenuation-free situation. In the modified non-uniform Chang³ method, the overall TF of each voxel in a SPECT image is

treated as the average of TFs along different projection trajectories starting from that voxel. Along each projection line, the TF is simply computed as the line integral of the attenuation coefficient on that line. The calculation above is represented as the following equation:

$$TF = \frac{1}{M} \sum_{m=1}^M \exp \left(- \int_{L_m} \mu(l) dl \right)$$

in which M is the number of projections in acquisition for a certain voxel, L_m denotes the m-th projection path of gamma photons, and $\mu(l)$ is the attenuation coefficient as a function of location l on that projection line L_m .

With the scatter-corrected image voxels (SC), the calibration factor (CF) and the overall transmitted fraction (TF), the attenuation-compensated image (AC) was given by:

$$AC = \frac{SC \cdot CF}{TF}.$$

Results

Figure 1(a) shows uniform and non-uniform slices of the NEMA phantom from un-corrected and attenuation-corrected SPECT images. Figure 1(b) shows their corresponded CT slices, and the derived attenuation correction maps (slices of transmitted fraction values) are illustrated in Figure 1(c).

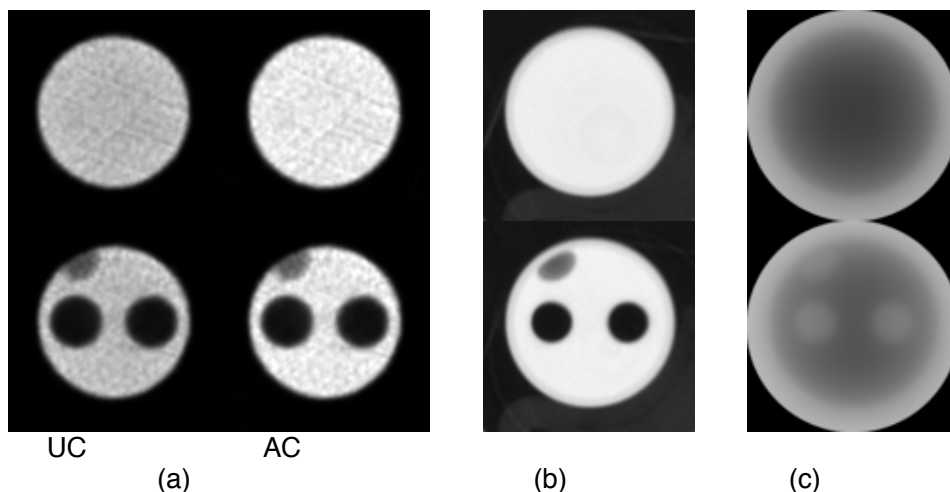


Figure 1: Slices and attenuation correction maps. (a) un-corrected (UC) and attenuation-corrected (AC) SPECT slices. (b) CT slices. (c) attenuation correction map derived from the CT slices.

The transmitted fraction values in the attenuation correction maps demonstrated about 20~23% attenuation in the center area of the phantom, which is consistent with literature¹⁻², and indicating that the attenuation correction is important for quantification even in small-animal SPECT. The quantitative errors are visualized more clearly by using line profiles in Figure 2. The average quantification error of the entire phantom volume was -16.2% without attenuation correction, and was reduced to 4.7% with attenuation correction.

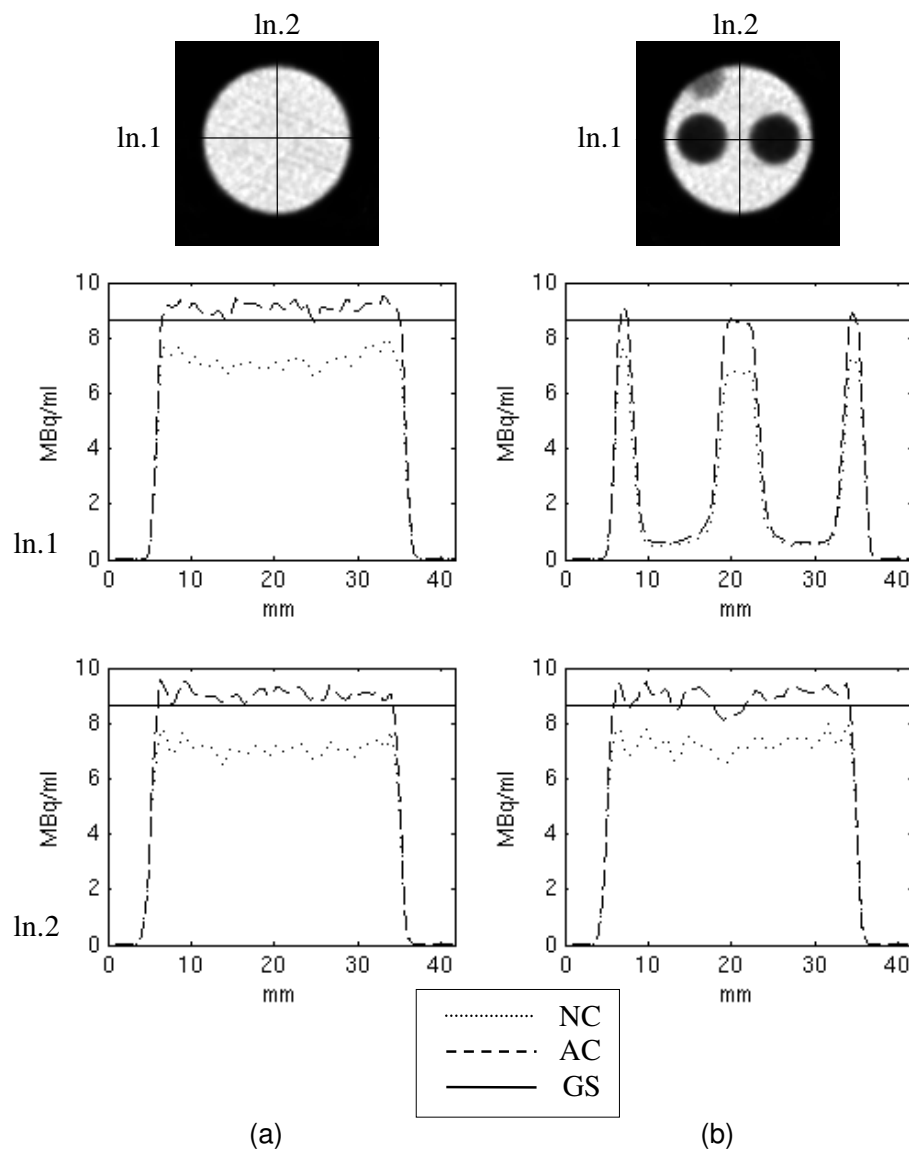


Figure 2: Line profiles in (a) uniform slice and (b) non-uniform slice. NC: without attenuation correction. AC: with attenuation correction. GS: gold standard obtained with dose calibrator.

Conclusion

The effects of attenuation in small-animal SPECT can be corrected by using the CT-based non-uniform Chang method in the U-SPECT-II/CT system, with a good accuracy of less than 5% error on average.

References:

1. A.B. Hwang, et al., "Assessment of the sources of error affecting the quantitative accuracy of SPECT imaging in small animals", Phys Med Biol, 53, 2233-52, 2008
2. C.L. Chen, et al., "Toward quantitative small animal pinhole SPECT: assessment of quantitation accuracy prior to image compensations", Mol Imaging Biol, 11, 195-203, 2009

3. L.T. Chang, "A method for attenuation correction in radionuclide computed tomography", IEEE Trans Nucl Sci, 25, 638-43, 1978
4. F. van der Have, et al., "U-SPECT-II: An ultra-high-resolution device for molecular small-animal imaging", J Nucl Med, 50(4), 599-605, 2009
5. W. Branderhorst, et al., "Pixel-based subsets for rapid multi-pinhole SPECT reconstruction", Phys Med Biol, 55, 2023-34, 2010
6. K. Ogawa, et al., A practical method for position-dependent compton-scatter correction in single photon-emission CT, IEEE Trans Med Imaging, 10, 408-12, 1991

Software Clearing CT Data from Effects of Instrumental Resolution

J. Dyson¹, V. Calbucci¹, F. Pasqualini¹, G. Albertini¹, F. Fiori¹, F. Rustichelli¹

¹ Università Politecnica delle Marche, Via Brecce Bianche, Ancona, 60100, Italy

Aims

The practical implementation and development of the EU BIO-CT-EXPLOIT⁵ software for clearing CT data from effects of instrumental resolution [2] adds a unique and specific capability to the in house analysis GUI package "CTan" provided by SKYSCAN with its tomographic scanning equipment. Programmed in-line to sit on the "plugin" panel of the analysis package for importing tomographic image slices direct from the machine, it is a fully automated image enhancement algorithm requiring little or no expertise from the user, making it fast and easy to use in single image or indeed batch mode. The images produced use the histogram equalization technique to remove the instrumental error as documented in [1]. These may then be further processed by the main body of the SKYSCAN package according to requirement and then visualized as three-dimensional reconstructions of the computed tomography (CT) process. The incremental advances in technology in today's market are so hard fought for that we feel confident that the unique technologies employed in this plugin concept designed for SKYSCAN will deliver a vital pre-processing step towards increasing the capability and applicability of CT scanner machines.

Method

Scientific Aspects

The presence of air inside the voids or cavities of a computed tomography (CT) sample introduces errors in the form of distributed noise in the two-dimensional output grey scale absorption image of the slice. These show up as a separate characteristic peak in the histogram of that image. According to the theory expounded in [1] the corrected image histogram is obtained by using the characteristic air error peak as the kernel in a one dimensional deconvolution operation [3] upon the original histogram. This histogram can then be mapped back to a corrected image using a variety of techniques. A very good, commonly used, method is to implement a histogram equalization (HE) [4] to derive the corrected image itself.

⁵ EU-FP7 project BIO-CT-EXPLOIT entitled „Innovative simulation tool for bone and bone biomaterials“, based on enhanced CT-data exploitation, information online at <http://bio-ct-exploit.imws.tuwien.ac.at/>

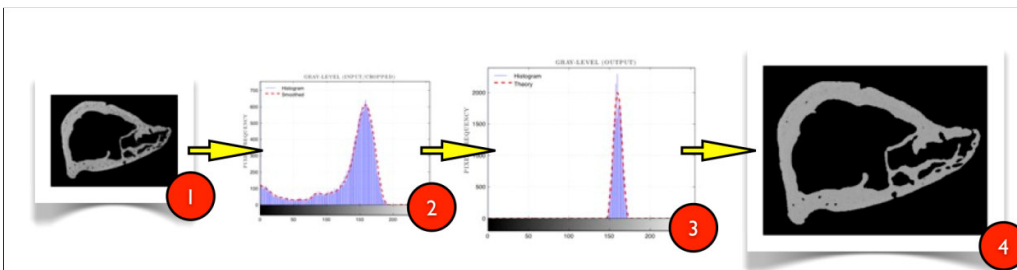


Figure 1: The image treatment schematic. (1) The SKYSCAN CT image is loaded and extraneous details removed (2) The gray-level histogram of the pre-processed image is extracted and the leftward peak (half peak at the far left) identified as the air error peak (3) The deconvolution with the air error peak effected to generate the dotted line (4) The HE process converts the new histogram into the corrected image.

Integration into SKYSCAN software

The process chain given in Figure 1 is actually implemented in the MATLAB environment as a part of the EU BIO-CT-EXPLOIT effort. We are presently converting it into a plugin format for the SKYSCAN scanner image processing software written in Microsoft's Visual C++ computer language. The C++ language is very fast and intricate from the programmer's perspective, giving strong and safe control over the computer functions. The development environment provided by Microsoft and used by SKYSCAN is an established standard in such program development projects. It permits the development of software as a seamless part of the MS Windows operating system using all the graphical user elements for maximum compatibility in the target market as well as ease of use.

This implementation gives the user an option to preprocess CT image(s) in a new way as laid out in [1] to be effectively better approximations, delivering effectively a more accurate and relevant absorption map of the material. The entire chain summarized in Figure 1 has been built to run without user intervention. The underlying processes are complicated and require much knowledge of certain numerical analysis techniques to produce the treated images. Thus intervention by the user would be a time consuming process and defeat the purpose of preprocessing in this way [2]. Complete automation is fast and batch processes can also be devised which, apart from the theoretical utility of the procedure, make it practical and a step forward when implemented and distributed as a plugin.

The MATLAB implementation has a certain object model that is very useful for testing as well as an image processing toolbox. The image processing libraries have therefore been self-contained as a part of the MATLAB environment for the duration of beta development. The transformation into a C++ plugin according to the SKYSCAN requirements needs a complementary image-processing library as strong as that of MATLAB (all the functions cannot hoped to be duplicated even so, but we can custom write the missing routines to retain the original functionality). To avoid licensing issues we chose a free library available on the internet as "CIMAGE" and immediately this provided a great deal of implementation strength. There are compatibility drawbacks involved; the main one being that the library is new while the compilation of the SKYSCAN C++ software was old by almost a decade. Our first challenge has therefore been to cast a compatibility framework linking the CIMAGE library to the SKYSCAN plugin code frame. This has been now done and a transparent

process pipeline from the MATLAB routines to their C++ counterparts achieved. Images can be loaded and processed in an equivalent way without trouble.

This opens the way for custom development of the plugin to exact requirements as specified by SKYSCAN. We are therefore engaged in a two way process of duplicating the original MATLAB beta functionality in C++ for the plugin, and indeed improving upon that functionality where C++ provides a significant gateway to do so. The result will be a fast and streamlined preprocessing package for a commercial endeavor, which is extensible and useful for analysis of CT scanner images in the engineering and medical fields as was laid out in the image clearing aspect of the EU BIO-CT-EXPLOIT project specification (see Figure 2 as well as [2]).

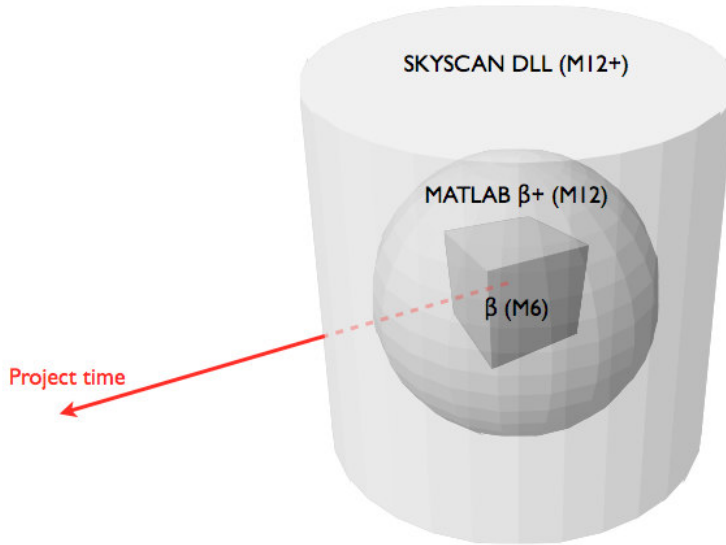


Figure 2: An illustration of the BIO-CT-EXPLOIT “Software for clearing CT data from effects of instrumental resolution” project timeline with increase in demonstrator/deliverable platform capacity shown as the volume of the shapes at each projected stage.

Results

The MATLAB beta delivers a complete implementation of the BIOCT image-clearing pipeline. This is shown in Figure 1 in its schematic form. The complete MATLAB GUI we present in Figure 3 below.

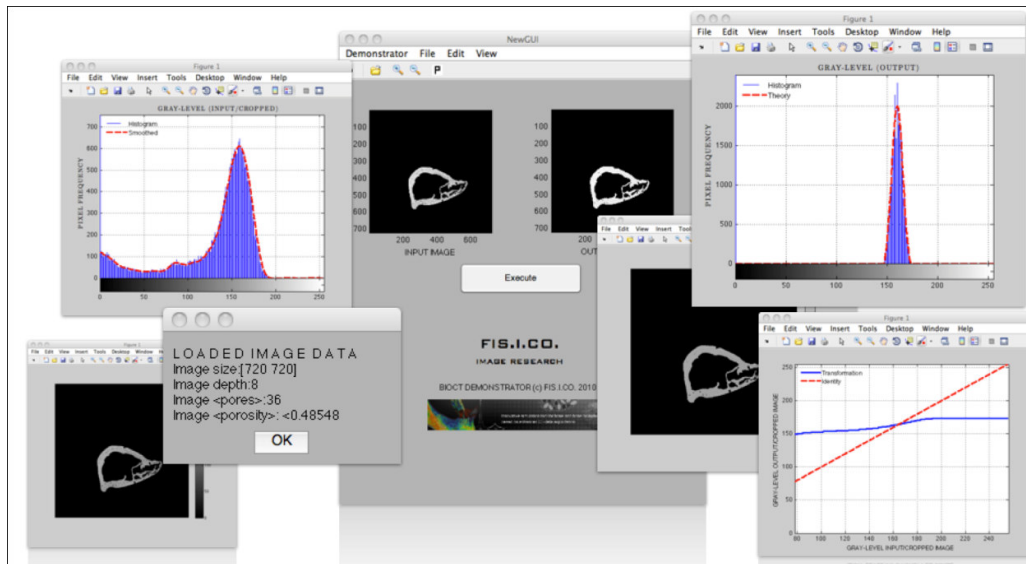


Figure 3: An illustration of the BIO-CT-EXPLOIT project “Software for clearing CT data from effects of instrumental resolution” MATLAB beta demonstrator as implemented at month 12.

The most recent developments in the project actually come from the C++ plugin framework that is referred to in the section above. Figure 4 is a glimpse of the framework in action on a SKYSCAN raw CT image; The framework is here implemented as a plugin already mounted and running in the SKYSCAN CTan environment showing the CIMAGE library “histogram” operation on the loaded image.

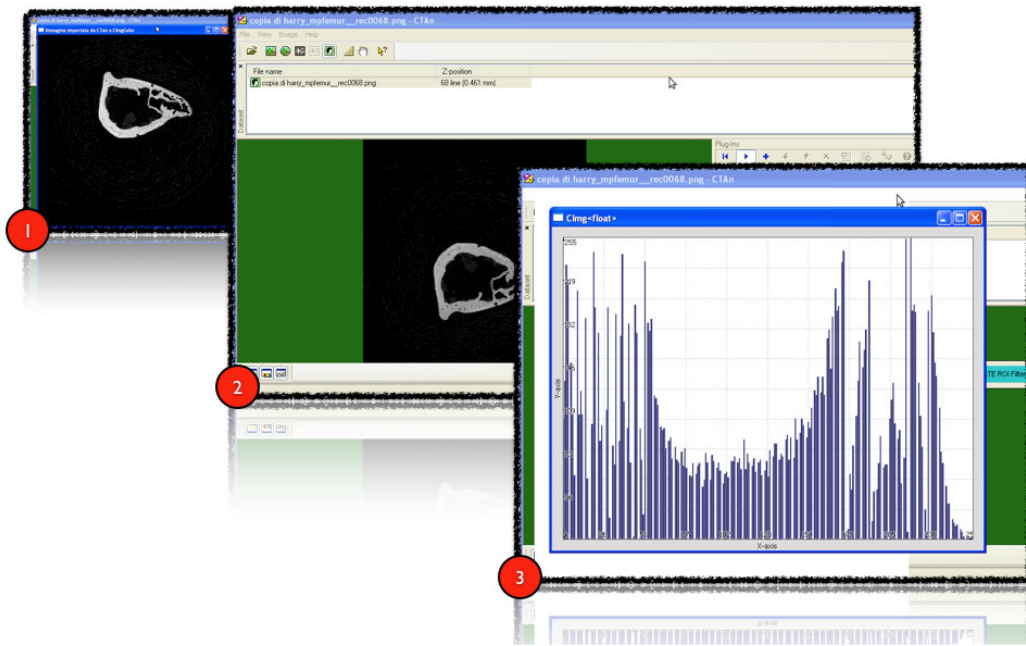


Figure 4: An illustration of the BIO-CT-EXPLOIT project “Software for clearing CT data from effects of instrumental resolution” SKYSCAN plugin GUI at its most recent development stage. (1) The SKYSCAN image is loaded into the CIMAGE library using the compatibility framework code. (2) The forgoing image is connected “live” to the SKYSCAN CTan environment. The Plugin buttons are the sub-toolbox on the far-right of the window. (3) A CIMAGE histogram operation extracts the image histogram for the user.

These results – for brevity here - hide much additional functionality available due to the sub-processing stages carried out to get the final image (Stage 4 in Figure 1 above). The details available in the sub-processing stages provide new ways of extracting information from images. This information can greatly aid the end user analysis by providing information such as estimated bone porosity as well as the probability distribution of pores in the CT image. That level of functionality is usually found in larger and more expensive analysis suites such as Visual Studio Max. In this context, one can by all means develop it as a further project to provide automated extraction of physical parameters from the bone image in a cheap and automatic manner.

Conclusion

The EU BIO-CT-EXPLOIT “Software for clearing CT data from effects of instrumental resolution” sub-specification has given rise to a unique opportunity in the image processing of CT produced two dimensional image slices for bone like materials. The coming together of the MATLAB, SKYSCAN and C++ computer technologies have proved an ideal cross platform for the integrated development of digital image processing enhancements to that connect the scientific discipline to the commercial technology distribution pipeline through SKYSCAN for example. This process has streamlined and made more efficient the path from research science to benefits realized by the public.

There are novelties associated with the image processing science behind these developments. This is particularly the case for the physical reinterpretation of so-called "image morphology" operations, which has allowed us to usefully extract porosity information hidden in the images. Further to this, the whole process is automated and can operate on batches of images in a wide variety of formats [2]. At every stage in Figure 1 a series of different sub-processes can be said to exist. These, quite apart from safeguarding automation, provide detailed information to the user about every transformation made should he or she require it. Included are the image histograms and their analytical approximations as well as the theoretical and measured final image histograms (Figure 1, stage 3). There is also the actual HE transformation curve that can be requested in the software as well as several different technical data like the Otsu background level [5] and the region of interest mask based on the porosity evaluation.

In all we feel that the integration of these technological developments into the plugin software currently being developed for SKYSCAN will provide a significant and unique advancement to the CT image preprocessing technology currently available in the market.

References:

[1]

Stefan Scheiner, Raffaele Sinibaldi, Bernhard Pichler, Vladimir Komlev, Chiara Renghini, Chiara Vitale-Brovarone, Franco Rustichelli and Christian Hellmich „*Micromechanics of bone tissue-engineering scaffolds, based on resolution error-cleared computer tomography*”, Biomaterials, Volume 30, Issue 12, Pages 2411-2419, April 2009

[2]

EU-FP7 project BIO-CT-EXPLOIT entitled „*Innovative simulation tool for bone and bone biomaterials, based on enhanced CT-data exploitation*“ (coordinator: Christian Hellmich), information online at <http://bio-ct-exploit.imws.tuwien.ac.at/>

[3]

Lucy L. B., “*An iterative technique for the rectification of observed distributions*”, The Astronomical Journal, Volume 79, No 6, June 1974

[4]

AI Bovik, “*The Essential Guide to Image Processing*”, AP Press, ISBN: 978-0-12-374457-9

[5]

Nobuyuki Otsu (1979). "A threshold selection method from gray-level histograms". *IEEE Trans. Sys. Man., Cyber.* 9: 62–66

Translation of CT data into voxel-specific micromechanics-based elasticity tensors

A. Fritsch¹, A. Dejaco¹, V. Komlev^{2,3}, W. Swieszkowski⁴,
J. Jaroszewicz⁴, E. Bongaers⁵, Ch. Hellmich¹

¹ Vienna University of Technology, Institute for Mechanics of Materials and Structures, Vienna, Austria,

² A. A. Baikov Institute of Metallurgy and Materials Science, Russian Academy of Sciences, Moscow, Russian Federation

³ InMatrixs, Moscow, Russian Federation

⁴ Warsaw University of Technology, Faculty of Materials Science and Engineering, Warsaw, Poland

⁵ Skyscan NV, Kontich, Belgium

Aims

The use of computer tomography (CT) imaging is steadily increasing in the ever growing bone implant/surgery and tissue engineering market, although commercial exploitation of CT data for structural design purposes is still based on trial-and-error approaches. This is because X-ray attenuation information is reduced to geometric grey level evaluation, and mechanical properties such as stiffness are often derived from empirical regression functions between grey values, mass density, and elastic constants. As a remedy, we here introduce a technique for (i) conversion of voxel-specific attenuation coefficients into chemical composition, and (ii) translation of these volume fractions, via micromechanics laws, into voxel-specific, inhomogeneous and anisotropic material properties. The application of this method is demonstrated for two classes of materials, namely commercial ceramic (carbonated hydroxyapatite) bone biomaterials, and extracellular bone matrix. Currently, this technique is being made compatible with the commercial software of SKYSCAN.

Method

Commercial porous biomaterial granules made of synthetic carbonate-substituted hydroxyapatite¹ for bone replacement or tissue engineering, with two different diameter size distributions of 0.7 and 2 mm, were scanned with a micro-CT scanner (Skyscan 1172, Skyscan, Belgium) at a resolution of 3.49 μm . A mouse femur was scanned with a micro-CT scanner (Skyscan 1172) at a resolution of 6.78 μm .

The grey scale values (GS) of a computer tomographic image are linearly related to voxel-specific X-ray attenuation coefficients μ , the attenuation coefficient of one voxel is the sum of the attenuation coefficients of the single constituents within this voxel, weighted by their volume fractions. These two basic relationships are used for computing the voxel-specific (nano)porosity of ceramic bone biomaterials, and the composition of extracellular bone matrix, in terms of the volume fractions of the bone mineral (hydroxyapatite), of the organic matter (90% of which is collagen), and of the water in the nanopores spaces between the collagen molecules or the mineral crystals.

For computing voxel-specific elasticity tensors from the aforementioned voxel-specific chemical information, we use homogenization procedures in the framework of continuum micromechanics³. As concerns the carbonated hydroxyapatite biomaterial, a single-step homogenization scheme is employed^{4,5}. Within a material volume (representative volume element – RVE) with a characteristic length of several microns (coinciding with the considered voxel), we discern, as material phases, spherical pores and solid crystals. The latter are represented as spheres, needles, or discs. Besides shape, the material phases are

characterized by their volume fractions (nanoporosity for the pores, and the rest of the RVE filled by the crystals), by “universal” (sample-independent) stiffnesses (zero for the pores, and that of hydroxyapatite for the crystals), as well as by their interactions, here by direct mechanical interaction as in a polycrystal (mathematically realized by means of a self-consistent scheme). As concerns the extracellular bone matrix of the mouse femur, the volume fractions of hydroxyapatite, of collagen, and of water plus non-collageneous organics serve as input for a multistep homogenization scheme for the elasticity of bone materials⁶, which is based on ‘universal’ (tissue-independent) elastic properties of hydroxyapatite, of water, and of collagen. The first homogenization step refers to an observation scale of several nanometers, where crosslinked collagen molecules form a contiguous matrix, which is ‘perforated’ by intermolecular, water-filled spaces. We call the homogenized material ‘wet collagen’. At the fibrillar observation scale (100-500 nanometers), wet collagen and mineral crystal agglomerations penetrate each other, building up the mineralized fibril. The last homogenization step refers to a material volume with 5 to 10 microns characteristic length (coninciding with the considered voxel), where mineralized fibrils are embedded as inclusions into the extrafibrillar mineral foam (a porous polycrystal), forming together the extracellular bone matrix. For each scale, the morphology of the phases is defined in terms of spheres or cylinders, and a suitable homogenization scheme is considered: the Mori–Tanaka scheme is used for composite materials such as the extracellular bone matrix or wet collagen, and the self-consistent scheme is employed for all other material volumes (with polycrystalline morphology).

Results

Colour representations of (nano)porosity of biomaterials and of volume fractions of extracellular bone matrix are depicted in Figures 1 and 3. The corresponding distributions of isotropic elasticity in case of ceramic biomaterials, and of transversely isotropic elasticity in case of the mouse femur, are shown in Figures 2 and 4.

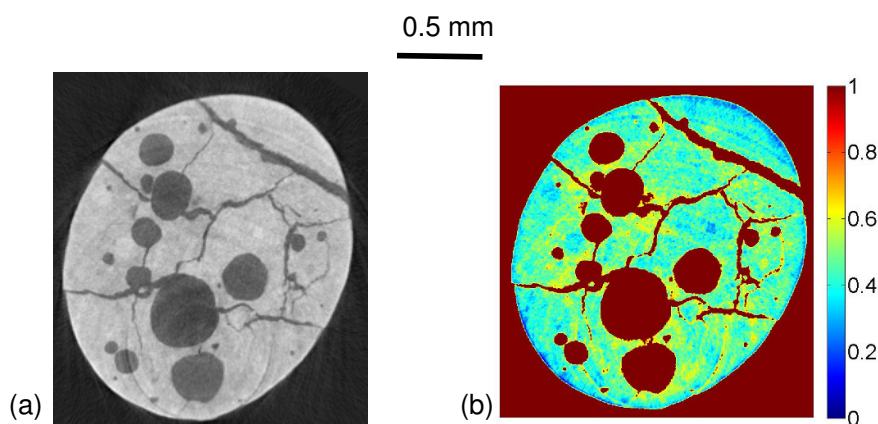


Figure 1: Reconstructed micro-CT image of a ceramic bone biomaterial (voxel size 3.49 microns): (a) typical slice, and (b) colour representation of (nano)porosity for one image

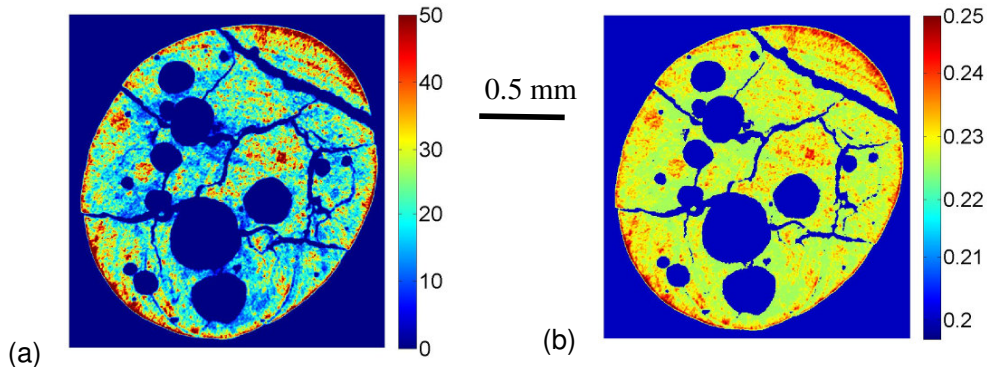


Figure 2: Distribution of voxel-specific isotropic elasticity in the ceramic bone biomaterial depicted in Figure 1, in terms of colour representations of (a) Young's modulus [GPa], (b) Poisson's ratio

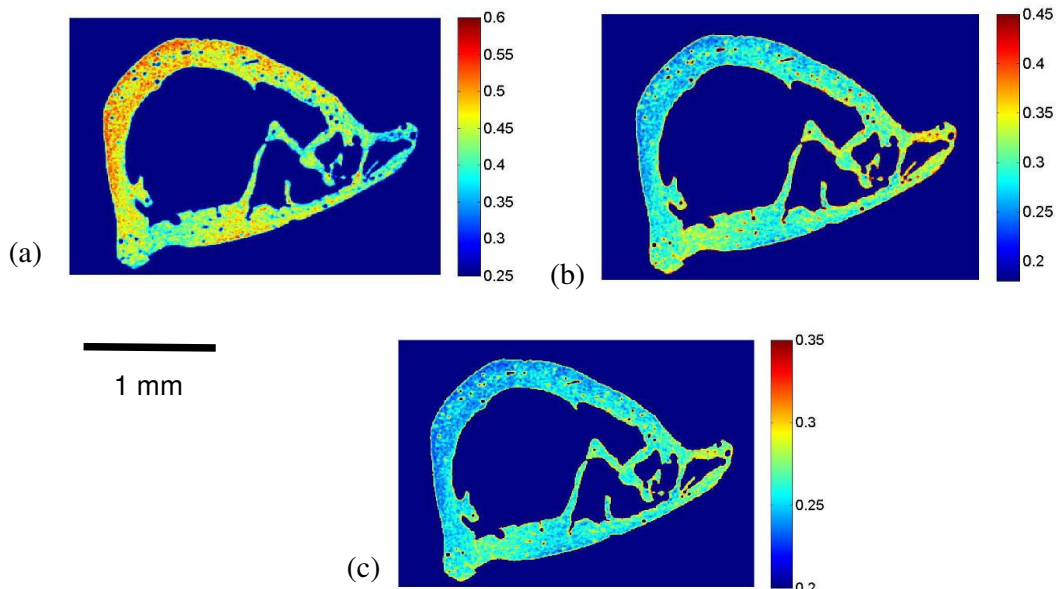


Figure 3: Colour representation of volume fractions of (a) bone mineral, (b) organic matter, and (c) water, for a micro-CT image of a mouse femur, settings: photon energy $E=10$ kEV, mean extracellular matrix mass density $\rho^{ec}=2.0$ g/cm³.

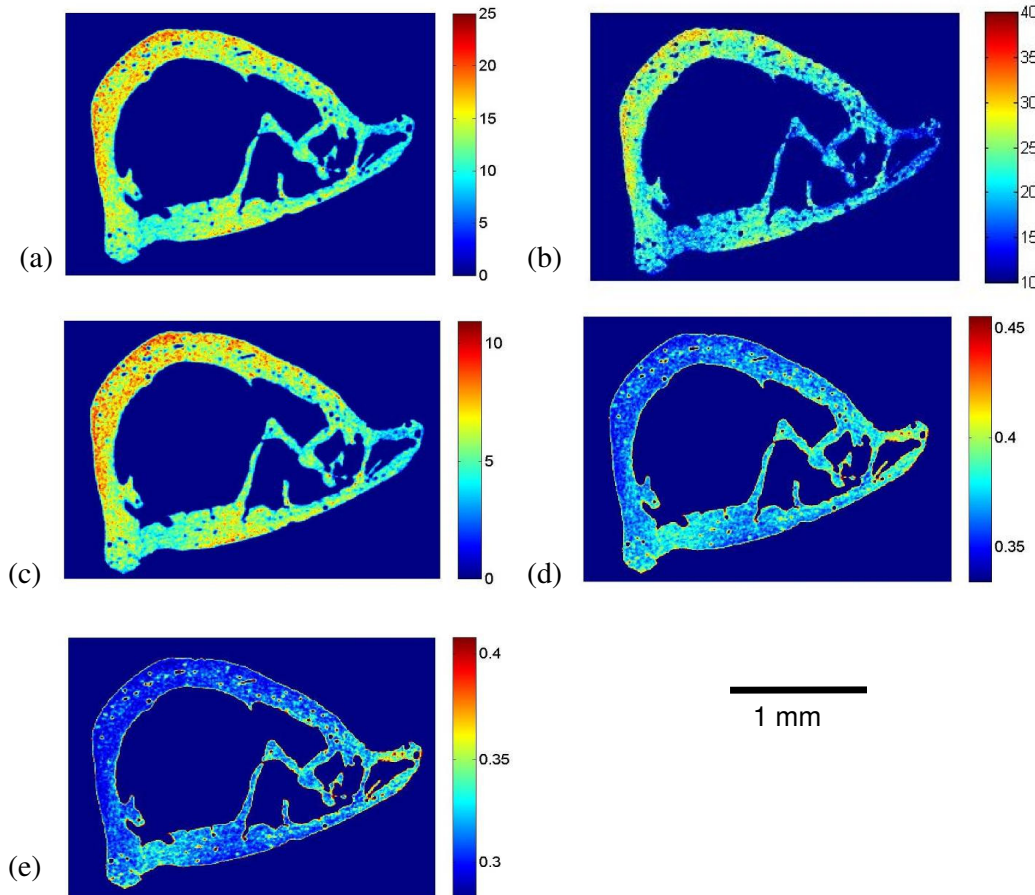


Figure 4: Distribution of voxel-specific transversely isotropic elasticity in the mouse femur, in terms of colour representation of engineering stiffness constants: (a) transverse Young's modulus E_{11} [GPa], (b) axial Young's modulus E_{33} [GPa], (c) axial shear modulus G_{23} [GPa], (d) Poisson's ratio ν_{12} in isotropic plane, and (e) axial Poisson's ratio ν_{13} ; settings: photon energy $E=10$ kEV, mean extracellular matrix mass density $\rho^{ec}=2.0$ g/cm³

Conclusion

We have presented a new concept for translating CT data into nanoporosity of ceramic scaffold materials and into the chemical composition of extracellular bone matrix, and for voxel-specific (multiscale) homogenization of elastic properties, based on the composition and microstructure of the materials. These mathematical relations are currently translated into a Graphical User Interface, as to demonstrate the functionality of the new concept and to allow for user-specific settings and refined data input and output. Finally, the software is currently made compatible with SKYSCAN's package "CT-Analyser" (CTAn)⁷.

Acknowledgments

This work was supported under the Theme FP7-2008-SME-1 of the 7th Framework Programme of the European Commission (Grant no. 232164, BIO-CT-EXPLOIT).

References:

1. V.S. Komlev, S.M. Barinov, E.V. Koplik, "A method to fabricate porous spherical hydroxyapatite granules intended for time-controlled drug release", *Biomaterials*, 23, 3449-3454, 2002
2. E.O. Crawley, W.D. Evans, G.M. Owen, "A theoretical analysis of the accuracy of single-energy CT bone measurements", *Physics in Medicine and Biology*, 33, 1113-1127, 1988
3. A. Zaoui, "Continuum micromechanics: survey", *Journal of Engineering Mechanics (ASCE)*, 128, 808-816, 2002
4. A. Fritsch, L. Dormieux, Ch. Hellmich, J. Sanahuja, "Mechanical behavior of hydroxyapatite biomaterials: An experimentally validated micromechanical model for elasticity and strength", *Journal of Biomedical Materials Research*, 88A, 149-161, 2009
5. A. Fritsch, Ch. Hellmich , L. Dormieux, "The role of disc-type crystal shape for micromechanical predictions of elasticity and strength of hydroxyapatite biomaterials", *Philosophical Transactions of the Royal Society A*, 368, 1913-1935, 2010
6. A. Fritsch, Ch. Hellmich, "Universal' microstructural patterns in cortical and trabecular, extracellular and extravascular bone materials: micromechanics-based prediction of anisotropic elasticity", *Journal of Theoretical Biology*, 244, 597-620, 2007
7. Skyscan: "CTAn User's Guide", Version 1.10, Skycan NV, Kontich, Belgium, 2010 (www.skyscan.be)

Tomographic reconstruction from limited data

K.J. Batenburg^{1,2}, Wim van Aarle², Elke Van de Castele²,
Willem Jan Palenstijn², Jan Sijbers²

¹ Centrum Wiskunde & Informatica, Science Park 123, NL-1098XG, Amsterdam, The Netherlands

² IBBT-Vision Lab, Universiteitsplein 1, B-2610, Wilrijk, Belgium

Introduction

At present, image reconstruction in micro-CT imaging is typically performed using the FDK algorithm. This algorithm, which is similar to the Filtered Backprojection algorithm for single-slice tomography, is capable of computing accurate reconstructions in a relatively short time, provided that the acquired dataset satisfies certain requirements:

- (i) a large number of projection images must be available;
- (ii) the angular step between consecutive projections must be approximately constant;
- (iii) the projections should not be too noisy;
- (iv) the object must be contained within the field-of-view (FOV) of the detector.

Violating these requirements typically results in degraded reconstructions, which can be difficult to interpret and analyze.

In many micro-CT applications it is actually desirable to deviate from these requirements. For in-vivo studies, for example, low dose CT is required to perform longitudinal studies. Another example is Region-Of-Interest (ROI) tomography, where only part of the object has to be reconstructed, and the object can be much larger than the FOV. Limiting the number of projection angles, the field-of-view, the signal-to-noise ratio, etc. results in *underdetermined* reconstruction problems. This means that the total set of measurements by itself is not sufficient to accurately reconstruct the scanned object. Such reconstruction problems are also known as *limited data problems*.

As a general strategy for obtaining accurate reconstructions from limited data, various forms of *prior knowledge* can be exploited within the reconstruction algorithm. For example, if it is known that the object consists of just a single material (e.g., a manufactured object consisting of a homogeneous polymer), the reconstructed image should be a black-and-white image, corresponding to the background (black) and polymer (white) respectively. Although such prior knowledge can be a powerful means to alleviate the problems associated with limited data reconstruction, modeling the available prior knowledge and exploiting it effectively is a nontrivial task.

Moreover, one needs to be careful to only specify what is known about the object, and not specifying properties that one expects to find. If the reconstruction algorithm is instructed that the object consists of a single material while in fact there are two materials, the results will be meaningless.

In the following section, four examples will be given of types of prior knowledge that can be successfully exploited to increase the reconstruction quality. From the first to the last example, the constraints imposed on the reconstruction become increasingly tight. When using a mild constraint, many projections are still needed to obtain accurate results. For the strongest types of constraints, a very small set of projection data is already sufficient.

Three types of prior knowledge

Nonnegativity

The reconstructions computed by the FDK algorithm are not restricted to positive values for the image voxels. As these values represent the attenuation coefficients of the materials in the scanned object, it makes sense to impose this physical property as prior knowledge in the reconstruction algorithm. While the FDK algorithm does not allow for incorporating this type of constraint, iterative methods such as the Simultaneous Algebraic Reconstruction Technique (SART) can enforce non-negativity [1]. Figure 1 illustrates the quality improvement that can be obtained.

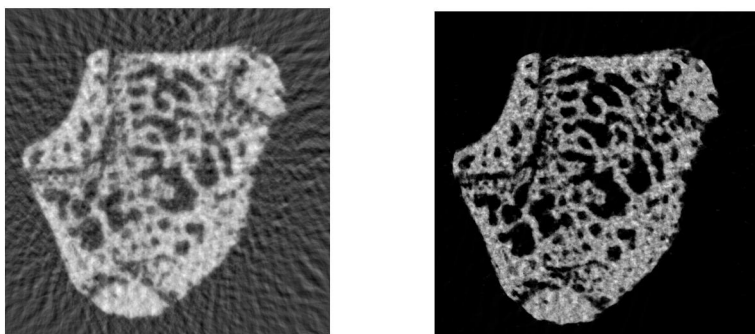


Figure 1: left: mouse femur slice, reconstructed using the iterative SART algorithm from 40 simulated projections without non-negativity constraint; right: the same slice reconstructed using the iterative SART algorithm with a non-negativity constraint

Discrete tomography

In certain applications, it is known in advance that the scanned object consists of only a few different materials, each corresponding to a distinct, constant grey level in the reconstruction. In such cases it makes sense that the reconstructed image only contains grey values from this small, discrete set of admissible values. This is the domain of *discrete tomography* [2]. Recently, powerful reconstruction algorithms, such as the Discrete Algebraic Reconstruction Technique (DART) have been developed that can incorporate such constraints [3]. Figure 2 illustrates that accurate reconstructions can be obtained even if very few projections are available.

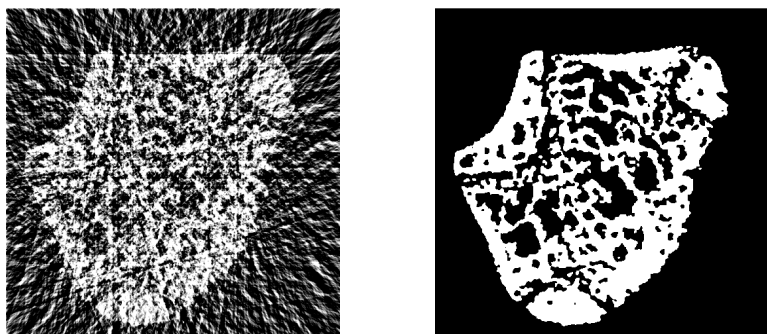


Figure 2: left: mouse femur slice, reconstructed using the Filtered Backprojection algorithm from 20 simulated projections; right: the same slice reconstructed using the DART algorithm for discrete tomography, assuming that there are only two grey levels (black and white).

Shape information

In some cases, it is not even possible to acquire a single complete projection image. If the object is considerably larger than the field-of-view of the X-ray detector, the projection images are all truncated. Hardly any reconstruction algorithms are available that can deal effectively with such truncated datasets, as the projections do not contain sufficient information about the object [4].

However, if powerful prior knowledge is available about the scanned object, a detailed reconstruction can still be obtained. It was recently proved mathematically, and demonstrated experimentally, that if the object is both homogeneous and *star-shaped*, it can be reconstructed even if it extends far beyond the FOV in all projection images [5].

Conclusion

Although limited data problems occur frequently in X-ray microtomography, one typically resorts to standard reconstruction algorithms that are not well-suited for this task. In recent years, reconstruction techniques have been developed that can exploit various forms of prior knowledge to obtain far more accurate reconstructions based on the same projection data. We illustrated the potential of these developments by several examples, where the amount of prior knowledge varies from elementary physical properties that are valid for all objects, to sample-specific shape information.

References:

3. A.C. Kak and M. Slaney, "Principles of Computerized Tomographic Imaging", SIAM, 2001.
4. G.T. Herman and A. Kuba, "Advances in Discrete Tomography and its Applications", Birkhäuser, 2007.
5. K.J. Batenburg and J. Sijbers, "DART: A practical algorithm for discrete tomography", IEEE Trans. Im. Proc., to appear, 2011.
6. R. Clackdoyle and M. Defrise, "Tomographic Reconstruction in the 21st Century: Region-of-interest reconstruction from incomplete data", IEEE Signal Proc. Mag., 27(4), 60-80, 2010.
7. G. Van Gompel, M. Defrise and K.J. Batenburg, "Reconstruction of a uniform star object from interior x-ray data: uniqueness, stability and algorithm", Inverse Problems, 25(6), 065010, 2009

Bone segmentation using discrete tomography

E. Van de Castele¹, K.J. Batenburg^{1,2}, P. Salmon³, and J. Sijbers¹

¹ IBBT-Vision Lab, University of Antwerp, Universiteitsplein 1, 2610 Wilrijk, Belgium,

² Centrum Wiskunde & Informatica, Science Park 123, 1098 XG Amsterdam, The Netherlands

³ SkyScan, Kartuizersweg 3B, 2550 Kontich, Belgium

Aims

Bone studies in X-ray micro-computed tomography (CT) are targeted towards analyzing a stack of virtual slices and calculating bone parameters in order to assess the differences in structures between, for example, control and diseased animals. Due to the small number of different materials under investigation, bone studies are ideal for discrete tomography, which is a new reconstruction technique. This method can be applied if the scanned object is known to consist of only a few materials; the prior knowledge on the grey values of each of these materials is then exploited to obtain a reconstruction that contains only these values. Reconstructing a stack of images with only a discrete set of grey values avoids the subjective segmentation step of global thresholding, mostly used in bone studies. A second advantage is that discrete tomography generally requires fewer projection images due to the use of prior knowledge. This is important when dose constraints determine the image quality, which is the case for in-vivo small animal studies.

The aim of this work is to present the first results on a real 3D dataset using the Discrete Algebraic Reconstruction Technique (DART). A comparison is made of the calculated trabecular morphometric parameters on the datasets obtained with the standard reconstruction and segmentation methods and with discrete tomography, both using 100%, 50% and 25% of the commonly used number of projection images.

Method

Sample material:

In this study, the sample under investigation is the distal femur of a control mouse. The soft tissue was removed from the bone as much as possible, after which the bone was stored in 70% alcohol. When scanning the sample, it was wrapped in saline-soaked gauze to avoid drying.

Micro-CT scanning:

The bone was scanned using a SkyScan 1172, a high resolution desktop X-ray micro-CT system. As a consequence of the cone beam geometry of the system, the distance of the sample to the source determines the magnification, which was set so that the bone stayed within the field of view of the detector for the full rotation cycle. By using camera binning, i.e. 4 by 4 pixels taken together giving 1000 pixels on a detector row instead of 4000, an isotropic pixel resolution of 4.98 μ m was obtained. In order to have an optimal contrast in the images, the source voltage was set at 40kV. Furthermore, a 0.5mm aluminium filter was used to restrict the X-ray spectrum to a more monochromatic range reducing the beam hardening effect. A frame averaging of 2 and a rotation step of 0.5°, covering a view of 180°, were chosen to minimize the noise. The scan took 13 minutes.

Reconstruction:

The most commonly used method for the reconstruction of X-ray cone beam data is the algorithm described by Feldkamp, David and Kress¹ (FDK). Although FDK is an approximate reconstruction method, the errors resulting from small cone angles are rather small and often acceptable. Additionally, FDK is computationally highly efficient and can thus offer very fast reconstruction speeds. For these reasons, FDK (often referred to as filtered back projection, FBP) is nowadays still the most used method.

Next to analytical reconstruction, there exist alternative approaches such as iterative reconstruction methods², which consider the reconstruction process as the optimization of a discrete representation of the object function in order to satisfy a system of equations that describes the imaging modality. If only a limited number of projections is available, if the sampling of the projections is not equiangular, or if certain orientations are missing, iterative methods can even provide reconstructions of higher quality than with FDK. Another advantage is their better noise handling. However, the main reason why they are not or only rarely used in X-ray µCT is the high computational burden. Currently these iterative techniques are accelerated using several GPU's³.

Within the field of Discrete Tomography, a new reconstruction algorithm, called the Discrete Algebraic Reconstruction Technique (DART) has recently been proposed with very promising results^{4,5}. DART is a reconstruction method based on iterative reconstruction techniques that includes prior knowledge on the grey values representing the materials under investigation. It directly reconstructs segmented images for further analysis. In other words the subjective step, used in e.g. bone studies, of selecting a threshold value can be avoided. This new reconstruction method has shown to achieve high quality reconstructions, even with a small number of projections. This is particularly interesting for small animal imaging using X-rays since the dose submitted to the animal imposes an important scanning constraint. In order to minimize the dose, researchers need to make a compromise in image quality due to the limitation on the scan time. With DART, fewer projection images can be used so that it would be possible within the same scan time to go to a higher frame averaging, thereby reducing the noise, or to choose a smaller pixel size obtaining a better resolution.

The following reconstructions were made:

Table I: Reconstructions and corresponding parameters

	Parameters	FDK	DART
NRecon parameters	Beam hardening correction	30%	30%
	Smoothing	1	1
	Ring artefact correction	5	5
Iterations	NA		Initial SIRT = 100 Update edges = 50 DART = 10
Number of projection images & corresponding rotation step	376 (0.5°), 188 (1°), 94 (2°)	376 (0.5°), 188 (1°), 94 (2°)	

The NRecon reconstruction parameters were applied on the sinograms exported from NRecon and used for the iterative reconstruction. The DART algorithm (flow chart shown in Figure 1) alternates iteratively between a "continuous" update step where SIRT was used and discretization steps incorporating the prior knowledge of the grey values of the image. This prior knowledge was obtained from an initial SIRT reconstruction.

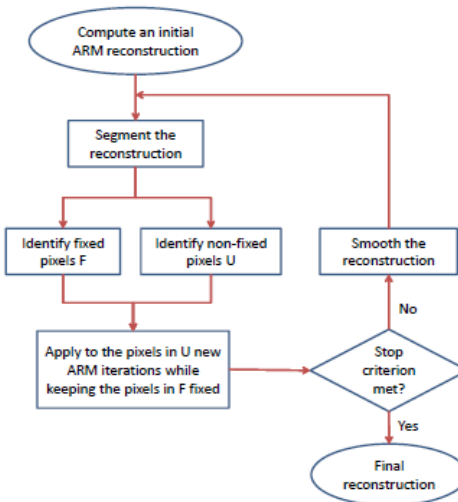


*Figure 1: Flow chart of the DART algorithm⁴.
Note that for the algebraic reconstruction method (ARM) SIRT was used.*

Parameter calculation:

For the quantitative analysis morphological parameters^{6,7} are calculated using CTAn. Several parameters are in common with histomorphometry: relative bone volume (BV/TV), trabecular thickness (Tb.Th), trabecular separation (Tb.Sp), trabecular number (Tb.N), and surface-to-volume ratio (BS/BV). Other parameters have been developed from micro-CT analysis of bone which are fundamentally 3D quantities and have no equivalent in 2D-based histomorphometry. These include for example the structure model index (SMI) which indicates the relative prevalence of plates and rods in trabecular bone and calculation of open and closed pores and number of objects in 3D.

Two steps are required for morphometric analysis of the reconstructed datasets:

(1) binarisation and (2) the selection of the volume of interest.

The most widely used method in bone research for binarisation is the simple and quick method of global thresholding. This technique is generally adequate for obtaining morphometric data where the bone images are of sufficient quality. However the selection of the grey value for thresholding is crucial since it is directly related to the thickness of the binarized structures. Often this threshold value is chosen using calibrated thickness measurements, which is done by scanning a micro-CT phantom composed of four aluminium foils of 20, 50, 100, 250µm embedded in a PMMA cylinder⁸.

The selection of the region of interest (ROI) is the starting point of the morphometric analysis. An important and common example is the selection of the volume of trabecular bone at a standard trabecular site in a rodent bone, such as the distal femur metaphysis as investigated in this paper. The ROI was selected containing trabecular bone and marrow only, starting 393µm above the growth plate and covering a region of 1.25mm in height (see *Figure 2 (a)* and *(b)*). The region of interest, on which the parameters were calculated, was kept the same throughout the different reconstructed datasets. 3D models were made for visualisation purposes using surface rendering (*Figure 2 (c)*).

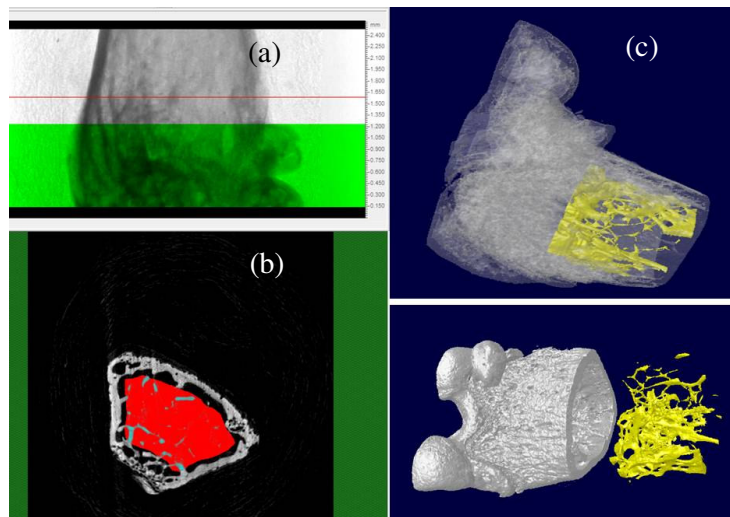


Figure 2. Selection of the ROI within the trabecular bone region and the corresponding 3D models: (a) Projection image: the non-highlighted area indicates the ROI in the Z-direction; (b) Transversal image showing the drawing of the ROI; (c) 3D surface rendering of the scanned mouse distal femur: full bone and selected trabecular region.

Results and discussion

In Table II, the calculated trabecular morphometric parameters of the mouse distal femur for the six different reconstructions are shown.

Table II: Trabecular morphometric parameters in the mouse distal femur

Number of projection images:	Standard FDK			DART		
	376	188	94	376	188	94
Parameter	Symbol (unit)					
Percent bone volume	BV/TV (%)	5.76	5.76	5.77	5.77	5.72
Bone surface	BS (mm ²)	9.79	10.00	10.78	9.38	9.31
Bone surface to volume ratio	BS/BV (mm ⁻¹)	77.25	78.90	84.93	73.83	73.94
Trabecular Thickness	Tb.Th (mm)	0.055	0.054	0.051	0.056	0.055
Trabecular Separation	Tb.Sp (mm)	0.37	0.37	0.34	0.38	0.38
Trabecular number	Tb.N (mm ⁻¹)	1.05	1.06	1.12	1.04	1.03
Structure model index	SMI	2.46	2.45	2.46	2.46	2.46
Number of objects	Obj.N	175	234	652	195	206
Number of closed pores	Po.N(cl)	4	30	131	3	4
						5

When comparing the results for FDK and DART using the full set of projection images, it can be seen that most parameters are similar. Differences are found in the bone surface, bone surface-to-volume ratio, and the number of objects. These differences can be visualized using 3D surface rendered models which are shown in Figure 3. The green DART model is shifted down over 5 pixels in comparison with the yellow FDK model in order to show the differences more clearly. The arrow in Figure 3 gives an example of the differences that are found at the thinner structures. These differences are due to the constraints used for obtaining the segmented images. With a global thresholding method, one threshold value

was chosen with the assumption that every material above this threshold is bone. In order to select smaller structures (having a lower grey value), the threshold value is lowered resulting in a thickening of the other structures. For discrete tomography however the prior knowledge on the grey values gives a much harder constraint. The selected value for bone gives a good segmentation for structures where no differences in grey values or partial volume effects are present. This explains the larger value for the number of objects and smaller BS and BS/BV for DART in comparison with FDK while the bone volume was the same.

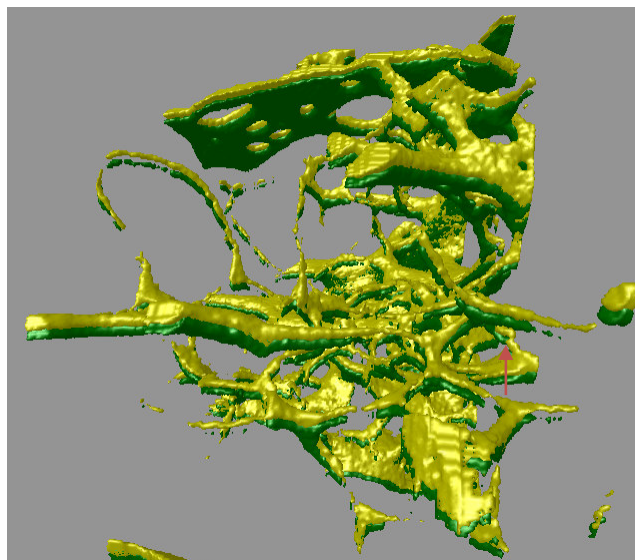


Figure 3: Comparison between the FDK reconstruction (yellow) and the DART result (green, shifted downward) both using 376 projection images for the reconstruction.

The results using fewer projections show that BV, BS and Tb.N decrease for DART, while the number of objects increases, indicating a further loss in connections on the smallest trabeculae. However, for the FDK reconstructions, more parameters are influenced and the differences are often larger, especially using only a quarter of the projection images. For the standard reconstruction technique the BS, BS/BV, Tb.N, Obj.N and the amount of closed pores increase, while the Tb.Th and Tb.Sp decreases. The latter only when using 25% of the images, indicating an increase in noise. Iterative reconstruction techniques are known for their advantage in handling in a better way noisy data or data obtained from fewer projections explaining the larger differences for FDK in comparison with DART. The increase in noise for FDK 94 can also be seen in *Table II* with the dramatic increase in number of objects and in closed pores.

Conclusion

Discrete tomography is a promising new method for bone research especially for in-vivo small animal imaging where dose constraints are important. This paper presents the first results on a 3D dataset and proofs the strength and robustness of DART using e.g. only a quarter of the projection images in comparison with the standard reconstruction method. In ongoing research the DART algorithm is further improved to make it more resilient to partial volume effects, which will potentially allow to resolve small structures with high accuracy.

References:

1. L.A. Feldkamp, L.C. Davis, and J.W. Kress, "Practical cone-beam algorithm", *J. Opt. Soc. Am. A* 1(6), pp. 612-619, 1984.
2. G.T. Herman, "Image reconstruction from projections: the fundamentals of computerized tomography", Academic Press, New York, 1980
3. J. Sijbers and K.J. Batenburg: Fastra II. <http://www.fastra2.ua.ac.be/>, 2009.
4. K.J. Batenburg and J. Sijbers, "DART: a fast heuristic algebraic reconstruction algorithm for discrete tomography", In: IEEE International Conference on Image Processing (ICIP), San Antonio, Texas, USA, 2007.
5. K.J. Batenburg and J. Sijbers, "DART: a practical reconstruction algorithm for discrete tomography", to appear in IEEE Transactions on Image Processing, Accepted, 2011.
6. A.M. Parfitt, M.K. Drezner, F.H. Glorieux, J.A. Kanis, H. Nalluque, P.J. Meunier, S.M. Ott, and R.R. Recker, "Bone Histomorphometry: standardization of nomenclature, symbols and units", *J. Bone Miner. Res.* 2(6), pp. 595-610, 1987.
7. A. Odgaard, "Three-dimensional methods for quantification of cancellous bone architecture", *Bone* 20(6), pp. 315-328, 1997.
8. E. Perilli, V. Le, B. Ma, P. Salmon, K. Reynolds and N.L. Fazzalari, " Detecting early bone changes using in vivo micro-CT in ovariectomized, zoledronic acid-treated, and sham-operated rats", *Osteoporosis International* 21, pp. 1371-1382, 2010.

Micro-computed tomography for imaging and quantification of non-mineralized tissues in rat mandibular condyle.

Z. Jabbour¹, C. Gao² J.E. Henderson², M. El-Hakim³, R. Albuquerque Junior¹

¹ Division of Restorative Dentistry, Faculty of Dentistry, McGill University, Montreal, QC, Canada

² JTN Wong Lab for Bone Tissue Engineering, Division of Orthopedic Surgery, Faculty of Medicine, McGill University, Montreal, QC, Canada.

³ Division of Oral and Maxillofacial Surgery, Faculty of Dentistry, McGill University, Montreal, QC, Canada.

Aims

Non-mineralized tissues are difficult of visualize and quantify. They could be normal anatomical structures such as blood vessels, or pathological lesions such as bone necrosis. Traditional techniques to examine non-mineralized tissues include histological analysis, which are limited to small areas of tissue and cannot provide adequate three-dimensional visualization and quantification (1-2). The aim of this study is to describe a simple method for visualization and quantification of non-mineralized tissues using micro-computed tomography (micro-CT).

Method

Rats used as controls for avascular necrosis associated with glucocorticoid administration in mandibular condyles were euthanized. Mandibular condyle articulates with the maxilla and skull by the temporomandibular joint below the zygomatic arch (Figure 1). Condyles were removed, cleaned of soft tissue, fixed overnight at 4°C in 4% paraformaldehyde, rinsed thoroughly in three changes of sterile phosphate buffered saline (PBS) and stored at 4°C while waiting for micro-CT scanning (Skyscan 1172, Kontich, Belgium with a 1.3MP camera) housed in the McGill Institute for Advanced Materials (MIAM). Acquisition of high resolution 2D images and reconstruction was performed using Control software for Skyscan 1172. Parameters for thresholding and analysis were selected using CTan software designed for quantification of bone microarchitecture. The region of interest (ROI) was drawn manually (Figure 2b). Thresholding for bone analysis was performed visually and selected at 70-255 range to mimic bone as closely as possible when compared to the raw image (Figure 2c, upper image). For non-mineralized tissues, the thresholding parameters were reversed (Figure 2c, lower image). Final adaptation of the ROI was achieved using the ROI shrink-wrap function (Figure 2d). Total and fraction of volume were calculated for bone and non-mineralized tissues.

Results

The results of the total and fraction of volume are tabulated below.

	Total volume (μm^3)	Volume fraction (%)
Bone tissues	3.963	92.973
Non-mineralized tissues	0.102	2.394

Conclusion

Visualization and quantification of non-mineralized tissues is possible using micro-CT.

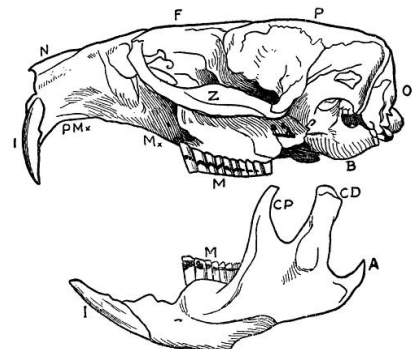


Figure 1: Rat skull showing: nasal (N), frontal (F), parietal (P), occipital (O), zygomatic arch (Z), audital bulla (B), Maxillary (upper jaw) (Mx), premaxillary (PMx), incisors (I), upper and lower molars (M), coronoid process (CP), mandibular condyle (CD) and mandibular angle (A).

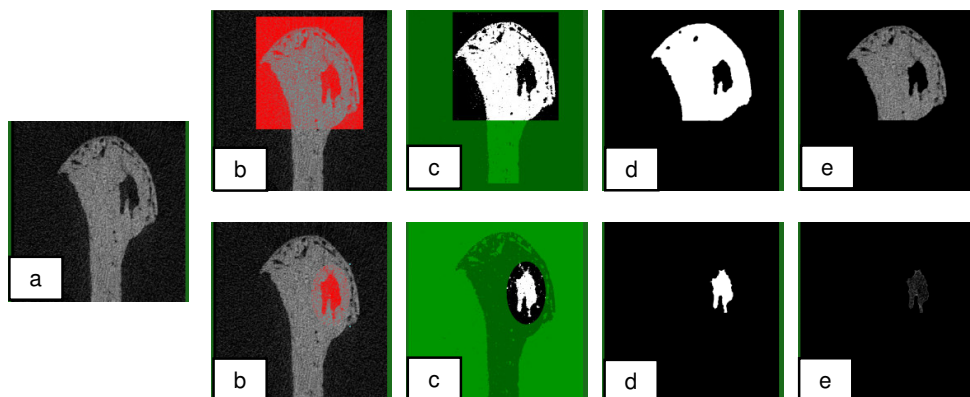


Figure 2: (a) raw cross sectional image of the mandibular condyle, (b) ROI drawn manually, (c) Thresholding for bone analysis (upper image) and reversed thresholding for non-mineralized tissues analysis (lower image), (d) Final ROI using shrink-wrap function, (e) image inside ROI.

References

1. Smolej, L. and P. Kasparova, "Choice of endothelial marker is crucial for assessment of bone marrow microvessel density in chronic lymphocytic leukemia", APMIS, 116(12): p.1058-62, 2008.
2. Barou, O., et al., "Relationships between trabecular bone remodeling and bone vascularization: a quantitative study", Bone, 30(4): p. 604-12, 2002.

Visualization of mouse and human femur based on SkyScan- μ CT

H. von der Kammer¹, J. Hostens², E. Bongaers², P. Young³, Ch. Hellmich⁴, C. Kober¹

¹ HAW Hamburg, Lohbruegger Kirchstr. 65, D-21033 Hamburg, Germany,

² Skyscan NV, Kontich, Belgium

³ Simpleware Ltd., Exeter, UK

⁴ Vienna University of Technology, Institute for Mechanics of Materials and Structures, Vienna, Austria

Aims

Due to its crucial role in locomotion, the trabecular architecture of femoral head and neck is a widely investigated subject in human and non human mammals^{1,2}. The purpose of this study is a refined analysis of the alignment of mouse and human trabecular structure by refined 3D-visualization methods based on μ CT-images.

Method

A preparation of a dry human femur placed at disposal by Simpleware Ltd., Exeter, UK, was scanned using a μ CT scanner (Skyscan 1173, Skyscan, Belgium) with a resolution of 54.04 μ m in all three spatial directions. A dried mouse femur was placed at disposal by Skyscan NV and scanned using a μ CT scanner (Skyscan 1172) with a resolution of 6.78 μ m in all three directions. All scanning was performed at Skyscan NV, Kontich, Belgium. Both image stacks were delivered as bmp- respectively as tiff-files with grey values ranging from 0-255.

For the sake of refined insight to the internal structure, the μ CT-data of both preparations were subjected to direct volume rendering with high transparency using a logarithmic physical color map (dark blue/low – light blue – green – yellow – orange – red/high). For image processing and visualization, we used the visualization toolbox Amira 5.2.2^{3,4}, Visage Imaging GmbH, Berlin, Germany.

Results

For the human femur, the typical trabecular arrangement often discussed in standard orthopedic literature⁵ can be observed (Fig. 1, 2).

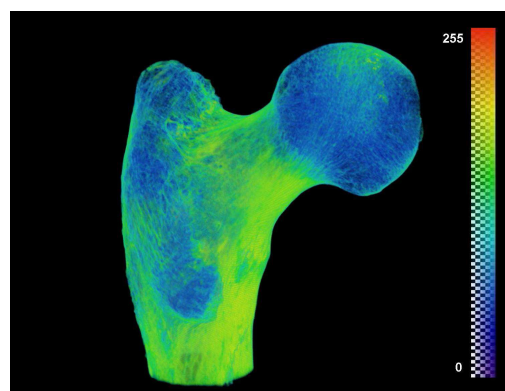


Figure 1: Visualization based on the human femur preparation as a whole with the colors referring to the gray values of the μ CT-data

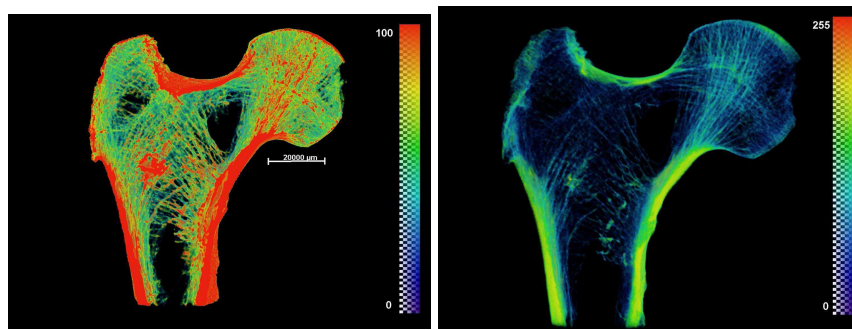


Figure 2: Trabecular structure of the human femur using different color scales

A highly transparent visualization of the mouse femur as a whole is given in Figure 3, whereas, in Figure 4, some details of trabecular structure are displayed. According to different loading regimes of mouse and human locomotion, trabecular architecture is highly different.

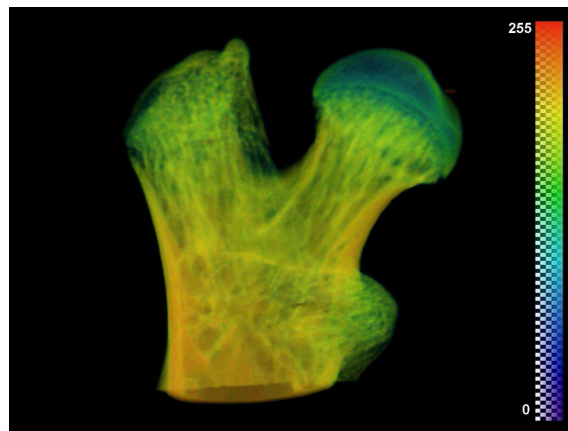


Figure 3: Visualization of the mouse femur preparation as a whole

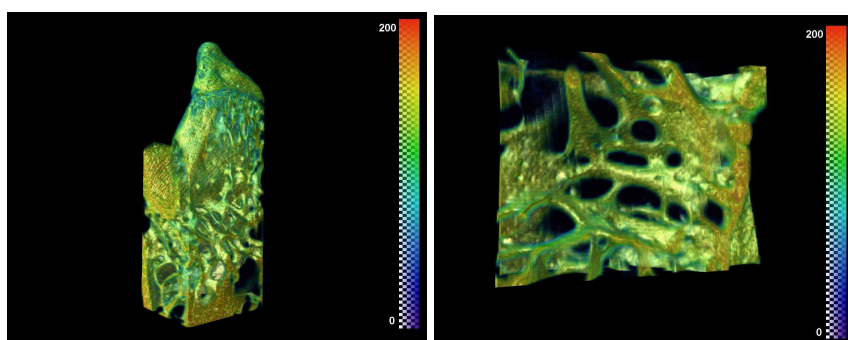


Figure 4: Details of the trabecular structure of the mouse femur

Conclusion

3D-visualization based on μ CT images enables detailed analysis of trabecular architecture of femoral head and neck of different mammalian bones.

Acknowledgments

This work was partially supported under the Theme FP7-2008-SME-1 of the 7th Framework Programme of the European Commission (Grant no. 232164, BIO-CT-EXPLOIT).

References:

1. R. J. Fajardo, R. Müller, R. A. Ketcham, M. Colbert, "Nonhuman Anthropoid Primate Femoral Neck Trabecular Architecture and Its Relationship to Locomotor Mode", *Anat Rec*, 290, 422–436, 2007
2. T. M. Ryan, A. Walker, "Trabecular bone structure in the humeral and femoral heads of anthropoid primates", *Anat Rec*, 293(4), 719-729, 2010
3. Visage Imaging GmbH. Amira™ – Visualize Analyze Present, <http://www.amira.com/>, accessed January 10, 2011
4. Stalling D, Westerhoff M, Hege HC. Amira: A highly interactive system for visual data analysis. In: Charles D. Hansen, Christopher R. Johnson (eds). *The Visualization Handbook*, Vol. 38, Elsevier, 749-767, 2005
5. H.-P. Scharf, A. Rüter, T. Pohlemann, I. Marzi, D. Kohn, K.-P. Günther, "Orthopädie und Unfallchirurgie: Facharztwissen nach der neuen Weiterbildungsordnung", Elsevier, Urban & Fischer Verlag, 2008

Creation of Computational Model of Cancellous bone

P. Marcián¹, J. Valášek¹, D. Krpalek¹, L. Borák¹, O. Konečný², M. Vašek¹, Z. Florian¹

¹ Institute of Solid Mechanics, Mechatronics and Biomechanics, Faculty of Mechanical Engineering Brno University of Technology, Technická 2896/2, Brno,

² Department of Control and Instrumentation, Faculty of Electrical Engineering and Communications, FEEC BUT, Kolejní 4

Aims

The paper deals with a creation of computational model of cancellous bone. Cancellous bone is inner porous part of bones and it is of a very complex geometry. It is composed of special trabecular architecture and the trabeculae can be less than 1 mm in diameter. In most cases, cancellous bone is modeled as a "non-trabecular" solid body with an apparent Young's modulus. A creation of a "trabecular" model of cancellous bone (which, in our opinion, is more appropriate) is quite difficult. MicroCT images are necessary for this case as well as the software for their processing. However, other way how to obtain information about bone architecture is to mill thin layers out of the bone specimen embedded into dyed epoxy resin. Authors of this paper developed for this purpose specialized software called STL Model Creator¹ which works in Matlab platform. The software uses image processing methods in segmentation of cancellous bone images. The paper introduces a method of creating of computational model and initial stress-strain analysis utilizing this model is presented as well.

Method

Firstly, bone specimen was placed in 30% peroxide solution in order to remove any remaining impurities. Secondly, the specimen was embedded into hard epoxy resin which was combined with fine black dry powder from printer toner cartridges. The embedded bone specimen was then placed into vacuum pump and the air was pumped out. The resulting vacuum ensured penetration of epoxy into holes among trabeculae. Afterwards, thin layers (0.02 mm) were removed in sequence by using fine milling and images of each layer were taken. Prior to taking images by camera fixed on the milling machine and equipped with yellow filter the specimen was floodlighted by UV-light. From the obtained images polygonized mesh was created by using STL Model Creator software and the final mesh was saved in STL-file format. Subsequent analyzing of mechanical response of cancellous bone tissue to external loading can be performed by means of computational modeling, specifically by using numerical methods. The most popular numerical method – finite element method (FEM) – was used; specifically, commercial product based on this method - ANSYS 11.0 (Ansys Inc., Canonsburg, PA, USA). In general, computational model consists of four submodels: model of geometry, model of material, model of loads and model of boundary conditions.

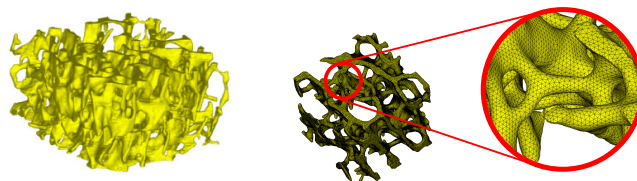


Figure 1: Geometry model and FE model of cancellous bone

At micro-level, cancellous bone is of the same mechanical properties as cortical bone². The material used in the computational model is homogenous, isotropic and linearly elastic – which is defined by two independent characteristics: Young's modulus $E = 13\,700$ MPa and Poisson's number $\mu = 0.3^3$.

The specimen was loaded in Z-axis by means of pre-defined displacements of all nodes at one side of the specimen in XY-plane.

Results

Using FEM one can identify risky locations of stresses and strains. Fig. 2 and 3 show typical first and third principal stress and strain distributions. These results indicate locations with the most severe tensile and compressive loading within individual trabeculae. In future, by using this methodology it will be possible to perform studies and analyses of mechanical interaction of bone with applied dental implants, bone substitutes etc. at higher modeling-level comprising detailed trabecular architecture.

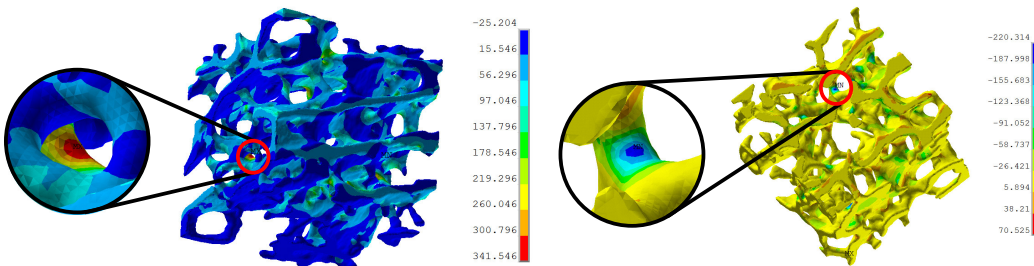


Figure 2: 1st and 3rd principal stresses [MPa] (0.5% elongation)

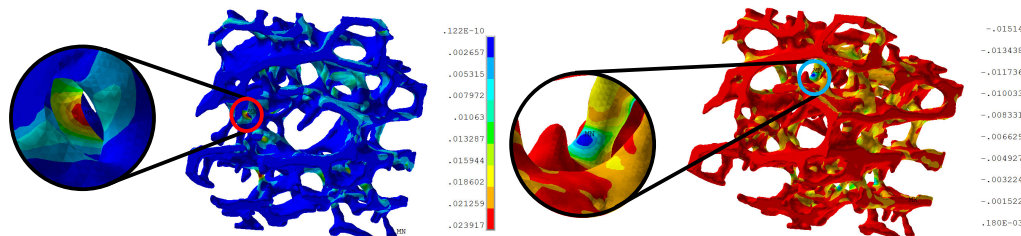


Figure 3: 1st and 3rd principal stresses [MPa] (0.5% elongation)

Conclusion

The aim of this paper was to create a computational model of cancellous bone specimen reflecting the trabecular architecture. STL Model Creator software developed by the authors was used for the reconstruction of images obtained from sequential milling thin layers of the specimen. The computational model created this way belongs to models at the highest modeling-level used up-to-date.

References:

1. Konečný, O., Marcián, P. et al. (2010), software, STL Model Creator, biomechanika.fme.vutbr.cz
2. Rho, J. Y., Tsui, T.Y., Pharr, G. M. (1998) Elastic properties of osteon and trabecular bone measured by nano-indentation, Journal of Biomechanics, vol.31, pp 21.
3. Bratu, E., Steigmann, M. (2003) Analyse der strukturellen Spannungen zwischen Implantat und Knochen. Implantologie J, vol. 7, pp. 47–49.

Computer aided customized creation of scaffolds

Peter Verschueren¹, Pieter-Jan Corthouts¹

¹ Materialise NV, Technologielaan 15, 3001 Heverlee, Belgium.

Aims

The design of scaffolds and search for the optimal pore shape and size is a topic of ongoing research within the tissue engineering community. In a 2009 review paper Hollister¹ finds i) the need for a more complete understanding of scaffold material and design requirements and ii) the need to better integrate computational design techniques with manufacturing methods as two of the six main reasons why the penetration of new scaffolding materials and structures from research laboratories to the clinic has been extremely limited.

Method

This paper presents a method to obtain fully customized 3D computer scaffold designs starting from patient specific scan data. The resulting scaffolds are ready to be produced via rapid manufacturing techniques. This method is then illustrated on a mouse bone scaffold coming from micro-CT scan data acquired by the SkyScan 1076 system using Mimics Innovation Suite software as shown in figure 1. From the virtual design a 3D printed scaffold is created in polycaprolactone using a fused deposition modelling technique.

Results

From patient specific data a high quality 3D triangle mesh model is calculated. From this model the anatomy to be replaced by a scaffold is selected and virtually separated. A porous unit cell which can be designed by the user, also represented by a triangle mesh, is patterned into a geometry which envelopes the separated anatomy from above. A virtual cutting operation on triangle mesh level between the separated anatomy and the patterned grid results in a customized scaffold structure.

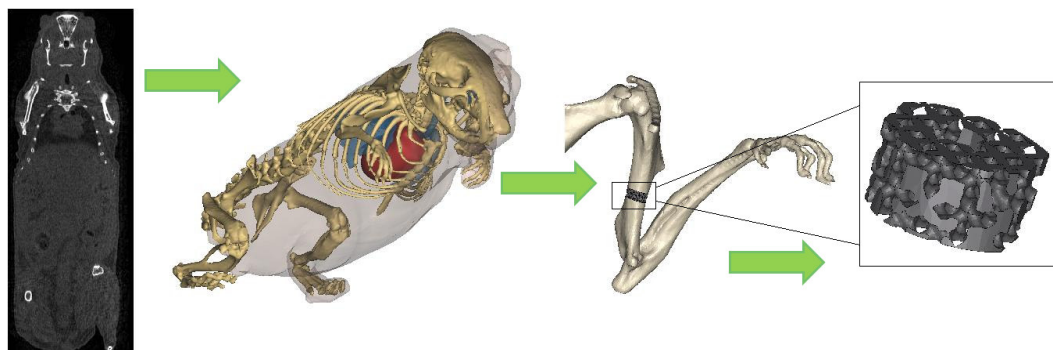


Figure 1: Workflow summary to obtain a customized bone scaffold starting from a micro-CT from a mouse.

Conclusion

The ability to create customized scaffolds with an unlimited freedom in unit cell structure can increase the speed of research and understanding of the influence of scaffold pore size and shape on cell differentiation and cell growth rate.

References:

1. Hollister S.J. Scaffold Design and Manufacturing: From Concept to Clinic. *Advanced Materials* 21 (32-33), 3330-42, 2009

Effect of Variability in Image Segmentation on Quantitative Parameters from Micro-CT Analysis of Human Cancellous Bone

I.H Parkinson^{1,2}, A Badiei^{1,2}, N.L Fazzalari^{1,2}

1. Bone and Joint Research Laboratory, SA Pathology and Hanson Institute.
2. Discipline of Pathology, University of Adelaide. Adelaide, South Australia.

Aims: A critical step in the quantitative analysis of micro-CT datasets is the assignment of each pixel in the 2D tomographs to the bone phase or the marrow phase. The segmentation process can be performed by a variety of methods ranging from subjective global methods to objective algorithm-based methods. The purpose of this study was to quantify the variability in image segmentation obtained by multiple users and segmentation methods and to determine the effect of this variability on quantitative parameters in human cancellous bone.

Methods: Three cubes of bone (10x10x10 mm) were cut from each of four vertebral bodies of a 33 year old human cadaver. Micro-CT scanning was performed on a Skyscan 1072 micro-CT scanner at an orthotropic resolution of 15µm/pixel (Figure 1). The scanner settings were, voltage=80kV, current=120µA, frame averaging = 4, rotation = 0.9° and 1mm aluminium filter. Global thresholding was performed by three operators and the objective thresholding algorithm of Otsu was applied. BV/TV and Tb.Th* (sphere-fitting algorithm) were obtained from all segmented datasets using CTAn software (Skyscan Ltd). Finally, the ash weight of specimens was obtained, yielding the ‘true’ apparent volumetric bone density. Variability in grey-level threshold, BV/TV and Tb.Th* between all methods and operators was expressed as bias and random error.

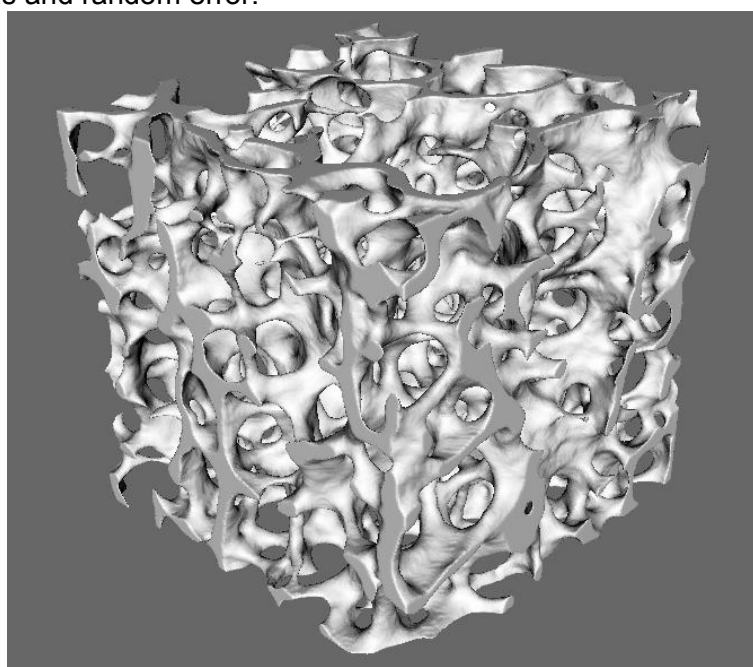


Figure 1: 3D reconstruction of a bone cube from the centre of a human vertebral body.

Results: The variability between operators and methods, in the selection of the grey-level threshold, showed bias ranging from 0.09% to 6.9% (Table 1) and random error ranging from 1.5% to 3.2% (Table 2). For BV/TV, bias ranged from 1.6% to 20.9% and random error

ranged from 4.8% to 10.6%. For Tb.Th*, bias ranged from 1.4% to 12.2% and random error ranged from 2.9% to 5.8%. These errors translate to differences of up to 8% in BV/TV estimates and 30 μ m in Tb.Th*.

Table 1: Bias (%) between and within operators (OP1, OP2 and OP3) and Otsu's method for all parameters.

	Grey	BV/TV	Tb.Th	Tb.Sp	Tb.N	TBPf	SMI	DA
OP1 v OP1 ₂	0.8	2.7	1.3	6.5	1.3	9.6	10.8	0.2
OP1 v OP2	3.2	10.1	5.4	20.1	4.5	34.5	41.9	0.2
OP1 v OP3	3.9	12.0	7.7	8.8	4.4	16.6	22.1	1.4
OP2 v OP3	7.1	22.0	13.1	29.2	8.9	49.8	61.6	1.5
OP1 v Otsu	0.1	2.0	1.4	3.7	0.7	6.4	9.6	0.2
OP2 v Otsu	3.1	12.1	6.8	24.1	5.2	40.4	50.4	0.4
OP3 v Otsu	4.1	10.0	6.3	5.2	3.8	10.2	12.6	1.1

Table 2: Random error (%) between and within operators (OP1, OP2 and OP3) and Otsu's method for all parameters.

	Grey	BV/TV	Tb.Th	Tb.Sp	Tb.N	TBPf	SMI	DA	Co ncl usi on: Thi s stu dy
OP1 v OP1 ₂	2.6	8.0	4.6	17.8	3.5	34.7	42.3	1.0	
OP1 v OP2	2.4	8.4	4.3	16.1	4.1	28.1	33.6	1.2	
OP1 v OP3	1.7	5.1	3.9	5.4	2.3	16.9	17.9	0.9	
OP2 v OP3	3.3	11.3	6.4	18.2	6.1	32.6	37.1	1.7	
OP1 v Otsu	1.9	4.8	2.8	5.9	2.1	11.1	15.5	0.8	
OP2 v Otsu	2.8	7.7	4.2	18.0	3.6	31.7	38.3	1.4	
OP3 v Otsu	2.4	6.9	4.3	2.5	3.7	14.3	10.5	1.1	

was not designed to determine the best method of image segmentation for micro-CT datasets but to highlight the dangers of non-standardisation of methodology. In particular, the variability between operators in setting a global threshold is statistically small (less than 7%) but translates into biologically significant differences in quantitative parameters (up to 8% in BV/TV estimates and 30 μ m in Tb.Th*). It is recommended that when global thresholding is used, a single operator for the entire study is essential. In addition, greater effort needs to be given to establishing objective segmentation methods, which are validated against a 'gold standard' such as ash weight.

Iterative reconstruction for segmentation of trabecular bone from in vivo microCT

M. Depypere¹, J. Nuyts², K. Laperre³, G. Carmeliet³, F. Maes¹, P. Suetens¹

¹ Medical Image Computing (ESAT/PSI), maarten.depypere@uz.kuleuven.be

² Department of Nuclear Medicine

³ Laboratory for experimental medicine and endocrinology
Katholieke Universiteit Leuven, Belgium

Aims. MicroCT allows the in vivo imaging of small animal bone structures. To detect subtle alterations in bone structures over time or between different mouse models, a sensitive segmentation method is required. The segmentation becomes problematic when image resolution decreases, as is the case for in vivo imaging. Murine trabecular bone can have dimensions similar to the system resolution, leading to blurred and less intense trabeculae in the reconstruction. To correctly segment even the thin bone structures, we attempt to incorporate the blurring of the projection data due to the microCT scanner, which is characterised by the point spread function (PSF) of the scanner.

The filtered backprojection reconstruction method does not allow incorporation of the PSF. Instead, the blurred projections can be corrected for the PSF prior to reconstructing using deconvolution techniques. Unfortunately these techniques are very sensitive to noise, and in vivo scans are rather noisy due to dose constraints. As incorporation of the PSF is unsatisfactory using filtered backprojection, we investigate whether an iterative reconstruction technique is more robust and whether it is feasible to use in everyday scanning.

Method. Iterative reconstruction techniques generally start from a uniform image that serves as estimate of the reconstruction, and iteratively refine this estimation. In each iteration the projections of the current reconstruction estimate are calculated and compared to the measured projections obtained during the microCT scan. The difference between current estimate projections and the measured projections is backprojected and added to the reconstruction estimate. This procedure is iterated until convergence, i.e. until the current calculated projections are equal to the measured projections.

As any real world measurement contains noise, the two sets of projections will never match exactly and the method will keep cycling. To resolve this issue, iterative reconstruction techniques can be formulated in a statistical framework, resulting in a search for the most likely reconstruction given the projection data [1]. Even in the presence of noise a most likely image will be found. The statistical model also allows incorporation of prior information about the object to be reconstructed. In our bone application, we know that the image consists of a limited number of tissues: usually bone, soft tissue and air. When for a certain voxel the projection data is indecisive for an attenuation value, the prior information can nudge the voxel towards an attenuation value that is close to that of one of the expected tissues. The prior can be implemented by modelling every tissue as a Gaussian, requiring knowledge about the number of tissues and their expected attenuation values. Instead, we use a variation on the joint entropy prior that needs no image specific input, but yields a clustered histogram as well [2].

A projection and a backprojection need to be performed in each iteration of the iterative reconstruction, making it a computationally expensive technique. In return more flexibility in defining the projector is obtained. If the calculated projections are smoothed with a kernel

similar to the PSF of the scanner, the effect of the PSF is incorporated and the reconstruction estimate is expected to be sharper.

Experiment. The tibiae of four male Bl6 mice were scanned *in vivo* using the SkyScan1076 microCT scanner at a pixel size of 9 micron. The mice were immediately sacrificed and the excised tibiae were scanned *ex vivo* in the SkyScan1172 microCT scanner with a pixel size of 5 micron. Both *in vivo* and *ex vivo* projection data sets were reconstructed using the filtered backprojection method available in NRecon (version 1.5.1.4; SkyScan). Additionally, the *in vivo* projection data was reconstructed using the presented iterative approach. The reconstructed region was restricted to the central slice of the object to make the iterative reconstruction feasible with respect to its computational burden.

All reconstructions were segmented using a global threshold. As it is well known that the global threshold is incapable of correctly segmenting thin objects relative to the resolution, the filtered backprojection reconstruction of the *in vivo* data was also segmented using the adaptive thresholding in CTAn (version 1.9.1.0; SkyScan). The three reconstructions of each tibia were registered to each other and this relationship was used to transfer a delineated region of interest (ROI) to the two other reconstructions. To evaluate the performance of the *in vivo* reconstruction and segmentation techniques, 2D bone parameters were calculated from the ROIs using CTAn for every approach and the results were compared. The high resolution *ex vivo* segmentation is considered as golden standard. Comparisons were based on the percentage error from the golden standard, which is 100 times the actual difference between the measurement and the golden standard, divided by the golden standard.

Results. As can be seen in table 1, the conventional reconstruction method with a simple global threshold leads to errors of 30% or larger for both bone volume fraction (BV/TV) and trabecular thickness (Tr.Th). Replacing the threshold by a more advanced technique that takes the local background into account improves these errors to 10%. The presented iterative reconstruction approach further reduces the trabecular thickness error by half. The different segmentations do not have a large effect on the trabecular number (Tr.N). These results are confirmed by visual inspection of the reconstructions and their segmentations in figure 1.

An important issue is the computation time. Calculating the iterative reconstruction of one slice of a 1000x1000 pixel image currently takes approximately one hour. The same slice takes only a few seconds to be reconstructed by filtered backprojection.

Reconstruction	Threshold	BV/TV (%)	Tr.Th (%)	Tr.N (%)
Filtered backprojection	Global	29.96	35.06	8.87
Filtered backprojection	Adaptive	10.03	11.32	12.48
Iterative Reconstruction	Global	10.86	5.26	11.10

Table 4. Mean percentage error from the golden standard over all animals for the different reconstruction and thresholding methods of *in vivo* data.

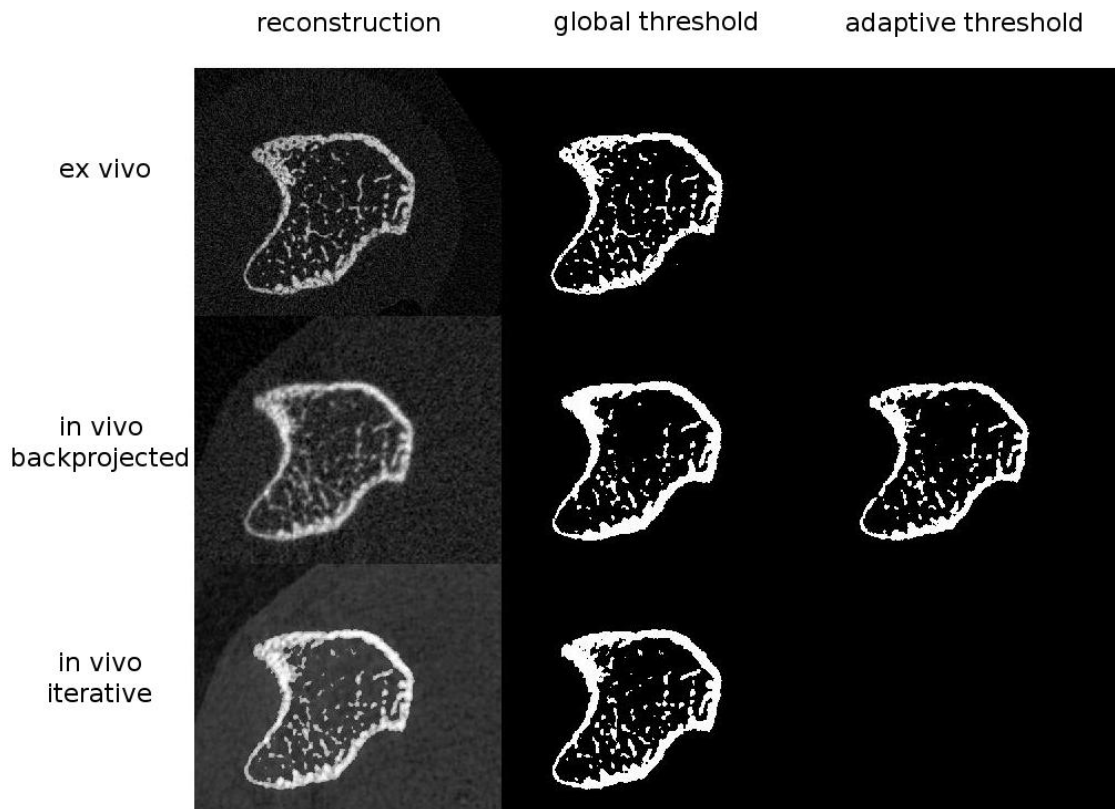


Figure 1: Results of the different reconstruction and segmentation approaches on the datasets of one animal.

Conclusion. We have presented an iterative reconstruction technique for in vivo microCT data that improves estimates of trabecular thickness compared to filtered backprojection reconstructions. The strength of the approach is that incorporates the PSF of the scanner. The major drawback of the method is the computational complexity. Executing image manipulation tasks that can be parallelised on a graphics processing unit (GPU), results in speed gains of a factor 10 up to 100 times compared to running the task on a central processing unit (CPU). To achieve the speedup required to make the iterative approach feasible in everyday scanning, the method could be implemented on the GPU.

References.

- [1] K. Lange and R. Carson, "EM reconstruction algorithms for emission and transmission tomography," *Journal of Computer Assisted Tomography*, vol 8, pp 306, 1984
- [2] J. Nuyts, "The use of mutual information and joint entropy for anatomical priors in emission tomography," *Nuclear Science Symposium Conference Record*, vol 6, pp 4149, 2007

In-vitro Evaluation of the Sinus Sagittalis Superior Thrombosis Model in the Rat using 3-D Micro- and Nano-Computed Tomography

Anne Ostendorf^{1,*}, M.D Mesut Yeniguen^{2,*}, M.D.;; Simone Marhoffer², DVM, Christian Dierkes⁴, M.D.; Susanne von Gerlach⁴, M.D.; Marian Kampschulte¹, M.D.; Georg Bachmann³, M.D.; Erwin Stolz², M.D., Tibo Gerriets², M.D.; Alexander C. Langheinrich^{1,*}, M.D.;

1) Department of Radiology, Justus-Liebig University Giessen, Germany

2) Department of Neurology, Experimental Neurology Research Group, Justus-Liebig University Giessen

3) Department of Radiology, Kerckhoff Clinic Bad Nauheim, Germany

4) Department of Pathology, Justus-Liebig University Giessen, Germany

Aims:

Clinical diagnosis of cerebral venous thrombosis (CVT) can be difficult due to the wide spectrum of symptoms and the large variation in the time interval from symptom onset to hospital admission¹. To elucidate the pathophysiology of CVT and to evaluate new, experimental therapies animal models are indispensable because they provide standardized conditions. Thrombosis of the superior sagittal sinus (SSS) has been developed in several animal models inducing irreversible sinus occlusion, leading to increase intracranial pressure and bloodbrain barrier disruption resulting in progressive cerebral edema, hemorrhagic infarcts, and occasionally to subarachnoid hemorrhage.

Hence, the purpose of our study was to evaluate micro-CT's technical feasibility to quantify structural and functional vascular alterations in the well-established sinus sagittalis superior thrombosis model in rats.

Methods:

Animal Preparation:

Four Male Sprague-Dawley rats were anesthetized with 5% isoflurane delivered in air for 2 minutes. Anesthesia was maintained with 2% to 3% isoflurane delivered in air at 0.5 L/min during surgery. Body temperature was continuously monitored with a rectal probe and maintained at 36.5°C to 37.0°C. The right external carotid artery (ECA) was ligated and transsected to create an ECA stump with a length of ~5 mm. Superior Sagittal Sinus Thrombosis Model:

The SSS thrombosis was induced experimentally as described previously². The head was fixed in a stereotactic frame in prone position. Skull was exposed by a 1.5 cm midline skin incision at the dorsal aspect of head and alongitudinal cranial window (10 mm × 1.5 mm) was made between the lambda and bregma sutures to expose SSS. Thrombosis of SSS was induced by topical application of a small strip of filter paper soaked with 40% ferric chloride for 5 min in dark. After 5 min, strip of ferric chloride was removed and the field was flushed with 0.9% saline. The removed bone strip was replaced, sealed with bone cement and skin was sutured.

Post mortem preparation:

The animals were anesthetized and after thoracotomy, PE-50 tubing was inserted into the left ventricle, followed by incision of the right atrium. Then the animal's circulation was flushed with heparinized saline and 5ml Microfil® (Flow Tech, Inc., Carver, Massachusetts, USA) was prepared and injected through the aortic arch to fill the arterial and venous cerebral circulation via the internal carotid and the vertebral arteries. After 45 minutes,

Microfil formed an elastomeric gel at room temperature. Then the brains including the intact dura mater were removed from the skull and immersed in 4.5% formalin. Contrast perfusion was performed 4 hours after infarction.

Micro-Computed Tomography:

All samples were scanned in a micro-computed tomograph (micro-CT) manufactured and developed by SkyScan (SkyScan1072_80kV; Belgium). The X-ray system is based on a microfocus tube (20-80 kVp, 0-100 μ A) reaching a minimum spot size of 8 μ m at 8W generating projection images irradiating X-rays in cone-beam geometry. This system has been described in detail before^{3,4}. The resulting 3D images were displayed using image analysis software (Analyze® 8.0; Biomedical Imaging Resource, Mayo Clinic, Rochester, MN). For this study, our micro-CT scanner was configured so that the side dimension of the cubic voxels was 8 to 12 μ m.

Nano-Computed Tomography:

For more detailed analysis of the brain microvessels, samples were rescanned at 900 nm isotropic voxel size using a nanocomputed tomograph (Nano-CT_2011), manufactured and developed by SkyScan® (Kontich, Belgium). The microfocus X-ray source is a pumped type source (open type x-ray source) with a LaB6 cathode. The electron beam is focused by two electromagnetic lenses onto the surface of an x-ray target. The x-ray target (Au) contains a thin tungsten film plated on the surface of the beryllium window producing x-ray emission reaching a minimum spot size of <400nm. At this small spot size, small-angle scattering enhances object details down to 150 nm isotropic voxel size. The X-ray detector consists of a 12-bit digital, water-cooled CCD highresolution (1280 x1024 pixel) camera with fibre optic 3.7:1 coupling to an X-ray scintillator and digital frame-grabber. In our experimental setting samples were positioned on a computer controlled rotation stage and scanned 180° around the vertical axis in rotation steps of 0.5 degrees at 40 kV. Acquisition time for each view was 2.4 seconds. Relative position of the object to the source determines geometric magnification and thus the pixel size defined by the cone-beam geometry of the system. Maximum possible magnification is also limited by the specimen size, which has to be within the cone-beam in its horizontal diameter. Raw data were reconstructed with a modified Feldkamp cone-beam reconstruction modus resulting in two dimensional 8-bit gray-scale images consisting of isotropic cubic voxels. Gray scale attenuations of nano-CT images were obtained in the parasagittal cortex, the occluded sinus sagittalis superior (thrombus) and compared to controls. For determination of relative attenuation values, rectangular regions of interest (ROI; side length, 0.5 mm at 8 bit) were established manually in areas by non-visible assessment of gray-scale differences. Gray scale attenuations were measured in 40 different areas within each brain using the ANALYZE© software package.

Histology:

The entire tissue block was embedded in paraffin and cut into cross-sections of 6 μ m with a microtome. The sections were mounted on a microscope slide and stained with hematoxylin/eosin. Cross-sections were digitized, analysed and compared to micro/nano-CT images.

Results:

Micro-CT proved to accurately visualize and differentiate vascular occlusion territories performed in the SSS thrombosis model of cerebral ischemia in rats. Moreover, 3D micro-CT provided quantitative information on arterial and venous vascular volume fraction. Micro-CT imaging enables a total 3D visualization of complications (ventricle rupture) in the SSS thrombosis model. We established gray scale measurements by which focal cerebral ischemia could be radiographically categorized ($p < 0.001$). Using nano-CT, the interface of contrast-perfused and occluded veins can be visualized.

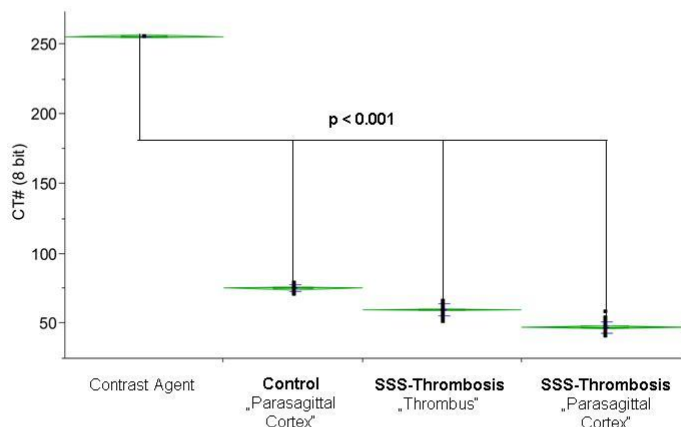


Figure 1: Gray scale value differences obtained in animals with SSS thrombosis compared to controls. Lower CT # (gray scale values) obtained in the parasagittal sinus in the SSS thrombosis group indicating progressive edema ($p < 0.001$) compared to controls. The thrombus formation demonstrates significant lower gray scale values as the parasagittal cortex and significant higher values compared to the parasagittal cortex in the SSS thrombosis group ($p < 0.001$).

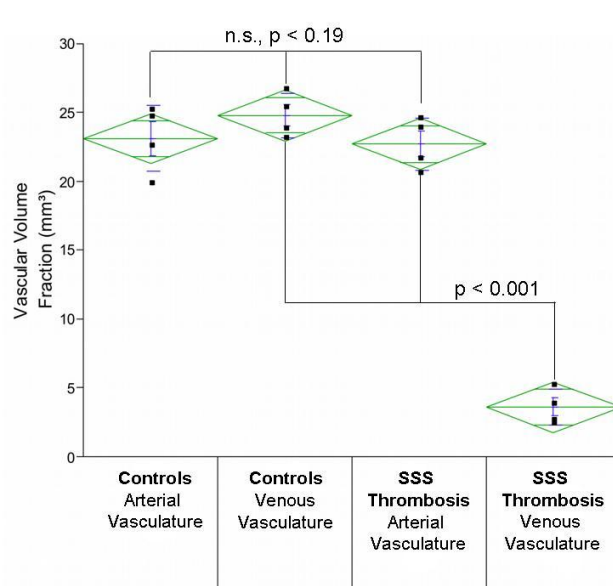
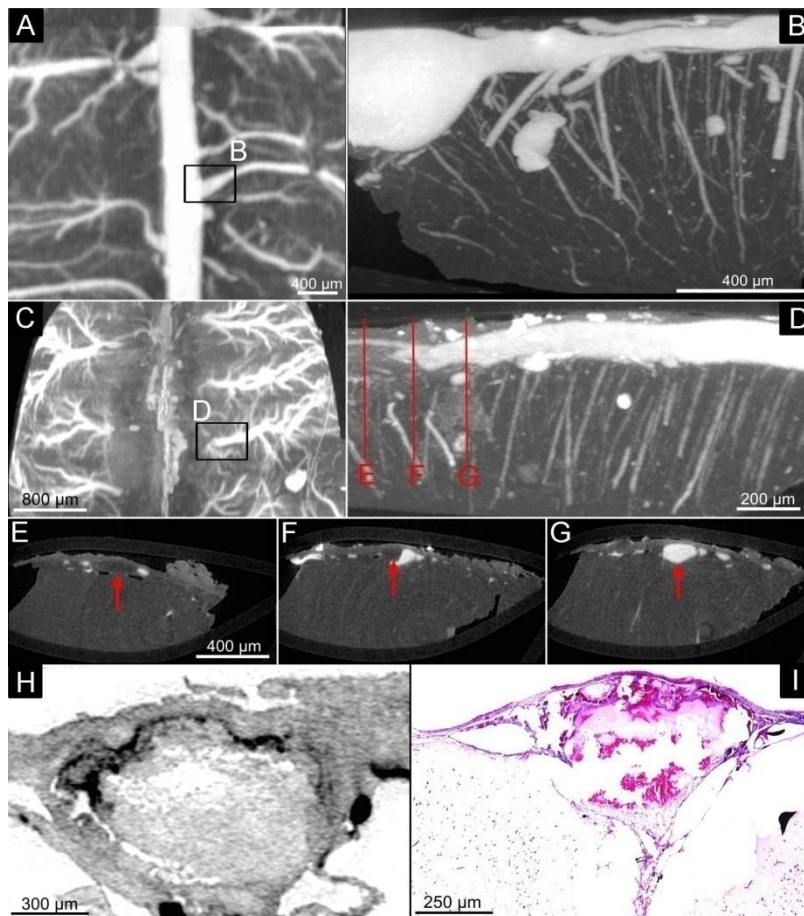
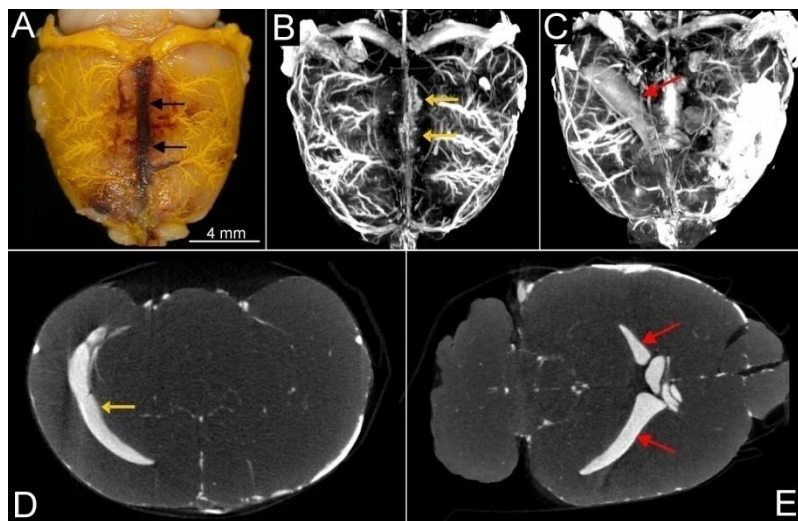


Figure 2: Vascular volume fraction obtained by 3D micro-CT demonstrating a significant decrease in the venous vascular volume fraction in the SSS thrombosis group ($p < 0.001$) compared to controls.

**Figure 3:**

A, Micro-CT and B, Nano-CT MIP showing regular contrast-enhanced inflow in the superior sagittal sinus.
C, In contrast, micro-CT (MIP) demonstrating occluded superior sagittalis sinus. D, Nano-CT imaging at the interface showing the contrast-enhanced bridge veins and the capillary system. E-G, Coronar single-slice nano-CT images demonstrate occluded (E, red arrow), partially occluded (F, red arrow) and widened (G, red arrow) bridge veins. G, Coronar single-slice nano-CT showing the thrombotic occluded sinus sagittalis superior.
I, Thrombus formation was confirmed by histology (HE staining, magnification x10).

**Figure 4:**

Macroscopic photograph of the rat brain after induced SSS thrombosis (black arrows). Corresponding micro-CT image (B, MIP) and coronar single-slice (D, yellow arrow) demonstrating SSS thrombosis (white arrows) with concomitant widened superior cerebral veins. MIP (C) and coronar micro-CT single slice image (E) demonstrates contrast enhanced lateral ventricle indicating Microfil leakage (red arrow).

Conclusion. Micro-CT and Nano-CT are feasible for analysis and differentiation of perfusion territories in an animal model of focal cerebral ischemia. It has the potential to become a standard technique for ex-vivo studies of focal cerebral ischemia.

Reference List:

- ¹ Ferro JM, Canhao P, Stam J, Bousser MG, Barinagarrementeria F. Prognosis of cerebral vein and dural sinus thrombosis: results of the International Study on Cerebral Vein and Dural Sinus Thrombosis (ISCVT). *Stroke* 2004 March;35(3):664-70.
- ² Rottger C, Bachmann G, Gerriets T, Kaps M, Kuchelmeister K, Schachenmayr W, Walberer M, Wessels T, Stoltz E. A new model of reversible sinus sagittalis superior thrombosis in the rat: magnetic resonance imaging changes. *Neurosurgery* 2005 September;57(3):573-80.
- ³ Langheinrich AC, Leithauser B, Greschus S, Von Gerlach S, Breithecker A, Matthias FR, Rau WS, Bohle RM. Acute rat lung injury: feasibility of assessment with micro-CT. *Radiology* 2004 October;233(1):165-71.
- ⁴ Langheinrich AC, Bohle RM, Breithecker A, Lommel D, Rau WS. [Micro-computed tomography of the vasculature in parenchymal organs and lung alveoli]. *Rofo* 2004 September;176(9):1219-25.

Modelling Intranasal Drug Particle Deposition and Clearance in the Guinea Pig by Micro-CT

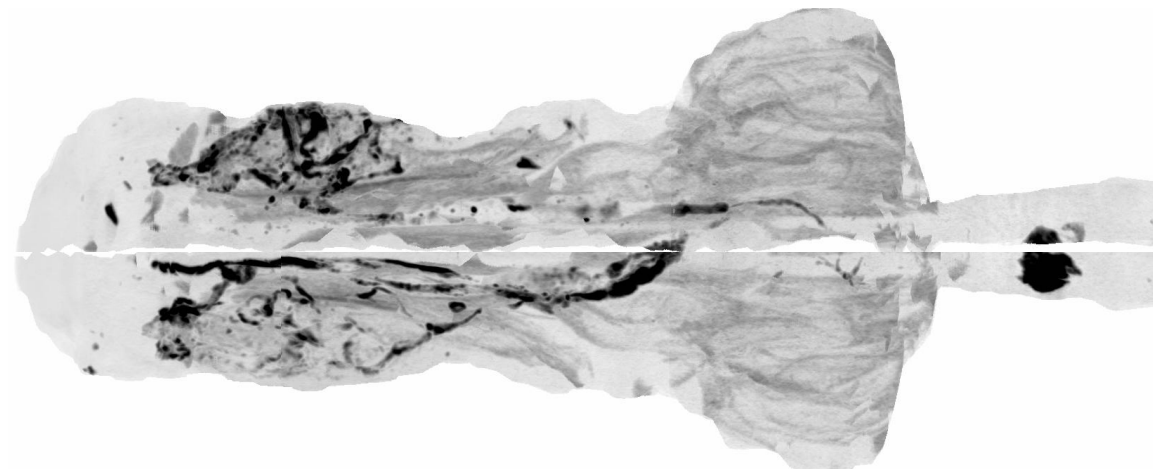
Brian Hayes, Kumar Changani, Sarah Hotee, Kashmira Pindoria, Nick Buxton and Jane Denyer

Respiratory Biology, GlaxoSmithKline R&D, Stevenage, Brian.P.Hayes@gsk.com

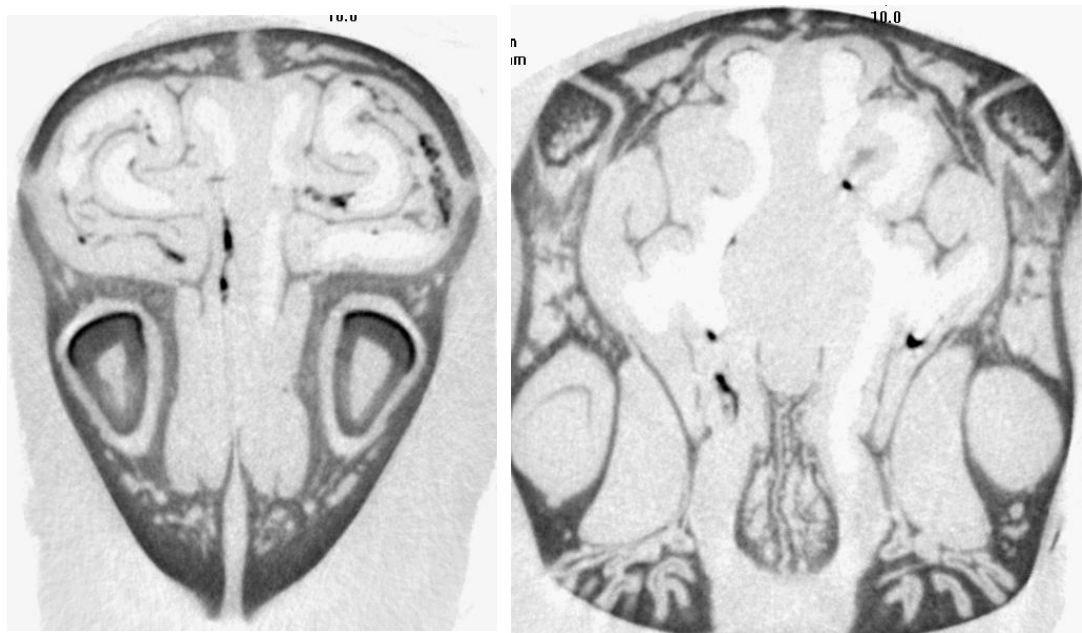
Aims. Animal models of allergic and non-allergic rhinitis are used in respiratory biology for testing and developing new treatments. In these models compounds are delivered intranasally, but there is little information on where these compounds may be deposited or the time course of clearance. To examine this in the guinea pig we made intranasal injections and carried out micro-CT analysis at different times after injection.

Method. Bilateral intranasal administration of 25 μ l barium sulphate suspension (CT contrast agent) was conducted in small groups of animals that were then sacrificed at 0.5, 1 and 24 hours after administration. The barium sulphate suspension has a particle size and viscosity relevant to intranasally dosed suspensions used in in-vivo studies in the guinea pig. The heads were dissected, fixed, and then scanned in the SkyScan 1072 micro-CT at 14 μ m resolution, and at 80kV voltage with no filtration, and sections were reconstructed from 3 overlapping scans for each head. Distribution of the contrast agent was examined in micro-CT sections, with volume measurements and longitudinal maximum intensity projections being made to examine the 3D particle distribution throughout the nasal cavities, and from side to side of the nose. We also made histological sections, stained them with eosin, and examined the distribution of the barium sulphate by confocal microscopy to find whether particles were confined to nasal cavities or taken up by the nasal mucosa.

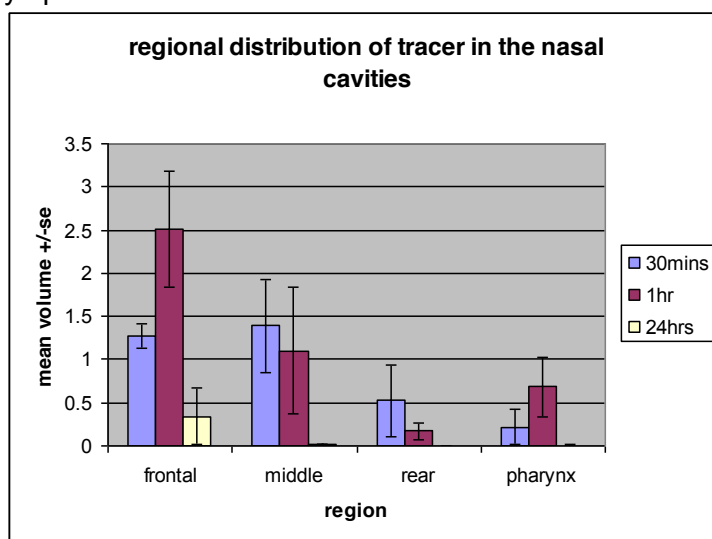
Results. The images and volume measurements showed that the barium sulphate suspension deposited mainly within the frontal third of the nasal tract with rapidly declining deposition towards the rear at 0.5 to 1 hour after administration. An example horizontal longitudinal maximum intensity projection at 0.5 hours is shown below.



The projection shows the barium sulphate deposits (black) mainly towards the front of the nose (on the left). Nasal turbinates appear grey. Barium sulphate was also found in the pharynx (black area to the right of the image), indicating that mucociliary clearance was under way. There was a three-fold variation between individual animals in total volume deposited in the nose, and a smaller variation from side to side.



Example micro-CT sections showing barium contrast medium in the nasal cavities at 0.5 hours towards the front (image on left) and middle of the nose (image on right). Confocal microscopy of histological sections confirmed that the barium sulphate was within nasal cavities without any uptake into the nasal tissues.



The histograms show the regional distribution of the tracer from the front to the back of the nose at different times after administration.

At 24 hours, 90% of the contrast agent had been cleared from the nose, with a small amount remaining in the frontal nasal cavities.

Conclusion. These results show the importance of understanding delivery of particulate suspension to the nose and the relevance of imaging modalities such as CT which may play an important role for translation into the clinic.

Tomographical Acquisition Geometries and Reconstruction Algorithms

Y. Bresler^{1,2}

¹ Department of Electrical and Computer Engineering, CSL, 1308 W. Main St. Urbana, IL 61801, USA, ybresler@illinois.edu

² InstaRecon, Inc., EnterpriseWorks, 60 Hazelwood Dr., Champaign, IL 61820, USA, Bresler@instarecon.com

Abstract

Tomographic imaging underlies nearly all of the diagnostic imaging modalities, including x-ray computed tomography (CT), positron emission tomography (PET), single photon emission tomography (SPECT), and certain acquisition methods for magnetic resonance imaging (MRI). X-ray CT is also widely used for airport baggage inspection, in nondestructive evaluation (NDE), and in micro CT for pre-clinical imaging and scientific discovery.

In this paper, we focus on x-ray computed tomography. We review the different data acquisition geometries in CT, all the way from parallel beam through cone beam and helical cone beam to inverse geometry. We discuss the acquisition requirements and their relationship to image resolution and artifacts. We then review image reconstruction algorithms starting with parallel-beam filtered back projection, through the FDK cone beam algorithm, and Katsevich algorithm for helical cone beam, to iterative reconstruction algorithms.

Finally, we address the computational requirements of the different tomographic reconstruction algorithms. These requirements scale as N^3 for an $N \times N$ pixel two-dimensional image, and as N^4 for an $N \times N \times N$ voxel three-dimensional image. This unfavorable scaling, which implies a factor of 8 or 16 increase in the computation for every doubling of the image matrix size, requires large computation resources or long waiting times for the reconstruction. In the case of micro CT, the delay between experiment and result, and the limitation on reconstruction throughput, can limit the pace of technological advances, drug testing, or scientific discovery.

We review progress in fast reconstruction algorithms to address these challenges, and introduce a novel family of fast algorithms that reduce the computational requirements from $O(N^3)$ to $O(N^2 \log N)$ in 2D, and from $O(N^4)$ to $O(N^3 \log N)$ in 3D. These algorithms are applicable to all imaging geometries, and for images of sizes typical in micro CT provide in practice acceleration between 10x to 50x on the same hardware.

In the mid 1980's it was widely believed that CT was a mature field, and that future improvement would be only incremental. As recent history has shown, nothing could be further from the truth. Technological and scientific innovation in CT is thriving, and the future of CT is bright.

Characterization of root canal curvatures by description of the axis based on microCT imaging

C. Dobo-Nagy¹, A. Kovacs², L. Szilagyi³, B. Benyo³

¹ Independent Section of Radiology, Semmelweis University, Budapest, ²Dept. of Architecture of Representation University of Technology and Economics, Budapest, ³Dept. of Control Engineering and Information Technology, Budapest University of Technology and Economics, Budapest, Hungary

Introduction: Every root canal of the teeth has its own individual form; therefore, guidelines are required in both endodontic practice (root canal treatment) and research for the purpose of simplification. Knowledge of the root canal shape helps in making the selection of the best technique or choosing the most appropriate instrumentation of a given root canal treatment a priori.

Cone-beam computer tomography (CBCT) was recently introduced in clinical dental radiology. This modality is essentially the same in the way of image records to that of the microCT. Experiments carried out on extracted human teeth using microCT serve as a basis of clinical use of CBCT.

Purpose: The purpose of this study was to give a mathematical description of 3D centreline of root canals of extracted human teeth using microfocal x-ray source records.

Materials and methods: Fifty one-rooted teeth were scanned with a microCT (SkyScan 1172) where the voxel size was 10x10x10 micrometer. Approximately 1000 reconstructed cross sections of each root were used for further analysis. In this study we introduced a complete image processing procedure, which started with the enhancement of input microCT slices, continued with 2D image segmentation based on an enhanced fuzzy c-means clustering [Szilagyi et al. 2003] identification of the centre points via a region growing method. During the automatic segmentation, the centre point was determined by four-clustered image first and sequential iteration of clustered images resulted in the binary image having a detected centre point (Fig. 1.). This centre of gravity was solved as a point of the root canal axis at the given level. Finally centres of gravity were determined at each reconstructed slices and the set of these centres of gravity were taken as the 3D root canal axis. Approximating a fourth degree polynomial function to the set of the centre of gravity provided a simple space curve. The Gaussian least square method was used to fit a polynom to the centre of gravity points. The root canal axis was determined and visualized by the MathCAD 14.0 software. Fitting of root canal axes and functions were determined with correlation coefficients. The basis of the computer graphyics alignment were (1) the determination of the set of curvature values, the mean curvature value and the maximum curvature value as well as the torsion value; and (2) view projections of the spatial polynomials being as plain curvatures. For this later analysis our previously described method was used [Dobo-Nagy et al. 1995]. For comparison, third degree and fifth degree polynomial function approximation were also carried out.

Results: The correlation coefficient value of the fourth degree polynomial function was found to be between 0.980-0.999 for all of the cases. Approximation of curvatures by any other degree polynomial function resulted in lower correlation coefficient values.

The 3D appearance of a root canal may highly different from its 2D views. The projections of the each 3D centreline from different views appeared as different plain curvatures (Fig. 2.).

Conclusion: The centreline of the root canal was interpolated as a spatial fourth degree polynomial function. The repetition of the fourth degree polynomial approximation appeared to be the most reliable to date. We could simplify the 3D individual form of real root canals. This kind of mathematically based simplification might improve the endodontic practice if it were successfully embedded in a novel dental imaging modality (e.g. CBCT).

References:

- C. Dobo-Nagy, J. Szabo, J Szabo (1995): A mathematically based classification of root canal curvatures on natural human teeth. *J. Endodontol.* 21(11):557-560.
 L. Szilagyi, Z. Benyo, SM Szilagyi, HS Adam (2003): MR brain image segmentation using an enhanced fuzzy c-means algorithm. Proc 25th Ann Int'l Conf IEEE EMBS, Cancun, Mexico, 724-726.

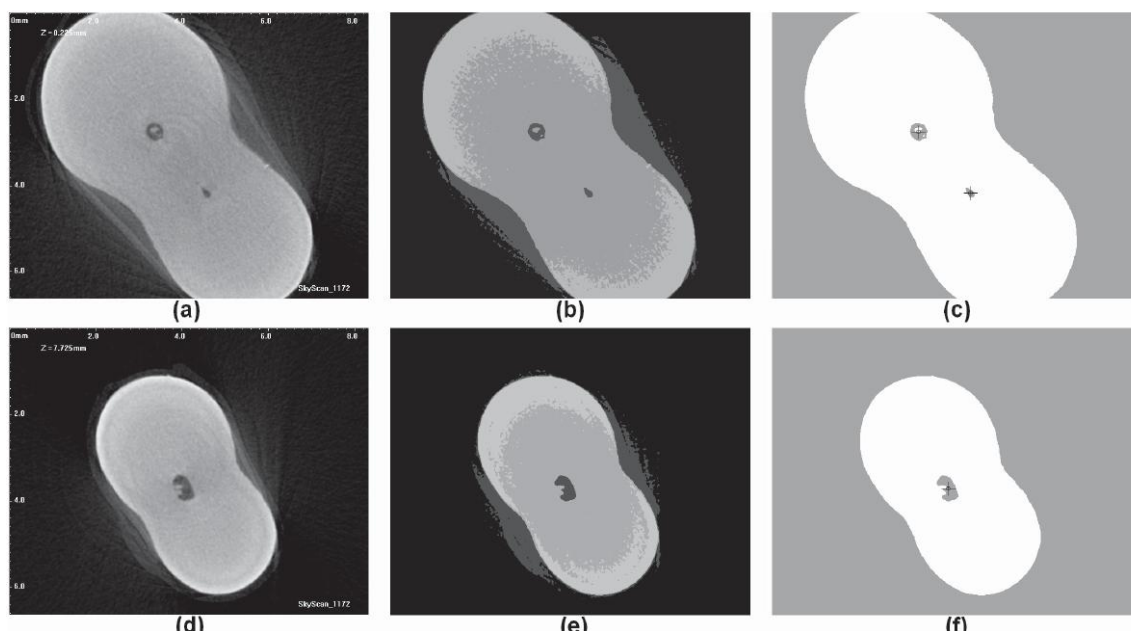


Fig. 1. Detailed presentation of image segmentation of reconstructed microCT slices
 First column shows the original recorded images; second column presents clustered images (four coloured image) with a preliminary centre of gravity; third column indicates segmented binary images with detected centre of gravity points at the end if iteration.

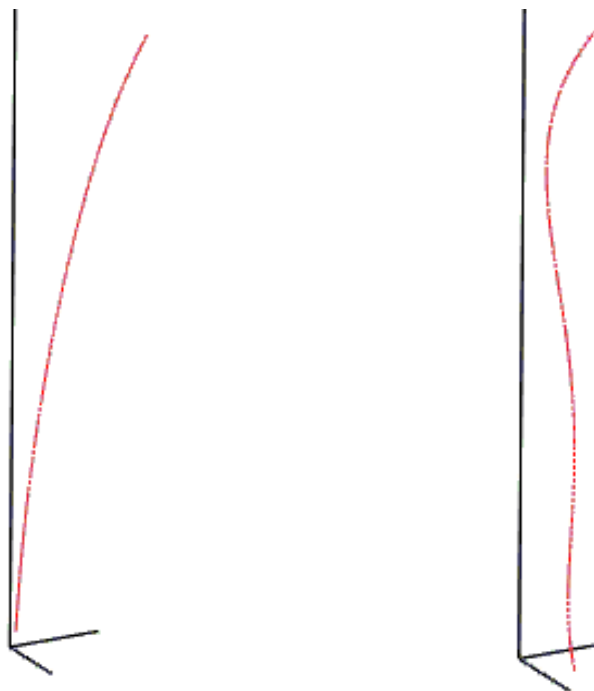


Fig. 2. Different appearances of the same 3D centreline

Two different projections of the same root canal are shown in this figure. Notice the big difference in their appearance. The left looks as a gradual simple curve, while the right looks as a severe double curvature. This example represent that the 3D visualisation is superior to the 2D view.



Application note

Acquiring optimal quality X-ray µCT scans

Mark F.V. Tarplee¹, Nick Corps²

¹Centre for Micromorphology, Department of Geography, Queen Mary, University of London, Mile End Road, London, UK. E1 4NS M.Tarplee@qmul.ac.uk

²e2v scientific instruments, Sirius House, Watery Lane, Wooburn Green, Bucks, UK. HP10 0AP

INTRODUCTION

X-ray computed tomography (CT) has, as with many analytical techniques, inherent problems that need addressing in order to achieve optimal quality results (Ketcham and Carlson, 2001; Mees et al., 2003; Davis and Elliott, 2006). Problems may not always be readily apparent, depending on the nature of the material being analysed. However, artefacts associated with such issues are almost always present and, especially where quantitative analyses are being conducted, can significantly compromise the quality of the resultant data (Ketcham and Carlson, 2001; Davis and Elliott, 2006). Equally, there are a number of simple adjustments that can be made to achieve the best overall scan quality. Though there is no substitute for a detailed understanding of the principles of X-ray CT and hence how to optimise its application; a lack of time, funding and/or an appropriate technical background prohibits many users from acquiring such a level of knowledge and insight. The purpose of this application note is to facilitate general users of SkyScan instruments to identify the inherent problems particular to the type(s) of material that they are analysing, take the necessary steps to resolve those issues and hence achieve the highest possible quality scans within realistic time and resource constraints.

Background information

Dr Mark Tarplee's primary expertise and X-ray µCT experience is in the analysis of geological samples, especially glacial sediments. Such samples present unusual challenges, particularly because of the often heterogeneous nature of the compositional element densities. However, the measures that are applied to mitigate such problems are applicable to all materials and so should be of relevance to all X-ray tomograph users. Mr Nick Corps is SkyScan Engineer for e2v scientific instruments, the UK distributor. He played a crucial role in helping Dr Tarplee to gain the knowledge and experience required to write this note, and the 'X-ray µCT operation manuals' on which it is based (Tarplee & Corps, 2008).

All of the samples were analysed using a SkyScan 1072 desktop X-ray microtomograph with a 20-100kV/0-250µA X-ray source.

PROBLEMS AND 'SOLUTIONS'

Beam hardening

What is beam hardening?

In order to understand the phenomenon of beam hardening, the nature of the X-ray cone beam generated by SkyScan μ CT instruments, and all laboratory based 'stand-alone' X-ray computed tomographs, must be appreciated. This can be facilitated by comparing such X-ray beams to those produced within a synchrotron (a sub-atomic particle accelerator). A synchrotron generated beam can be modified to produce a monochromatic X-ray beam, essentially a stream of X-rays with a specific voltage and intensity (Cnudde et al., 2008). If such a beam passes through a sample (or filter) of a specific pure material and thickness, the energy of the ray will be attenuated by n (50% for illustrative purposes). Placing another sample/filter of exactly the same type and thickness in the line of the beam will reduce the energy of the beam by the same value again, i.e. 50% thus cumulatively reducing overall X-ray beam energy by 75% (Fig. 1a).

'Off the shelf' X-ray CT system sources produce a polychromatic beam - a stream of X-rays with a spectrum of voltages, e.g. zero to 100kV for the SkyScan 1072 and 1172 instruments. A sample/filter of a specific pure material and thickness will block or absorb the lowest energy rays, e.g. the lowest 68% of the spectrum (for illustrative purposes), and attenuate the higher energy rays (Fig. 1b) (Davis and Elliott, 2006). Placing a second sample/filter within the line of the spectrum will remove the lowest part of the REVISED (partially attenuated) energy spectrum and further attenuate the remaining part of the beam. Hence the reduction in the overall X-ray energy spectrum transmitted through each of the samples/filters is not linear (unlike for the monochromatic beam).

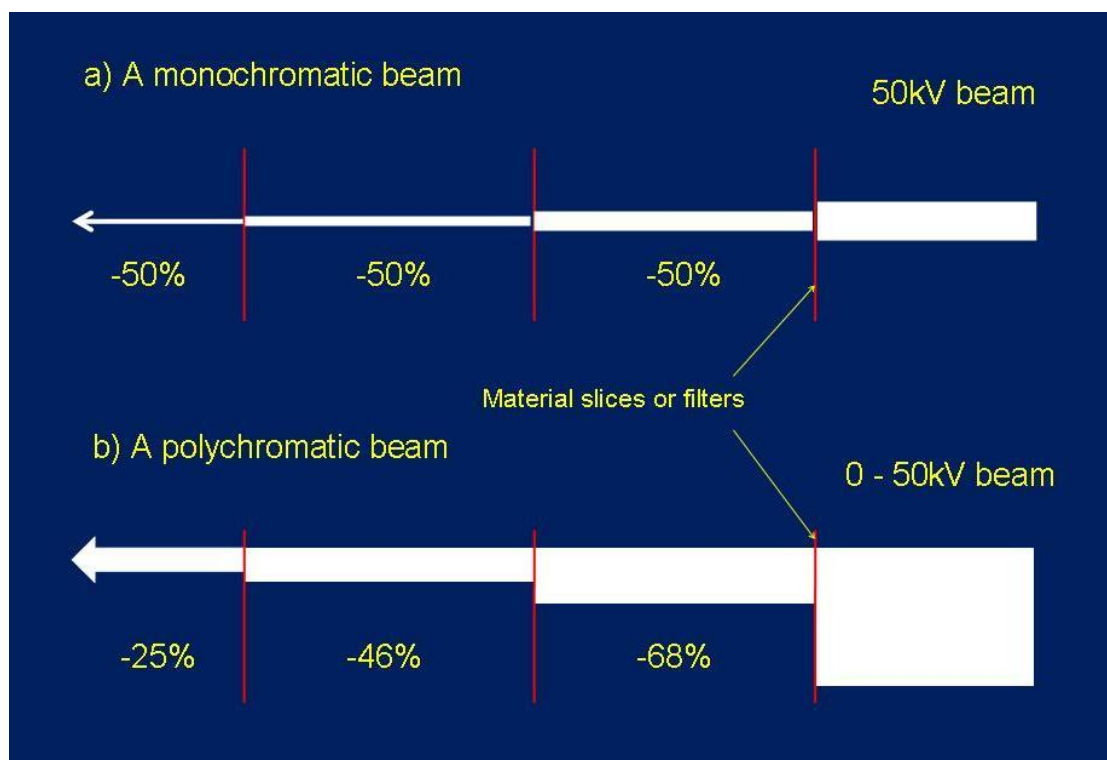


Figure 1. A schematic diagram to illustrate the effect of filtering on both a monochromatic (as generated by synchrotrons) and polychromatic (as generated by self-contained X-ray CT scanners) X-ray beams (see text for a detailed explanation).

What does beam hardening look like?

It is manifest mainly as a (artificially) high relative density zone at the edge of a sample, where a significant number of low energy X-rays are blocked/absorbed (Fig. 2a,b). However, it is a pervasive phenomenon, potentially (significantly) effecting all parts of a specimen.

How can it be reduced?

- Filtering the X-ray cone beam before or after it passes through the sample, but before it reaches the detector. By doing so you remove (filter out) the lower energy part of the spectrum thus reducing, or potentially eradicating, the problem (Fig. 2c,d). Filters have to be 99+% pure, in order to avoid increasing the noise within the resultant scan image, and are usually metal. There are a number of standard filter materials and thicknesses, a selection of which are listed below (Table 1). Also presented are data based on an arbitrary* threshold value, the portion of the energy spectrum beneath which will be blocked, for a selection of X-ray polychromatic beam applied maximum voltages, i.e. zero – n.

Table 1. Some standard metal filters used to filter polychromatic X-ray beams and indicative threshold values for different applied voltages (see text for details).

Filter	Thresholds (10%* of the peak intensity value - keV) . Applied voltages (n) are in parentheses					
	(50kV)	(60kV)	(70kV)	(80kV)	(90kV)	(100kV)
Al, 0.25mm	8.0	8.0	8.0	8.0	8.0	8.0
Al, 0.5mm	9.5	9.0	9.0	9.5	9.5	9.5
Al, 1.0mm	12.5	12.5	13.0	13.0	13.0	13.0
Cu, 0.04 + Al, 0.5mm	14.5	14.5	14.5	15.0	15.0	15.0
Cu 0.125mm	18.5	18.5	18.5	19.0	19.0	19.0

(*selected for illustrative purposes) (data courtesy of Dr Phil Salmon, SkyScan)

There is a limit to the degree of filtering that can be done, largely dependant on the maximum power of the source. A minimum 40% average saturation of the detector MUST be achieved (across an empty field of view, i.e. no sample present) to ensure that accurate results are obtained. Conversely, there is also a minimum degree of filtering required to ensure that saturation does not exceed 65% (though that eventuality is less likely during 'normal' use).

- By applying a beam hardening correction during the reconstruction process (Fig. 2e,f). See the SkyScan NRecon User Guide and Tarplee & Corps (2008) for details of this approach.
- As scans are rotational, it is advantageous that the sample be either spherical or cylindrical. Alternatively, the sample can be packed in a spherical or cylindrical container comprised of, or containing, a material of a similar density to the (main) constituent of the sample. For example, a 99+% pure quartz sand could be used to pack an irregularly shaped sandstone specimen in a container (wrapping the specimen in 'cling film' would prevent contamination by the packing material). The quartz sand would have similar attenuation characteristics to quartz grains within the rock. Thus irregular shaped samples can be pseudo converted into a regular form, with a consequent reduction in beam hardening artefacts, or at least their (partial) adaptation to regular and easily recognisable forms.

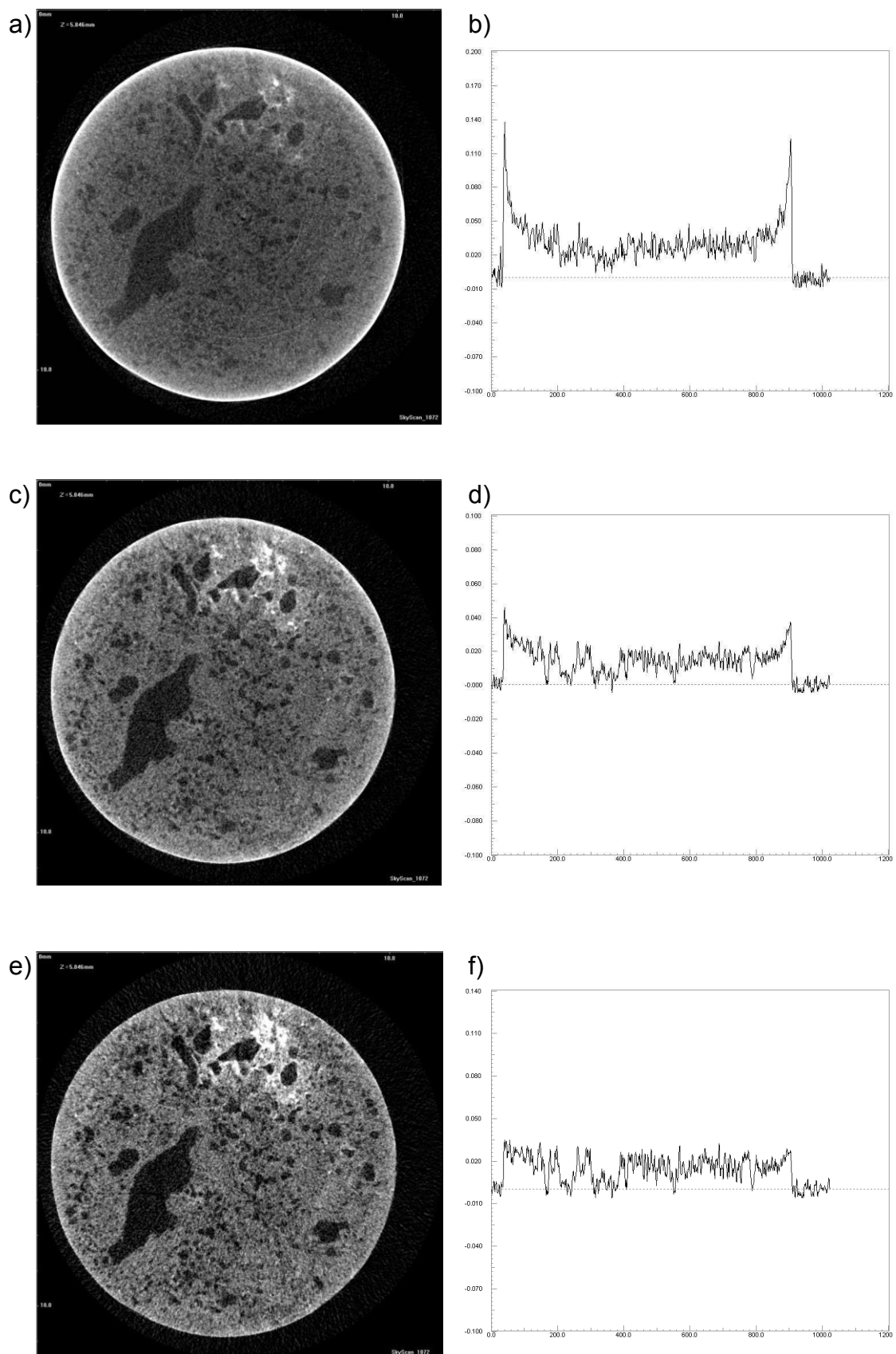


Figure 2a-f. A reconstructed cross-section of a 10mm Ø core derived from a block of fired clay (a house brick), illustrating the phenomenon of beam hardening and the effects of mitigating measures. a) The image was produced by scanning without a filter and with no

beam hardening correction applied. Note the corona at the edge of the sample. This is completely artificial, i.e. there is no density variation within this part of the sample (unlike the spots of relatively very dense material in the top right quadrant). b) An attenuation coefficient profile across the centre (from left to right) of the cross-section, illustrating the dramatically increased values at the edge – known as a cupping artefact (Van de Casteele et al., 2004). c) The result of rescanning with a Al 0.5mm thick filter placed in front of the camera to block the <12-13kV section of the polychromatic beam spectrum, but with no beam hardening correction applied. Note that the contrast is better (see ‘Maximising contrast’ for details of why) and hence that the spots of relatively very dense material in the top right quadrant are more prominent and better defined, as are the voids. d) An attenuation coefficient profile across the centre of the filtered cross-section, illustrating the significant reduction in the cupping artefact. e) The same scan as in c/d, but with a 40% beam hardening correction applied. Note that there is now no apparent beam hardening artefact (corona) at the edge of the sample. The contrast between the voids, medium density material (clay) and the relatively very dense material in the top right quadrant is excellent in comparison to previous images. Artefacts are still present, but the scan was relatively rapid and consequently not of optimal quality. f) An attenuation coefficient profile across the centre of the filtered and beam hardening corrected cross-section, illustrating the absence of any significant cupping artefact (the profile is approximately horizontal). Note that such highly irregular profiles, reflecting the variation in density within this type of material, are to be expected when scanning such specimens – indicative of the significant (and often problematic) natural variation within geological and geomaterial samples.

Other issues

Misalignment

Though there is always a requirement for a minor misalignment correction during reconstruction, it should not normally exceed 100 μm . Any more indicates that the source, stage and camera are out of alignment and need realigning (SkyScan, 2001; Davis and Elliott, 2006).

Alignment checks should be carried out regularly, the period dependant on the workload of the machine, i.e. if large numbers of scans are conducted each week an alignment correction should be done at the start of each new session. When fine tuning the unit to ensure a <1.0 pixel error, correct by approximately $\frac{1}{2}$ the misalignment value, i.e. if the value is 1.0, correct by 0.5 thereby avoiding overcompensation issues.

Blurring of shadow images

Can be caused by either movement of the sample on the stage or motion within the sample, e.g. of constituent parts or the substrate within which the sample is contained (Davis and Elliott, 2006).

The solutions are to:

- a) Secure the sample properly to the stage using ‘blu-tack’, double-sided adhesive tape or pads, water-soluble glue etc.
- b) Granular samples should be firmly tamped and packed in place, e.g. with cotton wool.
- c) Only fluids/gels that are of sufficiently high viscosity that they will not be perturbed by the rotation of the stage should be used as a sample substrate.

Interference from the stage

The base of the sample, proximal to the stage, can be affected by beam hardening associated with the metal mount.

By placing the sample on a polystyrene block or (in a) sheath, the specimen can be clearly separated from the stage.

Initial fluctuations in source output

During the first 5-15mins of operation the X-ray spectrum emitted from the source fluctuates.

Allow the source to stabilise for 10-15mins before doing any analyses, i.e. even before checking minimum and maximum transmission levels.

ACQUIRING AN OPTIMAL QUALITY SCAN

Maximising contrast

Filtering changes the X-ray source output characteristics detected by the scintillator, i.e. the camera receives a weaker signal. (Fig. 2a-d and 3a). To compensate for these changes a flat field correction must be applied (Fig. 3b). If a parameter is adjusted, i.e. voltage, current, exposure time or filter a new flat field correction MUST be acquired as the old one is now invalid. Essentially the flat field correction is an adjustment to the camera such that it will just detect the most energetic part of the X-ray spectrum being produced (and all less energetic rays), thereby avoiding underexposure. With the flat field correction acquired the camera will be at an average of 90-95% saturation, thereby also avoiding overexposure (Tarplee & Corps, 2008). If there is not a >90% average saturation level the flat field needs updating.

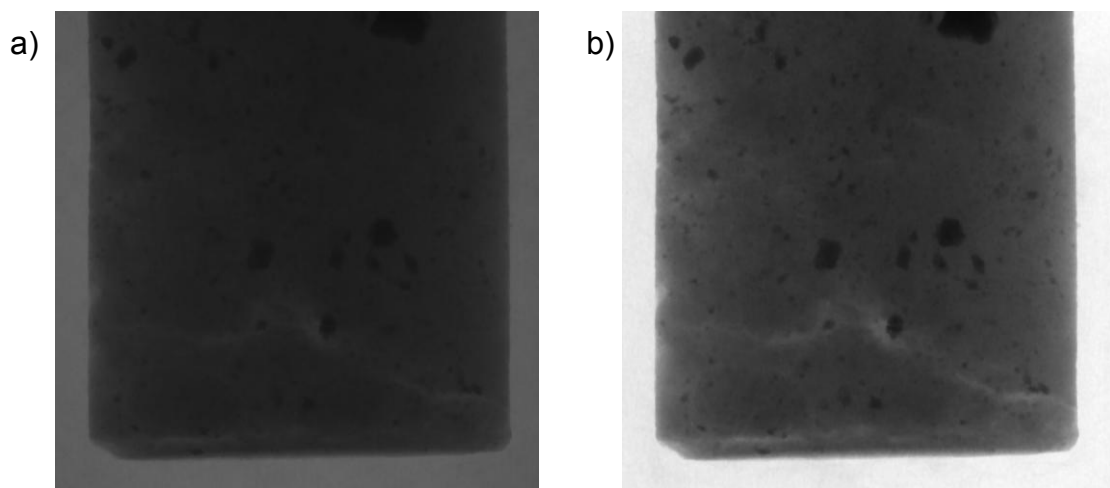


Figure 3. Two shadow images of the same sample, illustrating the contrast enhancement achieved by applying a flat field correction (part of an oversized, multiple section scan, hence the top of the sample is not visible). a) A 'raw' image (no flat field correction applied) illustrating the dimming effect of placing a Cu 0.038mm filter over the detector window, thereby reducing the percentage of the X-ray beam incident on the scintillator (though there is >40% saturation) and hence the contrast. b) The compensatory effect produced by applying an accurate flat field correction and hence restoring the contrast. Note that the area outside the sample is slightly off-white indicating that the camera is not entirely overexposed (though there is >90% saturation).

What the flat field correction does not address is the minimum transmission level. A relatively powerful beam will pass easily through specimens with low attenuation coefficients,

i.e. samples that are low density and/or have a low atomic number or are very thin. Hence the contrast achieved in the resultant scan will be poor and consequently the data could be of little use, certainly not optimal. However, by simply lowering the voltage the minimum transmission level can be reduced and the contrast increased as a consequence. Unfortunately close to the zero transmission level all sorts of other problems develop and so it is advisable to keep the minimum transmission above 5%, WITH THE FLAT FIELD CORRECTION APPLIED (Tarplee & Corps, 2008). Establishing an optimal minimum transmission level can be straight forward or somewhat involved, depending on the nature of the material being analysed and hence the maximum voltage setting applied. However, one important rule is to maximise the current at whatever voltage is selected. By doing so the photon flux is maximised and hence the signal to noise ratio, improving scan quality further (Davis and Elliott, 2006). For step-by step guidance reference should be made to Tarplee & Corps (2008).

Other settings and adjustments

Frame averaging

Very much a case of 'more is better'. However, increasing the frame averaging by one will increase the length of the scan by a value calculable by multiplying the exposure time by the number of steps selected to conduct a 180° or 360° scan (see below). Essentially, increasing the frame averaging from one to two doubles the scan time, x3 = treble, x4 = quadruple and so on. A frame average of four is the best compromise between quality and length of scan for the SkyScan 1072, but may well not apply to other instruments (Tarplee & Corps, 2008).

Rotation step

Again, very much a case of 'more is better', but reducing the size of the incremental rotation of the sample between image capturing will have a commensurate impact on both scan time and the size of the resultant dataset. Despite continuing significant technological advances in both computer hard- and software, at the current time (April 2009) very large datasets, i.e. $>1024^3$ are extremely difficult to visualise efficiently in volumetric 3D. If small rotational increments are desired, the resultant dataset can be reduced in size by binning.

180° or 360° scan?

Common sense dictates that a 360° scan will be better than a 180° scan as not only is the whole sample scanned twice, but the impact of persistent artefacts (such as streak artefacts) is minimised. However, where high throughput of materials is essential, 180° scans are an obvious compromise between quality and minimising scan time.

References

1. Cnudde, V., Masschaele, B., Vlassenbroeck, J., Dierick, M., De Witte, Y., Lehmann, E., Van Hoorebeke, L., Jacobs, P.J.S., 2008. X-rays and neutrons used for the visualisation of oligomeric siloxanes. Hydrophobe V, 5th International Conference on Water Repellent Treatment of Building Materials. Aedificatio Publishers, 31-42.
2. Davis, G.R., Elliott, J.C., 2006. Artefacts in X-ray microtomography of materials. Materials Science and Technology 22, 9, 1-8.
3. Ketcham, R.A., Carlson, W.D., 2001. Acquisition, optimization and interpretation of X-ray computed tomographic imagery: applications to the geosciences. Computers & Geosciences 27, 381-400.
4. Mees, F., Swennen, R., Van Geet, M., Jacobs, P., 2003. Applications of X-ray computed tomography in the geosciences. In: Mees, F., Swennen, R., Van Geet, M., Jacobs, P., (Eds.),

- Applications of X-ray computed tomography in the geosciences, Geological Society Special Publication, London, pp. 1-6.
- 5. SkyScan n.v., 2001. SkyScan 1072 Desktop x-ray Microtomograph Instruction Manual, Aartselaar.
 - 6. Tarplee, M., Corps, N., 2008. Skyscan 1072 desktop X-ray microtomograph. Sample scanning reconstruction, analysis and visualisation (2D and 3D) protocols. Guidelines, notes, selected references and F.A.Qs.<http://www.geog.qmul.ac.uk/docs/staff/4952.pdf>
 - 7. Van de Casteele, E., Van Dyck, D., Sijbers, J., Raman, E., 2004. A model-based correction method for beam hardening artefacts in X-ray microtomography. Journal of X-ray Science and Technology. 12, 43-57.

Aurovist contrast enhancement in healthy mice.

Inneke Willekens^{1,2}, Tony Lahoutte¹, Phil Salmon³, Nico Buls², Vicky Caveliers¹, Rudi Deklerck⁴, Axel Bossuyt¹ and Johan de Mey²

¹ In vivo Cellular and Molecular Imaging - ICMI - Vrije Universiteit Brussel

² Department of Radiology - UZ Brussel

³ SkyScan – Kontich

⁴ Electronics and Informatics - ETRO - IRIS - Vrije Universiteit Brussel

Purpose: To evaluate the time-course of contrast-enhancement of spleen, liver, and blood using Aurovist in healthy mice.

Methods: Healthy C57bl/6 mice (n=2) were used. Anesthesia was induced with 5% isoflurane and maintained at 2% during the scan with spontaneous breathing via a mask. Aurovist (Nanoprobes, New York, USA) was administered intravenously at a dose of 200 µl. Aurovist is a contrast agent containing gold nanoparticles ¹. Imaging was performed using micro-CT (SkyScan 1178 micro-CT system; SkyScan, Kontich, Belgium) at a resolution of 83 µm. The total acquisition time was 6 min. Each animal underwent a micro-CT scan before contrast injection, immediately after contrast injection and at 1h, 2h, 3h, 4h, 6h, 24h and 48h after contrast. Images were reconstructed using filtered backprojection (NRecon, SkyScan) and analysed using Amide (Loening et al). Regions of interest (ROIs) were drawn in spleen, liver, and left ventricle. The contrast enhancement was measured and expressed in function of time.

Results: Our results demonstrate that Aurovist contrast enhancement of the liver and spleen reaches a maximum at 48h. The peak contrast enhancement of the liver is 85%, while the best enhancement of the spleen is 231%. Enhancement in the heart lasts for at least 6h. In comparison with *in vivo* small animal blood pool iodine contrast agents like Exia 160, Fenestra LC and VC ², the Aurovist contrast is more intense and permits much longer blood retention.

Conclusion: Aurovist provides longlasting contrast with very high contrast enhancement.

References:

1. JF Hainfeld, DN Slatkin, TM Focella, HM Smilowitz. Gold nanoparticles: a new X-ray contrast agent. Br J Radiol 2006;79:248-253
2. I Willekens, T Lahoutte, N Buls, C Vanhove, R Deklerck, A Bossuyt, J de Mey. Time-course of contrast enhancement in spleen and liver with Exia 160, Fenestra LC and VC. Molecular Imaging and Biology 2009;11(2):128-35

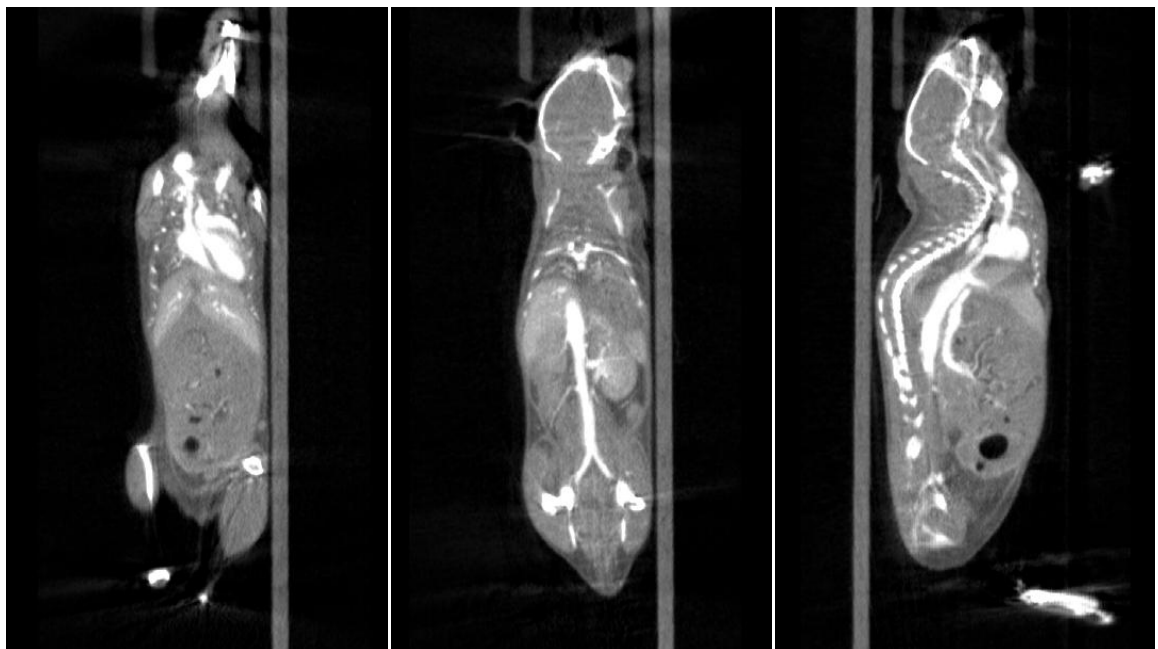


Figure 1: Two coronal and sagittal micro-CT images just after contrast injection.

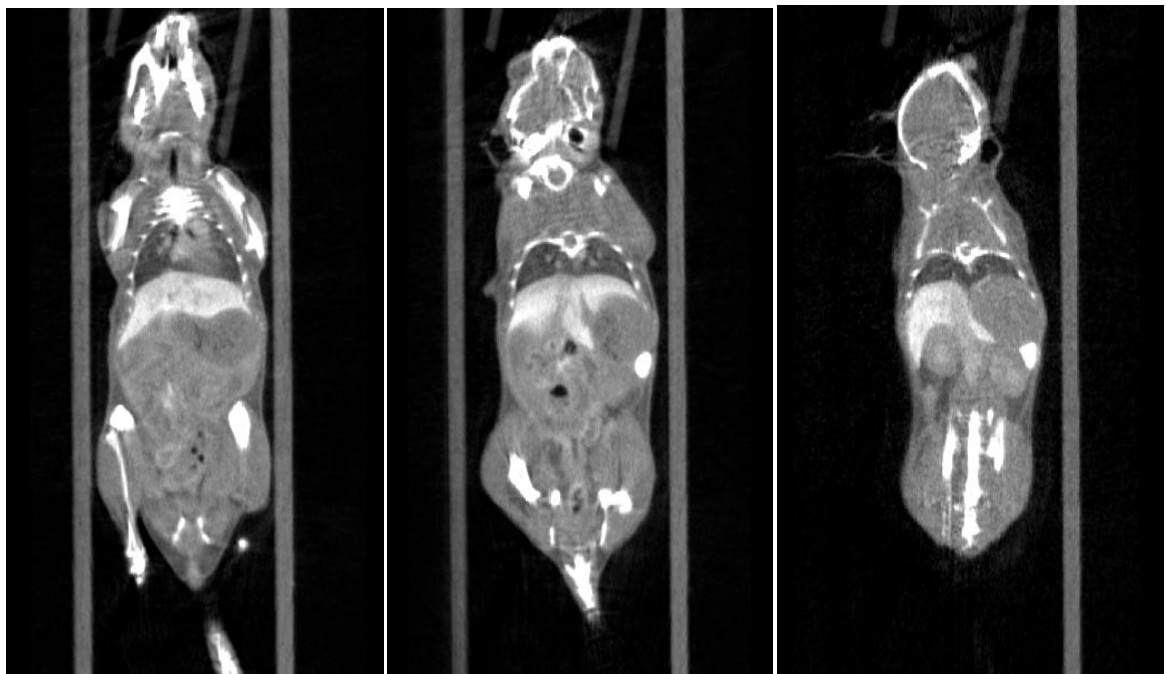


Figure 2: Three coronal micro-CT images 48h after contrast injection.

Validation of a densitometric calibration protocol in microCT

R. Stoico¹, S. Tassani^{1,2}, F. Baruffaldi¹, M. Viceconti¹

¹ Laboratorio di Tecnologia Medica, Istituto Ortopedico Rizzoli, Bologna, Italy,
stoico@tecnio.ior.it

² Engineering Faculty, University of Bologna, Italy

Aims. The aim of the present work was to validate a densitometric calibration protocol in micro computed tomography using gravimetric procedure, *ash* density, for the calculation of bone mineral density.

Method. A group of 30 healthy trabecular bone specimens were selected to validate the densitometric calibration protocol. Specimens were ashed in a muffle furnace at 650 degrees for 24 hours. The *ash* density (ρ_{ASH}) was calculated as the ash weight divided by the specimen volume and was found to range between 200 and 500 mg/cm³. The ρ_{ASH} is considered the golden standard for densitometric analysis, therefore was used in order to validate the micro computed tomography (microCT) calibration protocol. The densitometric calibration protocol in microCT was based on the use of a distilled water pet and two densitometric phantoms (250 and 750 mg/cm³ hydroxyapatite (HA) bone-equivalent density). Acquisition settings for both water and densitometric phantoms were 50kV, 200 μ A and 5.9s exposure time for each frame. The final image was obtained by averaging two frames, as previously published [1, 2]. An 1-mm Aluminium (Al) filter was used to reduce beam hardening effect. The rotation step was set at 0.90° to reduce the time of the acquisition. The magnification was set at 16x in order to obtain a pixel size of 19.5 μ m and a field of view of 20x20mm. The densitometric phantoms were dipped in saline to reproduce the same experimental set-up of trabecular bone specimens. The two phantoms were acquired together in the same holder. The tomographic acquisitions of distilled water and phantoms were reconstructed in 8-bit format with the beam hardening correction implemented in the reconstruction software. The beam hardening correction was set at 30%. The reconstructed slices of the water and the densitometric phantoms were obtained by using the same reconstruction parameters of the trabecular bone specimens. The cross section images of these specimens were obtained using the grey level scale, with white set to 0 value and black set to 255 value. The densitometric calibration protocol was divided in two steps: 1) Hounsfield Unit (HU) densitometric calibration by using water phantom and 2) bone mineral density (BMD) calibration by using densitometric phantoms. A density range calibration was necessary to change the grey level index scale in HU scale. It was performed by using all the reconstructed slices of distilled water phantom. After that the BMD calibration was performed. A stack of 481 and 466 reconstructed slices of 250mg/cm³ and 750mg/cm³ densitometric phantoms respectively were used to perform the BMD calibration. The same round region of interest (ROI), diameter 341pixel, was used during the application of the densitometric calibration protocol and its validation. According to the densitometric calibration protocol, the BMD was obtained by averaging the trabecular bone and the marrow density because the volumetric density of trabecular framework is generally under estimated due to partial volume effect. The BMD of trabecular bone specimens was associated with ρ_{ASH} to validate the calibration protocol.

Results.

A linear correlation (slope = 1.2) between ρ_{ASH} and BMD was found (Figure 1). The slope of the linear correlation was not found in line with the results of literature were a value equal to one is suggested. However, the parameters resulted well-correlated ($R^2=0.91$).

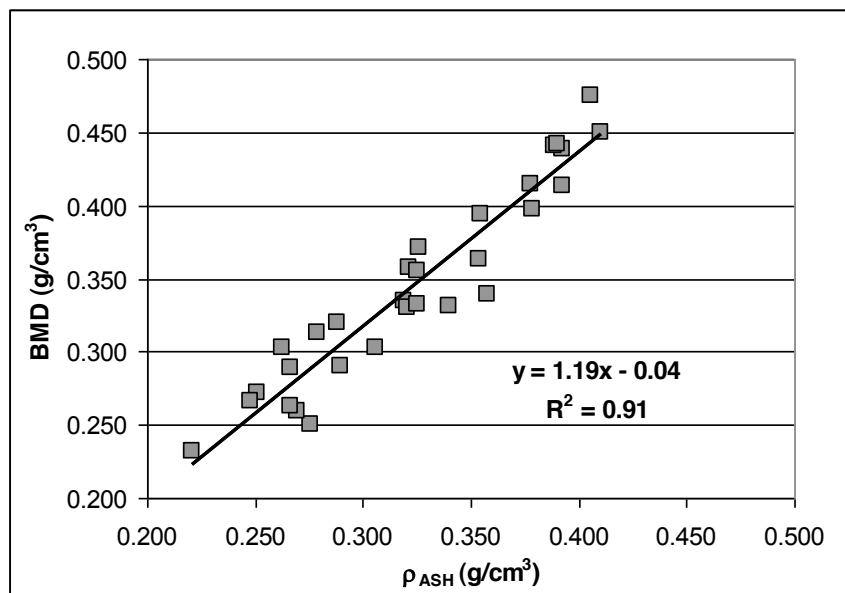


Figure 1: ρ_{ASH} and BMD linear correlation.

Conclusion. A densitometric calibration protocol in microCT applied on trabecular bone specimens was validated. A good correlation was found between the ρ_{ASH} and BMD. However, the slope was found to differ from one [3]. This means that an estimation error is present. This error could be due to the use of a fast acquisition protocol with low resolution, low number of projections and short scanning time. In fact a higher resolution ad scanning time is suggested in literature for the analysis of trabecular bone [3]. Moreover, a beam hardening correction by using step wedge-phantoms was not applied. Better result could be obtained using a more accurate acquisition protocol. Furthermore, ρ_{ASH} calculation using gravimetric procedure could represent further limits of this study. The application of more suitable acquisition parameters and more accurate gravimetric procedure could increase the determination coefficient and decrease the slope.

References.

1. Perilli, E., et al., *A physical phantom for the calibration of three-dimensional X-ray microtomography examination*. J Microsc, 2006. **222**(Pt 2): p. 124-34.
2. Ohman, C., et al., *Mechanical testing of cancellous bone from the femoral head: experimental errors due to off-axis measurements*. J Biomech, 2007. **40**(11): p. 2426-33.
3. Kazakia, G.J., et al., *Assessment of bone tissue mineralization by conventional x-ray microcomputed tomography: comparison with synchrotron radiation microcomputed tomography and ash measurements*. Med Phys, 2008. **35**(7): p. 3170-9.

Micro-CT - its growing use and potential in biomedical applications and some clinical implications

E L Ritman

Mayo Clinic College of Medicine, Rochester MN 55905 USA

Aims. The aim of this presentation is to provide some examples , and possible future possibilities of use of micro-CT imaging to provide mechanistic insights and/or supporting structural information that cannot be obtained with clinical imaging methodologies and/or provide information about the quantitative requirements for some potential clinical imaging approaches.

Method. The presentation will use micro-CT image data generated with custom-made “bench-top” micro-CT scanners as well as synchrotron-based micro-CT scanners. The micro-CT scan data is used to generate voxels of different sizes to explore the ability to detect and quantitate small anatomic structures as well as quantitate CT “density” values in those small structures. The role of purpose-bred and genetically modified small rodents to establish the most informative features that might be used in clinical CT scanners will also be explored.

Results. Specific tissues that were evaluated include bone mineralization in trabecular bone, arterial wall vasa vasorum as reflected by wall opacification following an intravascular injection of contrast agent and calcium/iron deposits , discrimination of the conductive from exchange components of the myocardial microcirculation by virtue of the relationship between the microcirculatory blood volume to the myocardial perfusion.

Conclusion. These data indicate the limits of clinical image voxel sizes and also that the information content of clinical imaged tissues can be extended beyond the resolution of the clinical scanners by including the knowledge provided by micro-CT scans.

Preparing Specimens for X-ray Microtomography

Allan S. Jones

Electron Microscope Unit, Madsen Building F09, The University of Sydney, NSW, 2006

There is no standard reference text that details specimen preparation techniques for the newly emergent technique of X-ray microtomography, and yet with careful attention to this aspect of the microscopy a very wide range of studies can be undertaken not only with hard materials but more interestingly with less dense samples. In this paper I detail approaches to sample preparation that have been successfully used at the University of Sydney.

The instrument that is currently used at the University of Sydney facility is a Skyscan 1172 device (SkyScan, Aartselaar, Belgium). For hard materials the beam energy is set at 100KeV and flux at 100 μ A, whilst for less dense specimens the beam energy is set at 60KeV and flux at 165 μ A.

For mineral samples we have found that core-drilling with diamond coated bits provides an optimal sample. The cores vary in size from 3mm to 19mm in diameter, with a height of 12mm to 15mm. The cylindrical aspect of these cores ensures that the beam path is of equal length at all rotations. In addition, the cylindrical nature of the specimen is ideal in terms of X-ray diffraction minimisation since there are no sharp corners at the external boundary of the specimen [1]. For biological specimens the sample preparation is less straight forward. These specimens are often a mixture of relatively low density tissue and higher density materials that constitute the skeletal structures. Whilst the skeletal structures generally are easily imaged the lower density components are often difficult to get enough contrast in. This situation is compounded by the susceptibility of these samples to dry out and subsequently move during the scan, which makes the data unusable. To mitigate these problems we apply several preparation techniques.

1. The density of soft tissues can be increased by application of heavy metal staining solutions, that include osmium tetroxide, gadolinium chloride, phosphomolibdic acid and phosphotungstic acid [2].
2. The specimens are scanned in thin walled containers that are made from drinking straws of various diameter. This minimises energy loses in the container wall.
3. The samples are scanned in humid conditions (i.e. not immersed) so that drying is minimised whilst avoiding any energy losses due to the presence of fluid.
4. Where specimens are particularly susceptible to dehydration the scan duration is minimised by lowing exposure times, lowing frame averaging and using 180° scan geometry – but the angular increments are kept as high as possible to provide good reconstruction geometry. Typically a scan of 20 minutes is used.

After several years of using these approaches it is clear that the utility of X-ray microtomography can be greatly expanded by careful specimen preparation. A specimen's density can be selectively increased or in some cases decreased by staining, and scans can be optimised by minimising beam energy loses in the containers.

[1] Jones AS; Reztsov A. Loo CE. Micron 38(1):40-48, 2006.

[2] Uzun H, Jones AS, Curthoys IS. Acta Oto-Laryngologica. 127(6): 568 – 573, 2007.

Detecting vasculature inside long bones of rat using Angiofil

Alireza Roshan Ghias, Alexandre Terrier, Dominique Pioletti

Laboratory of Biomechanical Orthopedics, Ecole Polytechnique Federale de Lausanne, Switzerland, alireza.roshanghias@epfl.ch

Aims. Studying microvasculature inside long bones of rat using Angiofil for future bone tissue engineering purposes.

Method. Two different methods of Angiofil injection were used. Three rats were anesthetized by IP injection of Ketamin and Xylasine (1.5+1 ml). For the first rat, the abdominal cavity was opened and the Angiofil was injected to inferior vena cava. For the next rat, the right sephanous vein was used. In the second method, the left ventricle was used for the injection and blood vessels were washed with Saline and fixed with Paraformaldehyde prior to injection of Angiofil. The first two rats died during the injection of Angiofil. The third rat died during the injection of Saline. After the experiment, the legs and kidneys of each animal were harvested and scanned with micro-CT. The images were reconstructed and blood vessels were recognized as far as possible. The harvested specimens were kept in -70°C for 3 weeks after the scanning and re-scanned afterward.

Results. Different methods of injection resulted in different levels of penetration of Angiofil into blood vessels. The inferior vena cava in the first rat was ruptured during injection, so the contrast agent could not be injected properly. Therefore the results of the scanning showed poor Angiofil penetration into blood vessels of the kidney and no Angiofil penetration inside bone vessels. In the case of second rat, the scan results showed fairly good penetration of Angiofil into the kidney. In addition, a big vessel and its daughter vessels inside the both femurs of the rat were clearly visible. However, since the radio-opacity of Angiofil solution was similar to that of cancellous bone, it was not possible to differentiate the micro-vessels from the trabecular bone. In the case of third rat, no Angiofil could be seen neither in kidneys nor in the bones. During the dissection, traces of blood could be seen in the vessels in the first and second rat but not in the third rat. The re-scanning of specimens after being kept in -70°C for 3 weeks showed almost the same results as before.

Conclusion. The results showed the potential of using Angiofil in detecting vasculature inside the long bones. It also showed that the method of injection of Angiofil is very important in the success of the procedure. For example in the case of third rat, since the animal died during injection of saline, no traces of Angiofil could be seen in the vessels which means that the Angiofil was not circulated correctly. In the second rat, although the vasculature was clearly visible in the kidneys, the capillaries could not be detected. This might be because of the injection of low amount of Angiofil and also as a result of remaining blood in the vessels. However, the vasculature inside the femur was fully visible in the diaphysis part of the bone using this technique. It seems that to achieve enhanced results, using higher amounts and higher concentrations of Angiofil is recommended in detecting microvasculature inside long bones. In addition, a suitable protocol for administration of Angiofil for this purpose is highly needed.

New and improved functions in SkyScan micro-CT 3D analysis and visualisation software

Phil Salmon

SkyScan NV, Kontich, Belgium

Ongoing advances in functionality in both the CT-analyser and CT-volume programs ("CTAn" and "CTVol", for dataset analysis and model visualisation respectively) are described, as well as bug fixes. Both CTAn and CTVol are now available in versions compiled for both 64bit and 32bit versions of either Windows Vista or XP. 64bit use with a 64bit operating system is highly recommended for ability to deal with large models.

In CTAn, a new "Bitwise" module has been added to custom processing / BATMAN, applying logical or Boolean comparative operations to the current dataset and ROI, such as AND, NOT, COPY, OR, XOR, SUB. These greatly extend the range of manipulations of both the dataset (binarised or original) and the ROI – which can be considered as a parallel, second dataset. A particularly useful function is <image = image AND ROI> which eliminates all parts of the image outside the ROI, simplifying several tasks under despeckle and morphological operations. (It is a good idea to run this command immediately after reloading original images to an existing ROI mask.) Under bitwise the <ROI = COPY image> replaces the previous "image copy" function under shrink-wrap.

A new individual object 3D analysis is introduced. This calculates the volume, surface and other parameters (e.g. porosity) of each and every individual discreet binarised object (there can be thousands of such objects in a volume of interest); this is important for particle analysis, porosity and other applications. Individual 2D & 3D analysis plugins are now added to custom processing / BATMAN. Porosity analysis is an important part of the analysis software and continues to be extended. The standard 3D morphometric analysis now includes measurement of number, volume and percent volume of pores, defined as always as space voxels fully surrounded in 3d by solid voxels.

The important function of writing an ROI dataset with size reduced to the minimum needed to enclose the ROI, can now be done from custom processing / BATMAN, using a new option under "save bitmaps". This allows the sometimes time-consuming creation of ROI datasets from multiple scans to be run in a batch, reducing operator time. The ROI drawing feature has been enhanced by allowing editing of boundary dots; further, the user can alternate between two ROI editing modes, either editing individual border dots, or shape-shifting the whole shape using a bounding rectangle, in the same way as for fixed shapes. A scale bar can be added to images – also a new option under "save bitmaps".

In the thickness calculation there is an option to restrict the calculation to VOI only. This is selected by default; if unselected, thickness is calculated for whole dataset, eliminating boundary artifact errors in thickness calculation for a selected VOI (but taking more time).

Under raw images, the profile line for reslicing can be edited at both ends. Two sequential resampling cuts gives a quicker and easier possibility for resampling to any 3d orientation. Stereology data associated with the MIL anisotropy analysis (an optional, switchable function) has been validated with the helpful input of Dr Paul Zaslansky from the Max Plank Institute, Germany. Some memory and resource tips are also given for CTAn – CTVol

In the CTVol volume model viewing software, an important addition is the ability to centre multiple models with respect to one of the models that you select. This enables well centered rotation of multiple models. Automatic adjustment of cube size also improves the initial positioning of models in the viewing cube. Saving of properties of visual models (colour, texture, brightness, matt / gloss, transparency etc.) is enabled in a “material” file. There is a modified and improved dialog box for movie making, as well as improved interaction with hardware accelerators. A logarithmic scale of model opacity is optionally available.

The time course of Exia 160 contrast enhancement in healthy mice.

Inneke Willekens^{1,2}, Tony Lahoutte¹, Cindy Peleman¹, Chris Vanhove¹, Rudi Deklerck³, Axel Bossuyt¹ and Johan de Mey²

¹ In vivo Cellular and Molecular Imaging - ICMI - Vrije Universiteit Brussel

² Department of Radiology - UZ Brussel

³ Electronics and Informatics - ETRO - IRIS - Vrije Universiteit Brussel

Background: Micro-CT allows high-resolution volumetric imaging of the inner anatomy of living animals. However, there is too little contrast between the major abdominal organs on the Micro-CT images to allow for a correct delineation. This problem can be solved by using CT contrast agents.

Aim: The purpose of this study was to evaluate the time-course of contrast-enhancement of spleen, liver, and left ventricle using Exia 160 in healthy mice.

Methods: Healthy C57bl/6 mice (n=12) were used in this study. Anesthesia was induced with 5% isoflurane and maintained at 2% for the duration of the scan with mice breathing spontaneously via a mask. Exia 160 (Binitio Biomedical, Inc., Ottawa, CA) was administered intravenously at a dose of 0.05 ml/20g (n=6) or 0.1 ml/20g (n=6). Exia 160 is a blood pool contrast with hepato-selective components, based on an aqueous nonpyrogenic colloidal polydispersed contrast. The animals were scanned in prone position. Imaging was performed using micro-CT (Skyscan 1178 micro-CT system; Skyscan, Aartselaar, Belgium) at a resolution of 83 µm. The total acquisition time was 121 sec. Each animal underwent a Micro-CT scan before contrast injection (baseline) and immediately after contrast injection. Additional scans were performed at 15 min, 30 min, 45 min, 1h, 2h, 3h, 4h, 24h and 48h after contrast. Images were reconstructed the using filtered backprojection (NRecon, Skyscan) and analysed using Amide (Loening et al). Regions of interest (ROIs) were drawn in spleen, liver, and heart. The contrast enhancement was measured for different tissues and expressed in function of time.

Results and Conclusion: Our results show that the Exia 160 contrast enhancement of the spleen reaches a maximum at 15 min while the maximum contrast in the liver occurs at 45 min. The best contrast in the blood was just after contrast injection.

Quality Control in micro-CT

S.Tassani^{1,2}, R.Stoico¹, E. Perilli¹, F. Baruffaldi¹, L.Cristofolini², M.Viceconti¹

¹ Laboratorio di Tecnologia Medica, Istituti Ortopedici Rizzoli, Bologna, Italy,
tassani@tecnio.ior.it

² Engineering Faculty, University of Bologna, Italy

Aims. The micro-CT scanner is becoming a wide spread imaging instrument for morphometric analysis of cancellous bone. Calibration phantoms have been presented, but it does not exist yet an international protocol for quality control. Aim of the present work is to provide a control protocol to verify the scanner status every month.

Method. A human cancellous bone specimen was embedded in PMMA, in order to make it easy to handle and to keep his structure preserved along the years. Five consecutive acquisitions were performed in order to identify the baseline (B.L.) and the standard deviation of the parameters. Afterwards, the same specimen was acquired monthly for a period of 3 years. The same micro-CT examination procedure and configuration was used. Morphometric calculation of two histomorphometric parameters was performed after each acquisition, that is, Bone Volume (BV) and direct Trabecular Thickness (Tb.Th.*).

A control chart was plotted in order to monitor these parameters over time. Every value was defined "Out of Control" if far more than 3 standard deviations from the B.L. Finally, an analysis of variance (ANOVA) among the years and the B.L. was performed.

Results. The values of the selected parameters resulted to be "Out of Control" 14 times for BV and 8 times for Tb.Th* over the 36 analyzed months. Moreover, statistically significant differences among the data collected along each of the three years and the B.L. were found. In particular, during the second and the third year, the Tb.Th* was increased when compared with the first year (first, second and third year $276.3 \pm 1.1 \mu\text{m}$; $277.9 \pm 1.1 \mu\text{m}$; $278.0 \pm 1.7 \mu\text{m}$; $p < 0.01$), and with the B.L. (B.L. $276.2 \pm 0.9 \mu\text{m}$; $p < 0.05$). Similarly during the second and the third year the BV was increased in comparison with the first year (first, second and third year $173.2 \pm 1.0 \text{ mm}^3$; $175.2 \pm 1.0 \text{ mm}^3$; $174.8 \pm 1.8 \text{ mm}^3$; $p < 0.01$), but only the second year resulted to be different from the B.L. (B.L. $173.5 \pm 0.7 \text{ mm}^3$; $p < 0.05$).

The maximum difference between the Tb.Th* and the B.L. ($3.6 \mu\text{m}$) was smaller than the pixel size ($19.5 \mu\text{m}$). On the other hand the maximum difference between the BV trend and the B.L. (3.5 mm^3) was greater than the voxel size ($7.4 \times 10^{-6} \text{ mm}^3$). However, this difference resulted to be the 2% of the B.L.

Conclusion. In conclusion, the quality control performed over three years highlighted some "Out of Control" situations.

Moreover, a significant increase in the examined histomorphometric parameters over time was found. However, the magnitude is very small if compared to the differences that might occur in discriminating bones of different patients. Therefore, these differences, although significant, are negligible. Nonetheless, a control chart is suggested to monitor the behaviour of the micro-CT scanner along the years.

Overview of image reconstruction for micro-CT

Michel Defrise

Department of Nuclear Medicine, Free University of Brussels (VUB), Belgium
mdefrise@ulb.ac.be

We give an overview of the standard algorithm used for 3D CT reconstruction with a flat panel detector and a circular acquisition.

This algorithm published by Feldkamp, Davis and Kress in 1984 is still a work-horse in micro-CT because of its numerical efficiency, ease of implementation, and good robustness. The limitations of this classical algorithm and of the circular acquisition orbit are discussed and illustrated.

The second part of the talk briefly describes recent advances, which allow

- i/ the reconstruction from truncated projections measured when the detector is too small to cover the complete object,
- ii/ the accurate reconstruction of CT data acquired with a spiral orbit, and
- iii/ the correction of various effects such as detector cross talk and after glow using iterative data restoration methods.

Development of micro-CT imaging in a core facility

Kevin Mackenzie

Microscopy and Cellular Imaging Core Facility, Institute of Medical Sciences,
University of Aberdeen, Aberdeen AB25 2ZD
k.s.mackenzie@abdn.ac.uk

Aims. To demonstrate how the use of a Wacom Tablet and Interactive Pen Display can facilitate the drawing of Regions of Interest (ROI's) and also how third party software can be used to view and render reconstructed data from micro-CT. Samples will be shown to illustrate the diverse range of specimens examined over the past 2 years using the SkyScan 1072.

Method. The SkyScan 1072 is normally used to carry out Trabecular and Cortical measurements on bones using the SkyScan CTan software. We discovered that by using a Wacom Intuos3 A5 graphics tablet and pen, the drawing of ROI's was greatly improved compared to using a standard mouse. In order to develop this technique further, last year we purchased a Wacom Cintiq 21UX Interactive Pen Display, an active monitor that allows you to draw directly onto the screen with a stylus.

Results. We have successfully imported reconstruction data sets into other software packages (Velocity and Imaris) commonly used for viewing and analysing z-stacks obtained by confocal microscopy. This allows us to render surfaces, slice through 3D models, and generate movies.

The Core Facility web site (www.abdn.ac.uk/ims/microscopy), on which some of the resulting images are displayed, generates enquires from across the UK and Ireland. Clients want to look not only at bones but also at a surprising range of other samples. For example: fossilised teeth, insects (beetle's, ticks), tendon, aluminium foam, titanium matrix composites, glass fibres, amber, shells and coral.

Conclusions. Where budget allows, the use of a Wacom Cintiq active monitor is highly recommended. If this is not possible, then consider a standard graphics tablet to facilitate drawing ROI's. Secondly: the purchasing of third party software may not compare favourably to what is readily available, free, from SkyScan. However, if you find you already have access to these packages (perhaps within another department) then it is worth experimenting for yourself.

Optimization of µCT image quality of live mice using synchronization

Jeroen Hostens

PHILIP MORRIS Research Laboratories bvba, Grauwmeer 14, 3001 Leuven,
Belgium Jeroen.Hostens@pmintl.com

Aim. Movement during scanning of live mice (mainly due to respiration), greatly reduces µCT image quality. This can be overcome by synchronizing the image acquisition with respiration movement. Several synchronization methods were evaluated using two types of small animal ventilators. During the synchronization setup, numerous parameters need to be optimized to ensure that during image acquisition, movement is kept to an absolute minimum. Depending on the method used, a large increase in image quality can be achieved; however, it is also important to keep the scanning time (and hence radiation dose) to a minimum.

Method. Live mice were scanned using Skyscan 1076. Two major approaches were taken in the effort to synchronize image acquisition with breathing: (1) synchronization with chest movement during autonomous breathing and (2) synchronization with breathing cycle during artificial breathing. For artificial breathing, two animal ventilators were used: the SAR830 and the FlexiVent system from Scireq.

Results. When scanning live mice, both the duration of anesthesia and the radiation dose are limiting factors. Therefore, to optimize the synchronization of image acquisition with respiration, the pixel size was set to 35µm, resulting in scans of approximately 10 to 25 min, depending on the synchronization method.

In a first approach image acquisition was synchronized with chest movement during autonomous breathing. Due to deep anesthesia, resulting in shallow breathing of the mice during scanning, synchronization of image acquisition with chest movement is limited to the exhalation period. As a result, a limited amount of air is present in the lung, which reduces the contrast of the images.

The second approach, in which mice are intubated and mechanically ventilated, has several advantages. A vast number of parameters can be adjusted, e.g., maximum pressure, duration of the inhalation time versus the exhalation time, duration of the total breathing cycle, and frequency. Care must be taken to stay within a physiologically acceptable range. The image acquisition can be set to overlap with the inhalation phase of respiration. The resulting reconstructed images have a much better contrast and resolution. This is especially visible when looking at the tip of the lung, which is most susceptible to movement artifacts.

Conclusion. Synchronization of image acquisition with respiratory movement can significantly enhance image quality. As scanning time increases, the challenge is to keep the radiation dose as low as possible. The very high quality images of lungs of live mice obtained with this method can possibly answer questions that are otherwise impossible to address due to insufficient image quality.

Expectation-maximisation segmentation of trabecular bone from in vivo micro-CT

M. Depypere¹, K. Laperre², G. Carmeliet², F. Maes¹, P. Suetens¹

¹ Medical Image Computing (ESAT/PSI), Faculty of Engineering, K.U.Leuven, Belgium, maarten.depypere@uz.kuleuven.be

² Laboratory for experimental medicine and endocrinology, Faculty of Medicine, K.U.Leuven, Belgium

Aims. A global thresholding operation is usually applied to segment micro computed tomography (micro-CT) images of bone. However, for micro-CT scans of mouse tibiae acquired in vivo, a global threshold will underestimate trabecular bone volume as it fails to correctly segment thin trabecular structures due to the partial volume effect (PVE). We therefore present a local thresholding algorithm to overcome this limitation. The performance of this method is compared to conventional global thresholding using ex vivo scans as golden standard.

Method. Our local thresholding algorithm adopts the pixel classification framework that is typically used for segmentation of brain MR images. This statistical framework computes the probability that a voxel belongs to a certain tissue class, assuming that the intensities are Gaussian distributed within each class. The PVE is modelled by allowing a mixture of two classes in a single voxel. The framework also allows to correct for global intensity inhomogeneity in the image data and to account for contextual spatial information such as voxel intensities of neighbouring voxels. The parameters of the Gaussian mixture model and the classification itself are optimized using the iterative expectation-maximisation approach that is guaranteed to converge to the global optimum.

The tibia of five 14 week old C57/Bl6 mice was scanned in vivo using the SkyScan1076 micro-CT scanner at a pixel size of 9 micron. The mice were then sacrificed and the tibia was isolated. The tibiae were scanned again ex vivo in the SkyScan1172 micro-CT scanner with a pixel size of 5 micron.

Quantitative information on trabecular bone structures is of major interest for our bone analysis. To validate the presented method, trabecular structure parameters such as bone volume fraction (BV/TV), trabecular thickness (Tr.Th), trabecular number (Tr.N) and structure model index (SMI) were evaluated by both the novel method and the conventional global threshold approach. The high resolution ex vivo images served as golden standard. Comparisons were based on the percentage error from the golden standard, which is 100 times the actual difference between the measurement and the golden standard, divided by the golden standard.

Results. Our PVE method improved the estimation of BV/TV, Tr.N and SMI compared to the global threshold. The percentage error from the ex vivo ground truth decreased from -55% to -7% for BV/TV, from -28% to -18% for Tr.N and from 17% to 10% for SMI. The Tr.Th estimate however increased from a difference of 7% to 20% from the ground truth, but much more individual trabeculae were segmented with our method.

Conclusion. We have developed a thresholding technique that gives superior estimates of bone volume fraction, trabecular number and structure model index compared to the conventional global threshold.

Angiofil*: a radiocontrast agent for postmortem microangiography

Silke Grabherr¹, Valentin Djonov², Marco Dominiotto³, Sebastian Friess⁴

¹ Institute of Forensic Medicine, University of Lausanne, 1005 Lausanne, Switzerland

² Institute of Anatomy, University of Fribourg, 1700 Fribourg, Switzerland

³ Institute for Biomedical Engineering, ETH Zurich, 8093 Zurich, Switzerland

⁴ Gloor Instruments AG, 8610 Uster, Switzerland, info@gloorinstruments.ch

* www.angiofil.ch

Aims. The biomedical imaging market is currently seeking a steady growth. One large field comprises the development and marketing of novel radiocontrast agents in order to enhance imaging capabilities of biological tissue that would otherwise not be amenable to computer tomography for its lack of sufficient radiocontrast. We present a novel radiocontrast agent for vascular phenotyping, e.g. as applied in postmortem microangiography.

Method. Angiofil consists of an iodized oil and a diluent. It is purely liquid, gives a high radiocontrast (> 2000 HU, undiluted) and, by further dilution, one can adjust its viscosity. Blood vessels are thus readily perfused, and both stem vessels or small capillaries can be visualized according to sample preparation. We have chosen a set of experiments to prove the high potential of Angiofil for postmortem vascular imaging, among them we report on imaging experiments performed on desktop micro CT systems, as well as several experiments performed on synchrotron radiation sources in Germany and Switzerland.

Results. Angiofil largely circumvents the main problems encountered with particle based compounds, such as incomplete mixing, sedimentation, or extravasation. It remains liquid upon injection, making it a straightforward and easy-to-use compound. We have successfully compared it to barium sulfate stains, and have found that both contrast agents work well for lung vessel imaging in rodents; however, the size of the barium sulfate particles strongly influences infiltration of the vessels, whereas Angiofil does not show such phenomena. In another experiment, we have injected a set of 10 mice for microangiography postmortem. Whole body scans at 40 micrometer pixel size impressively represent the vascular systems, and individually dissected organs are imaged down to a resolution of 15 micrometer. In the latter case, remarkable overviews of the main vessels of each organ can be obtained.

Currently, we evaluate the performance of Angiofil by comparing it to other established iodized compounds, i.e. exIA / fenestra, and we investigate its comparability to casting procedures, such as microfil casting. Additionally, we have started a study on perfusing tumor vessels with Angiofil.

Conclusion. We show in our studies that our radiocontrast agent Angiofil compares well to more established compounds while offering clear benefits. When combined with microcomputed tomography, it has the potential to turn into a powerful method for rapid vascular phenotyping.

Mechanical characterization of porous structures by the combined use of micro-CT and in-situ loading

G. Kerckhofs¹, J. Schrooten¹, L. Elicegui¹, S. Van Bael², M. Moesen¹, S.V. Lomov¹,
M. Wevers¹

¹ Dept. of Metallurgy and Materials Engineering, K.U.Leuven, Kasteelpark Arenberg
44 - bus 2450, B-3001 Leuven, greet.kerckhofs@mtm.kuleuven.be

² Dept. of Mechanical Engineering, Division of Production engineering, Machine
design and Automation, K.U.Leuven, Celestijnenlaan 300b - bus 2420, B-3001
Leuven

Aims. The goal of the study was to investigate the strength of the combined use of microfocus X-ray computed tomography (micro-CT) and in-situ mechanical loading to unravel the relationship between the morphology and mechanical behavior on the one hand, and the failure mechanisms on the other hand of porous structures.

Method. Three different batches of cylindrical porous Ti6Al4V samples with varying pore and constant strut size, produced by rapid prototyping (RP) and more specific by selective laser melting (SLM)^[1, 2], were investigated. First the accuracy of the developed micro-CT loading stage was assessed by validation against a standard mechanical testing device. Then, the inter-batch variation of the morphology and mechanical properties was determined to check the robustness of SLM, followed by a correlation between the morphology and mechanical properties.

Results. For the validation of the micro-CT loading stage, 5 samples per batch were continuously loaded on standard mechanical loading device and 5 on the newly developed micro-CT loading stage. There was no significant difference between the results for the stiffness, strength and strain at maximum load, which indicated that the micro-CT loading stage renders accurate and correct global mechanical properties. Analysis of the morphological properties based on the micro-CT datasets of all samples preloaded at 10N indicated that the standard deviation within one batch was small. The same was seen for their mechanical properties, which confirms the robustness of the production technique. Moreover, it indicates that one random sample within a batch is sufficient for a full batch characterization. Finally, a correlation was found between stiffness and volume fraction determined via micro-CT. The exponential fit shows a factor 2.5. This factor indicates, as was expected, that the pore shape of the assessed structures lies between what Gibson and Ashby^[3] define as being an open cell and a honeycomb.

Conclusion. The newly developed micro-CT loading stage was proven to give accurate and correct results for the global mechanical properties of the tested RP Ti6Al4V porous structures. It was also determined that for further research, one random sample per design can be assessed as a representative. Finally, the correlations functions between the morphology and the mechanical properties can be applied to tailor the design according to the required stiffness and strength.

References

- [1] F. Snijkers et al., Porous Materials as Scaffold for Bone Replacement, Acers-meeting. 2005.
- [2] S. Impens et al., Production and characterization of CaP en Ti scaffolds for bone tissue engineering, 19th European Conference on Biomaterials. 2005.
- [3] L. J. Gibson et al., Cellular solids: structure and properties. 1988: Pergamon Press.

Skyscan 1072 - Sample scanning, reconstruction and visualisation (2D and 3D) protocols

Dr Mark Tarplee¹, Mr Nick Corps²

¹Centre for Micromorphology, Department of Geography, Queen Mary, University of London, Mile End Road, London, UK. E1 4NS M.Tarplee@qmul.ac.uk

²Mr. Nick Corps, e2v scientific instruments, Sirius House, Watery Lane, Wooburn Green, Bucks, UK. HP10 0AP

Aim.

To create a step-by-step guide, from sample scanning through to volumetric 3D visualisation, for both novice and experienced users of the Skyscan 1072 desktop X-ray microtomograph.

Methods.

The first author worked through the existing scanning, reconstruction and analytical/visualisation manuals for the Skyscan 1072 microtomograph, the second author providing invaluable guidance. A sound knowledge of the principles of (micro)tomography was established and the information acquired was systematically recorded, forming a preliminary user guide. An evaluation of the effects of adjustments to individual parameters led to an expansion of the initial protocols and the production of an 'Advanced acquisition' section. A similar approach was taken in the application of the reconstruction (NRecon) and analytical/visualisation (CTAn/CTVol) software. Rigorous, continuous testing of the protocols was conducted throughout the compilation process and additional 'guidelines' section was also produced.

Results.

A robust, detailed but concise set of protocols and guidelines have been developed. The guide has been subdivided into the individual stages of sample scanning, reconstruction and analysis/visualisation, with further subdivisions where appropriate:

- Introduction
- Sample scanning protocol
- Reconstruction protocol
- Reconstructed scan analysis and visualisation protocol
- Guidelines, notes, selected references, F.A.Q's

Conclusions.

A detailed stepwise guide to the effective operation of the Skyscan 1072 microtomograph has been produced. Each stage is methodically, but concisely, described and is designed to complement rather than replace the existing manuals. Supplementary guidelines and additional material have also been provided.